# Quantum Entanglement in Random and Inhomogeneous Spin Chains

**Angel Giovanni Ramírez García**

Institute for Theoretical Physics


Madrid, May 2015

Consejo Superior de Investigaciones Científicas
Universidad Autónoma de Madrid
Instituto de Física Teórica

# Quantum Entanglement in Random and Inhomogeneous Spin Chains

Memoria de Tesis Doctoral realizada por
**Angel Giovanni Ramírez García**
presentada ante el Departamento de Física Teórica de la Materia Condensada de la Universidad Autónoma de Madrid para la obtención del título de Doctor

Supervisado por los Doctores
Javier Rodríguez-Laguna y Germán Sierra Rodero

Madrid, mayo de 2015

*All men live in full view, so that all are obliged both to perform their ordinary task and to employ themselves well in their spare hours; and it is certain that a people thus ordered must live in great abundance of all things, and these being equally distributed among them, no man can want or be obliged to beg.*
Thomas More – Utopia (1516).

*The most painful thing about it (in reference to Quantum Theory): is that throws doubt upon the universality of causality; the view at present is that atoms have a certain amount of free-will, so that their behavior even in theory, is not wholly subject to law.*
Bertrand Russell – The Twilight Of Science (1929).

# Prefacio

Este documento recoge una parte del trabajo realizado durante mi doctorado. Sí, una parte, porque si bien hubo muchas cosas que aprender, no se podría escribir algo tan grande y diverso. La estructura de este documento intenta conjugar dos ideas. Por un lado, la idea de *contar una historia* donde la estructura, los protagonistas y la trama absorban al lector; y por otro lado, la idea de *contar a un estudiante lo que a mi me habría gustado que me contaran al iniciar* la investigación.

El objetivo de esta tesis es estudiar el entrelazamiento cuántico en sistemas aleatorios y sistemas no homogéneos en 1D. Y para ello hemos usado distintos métodos, tanto analíticos como numéricos. También hemos propuesto nuevos métodos que permiten la confirmación de los resultados. Además, hemos usado herramientas computacionales de *software* libre para simulación y análisis numérico que se hemos desarrollado en base a las bibliotecas creadas por J. Rodríguez-Laguna.

Mucho de este trabajo ha sido realizado en el Instituto de Física Teórica de Madrid. También se ha realizado durante estancias en el Instituto de Ciencias Fotónicas de Barcelona y en el Instituto de Física de São Carlos. Además, durante visitas al Instituto de Estructura de la Materia de Madrid, a los Departamentos de Física y de Matemáticas de la Universidad Carlos III de Madrid y especialmente en el Centro de Ciencias de Benasque.

# Agradecimientos

A Germán y Javi, ya que gracias a ellos y a las muchas horas de su tiempo que han dedicado tanto a este trabajo como a la tarea de ayudarme con los aspectos formativos y que, en conjunto han guiado mi investigación. También porque ya fuera en reuniones de trabajo, comidas, charlas de café o de bar aportaron muchos aspectos que me han ayudado a crecer personalmente. No está de más decir que sin su ayuda, esta tesis no habría sido posible.

A Maru, que ha estado conmigo estos *tres de cuatro soles*. Y con estoicismo me ha acompañado durante este tiempo donde muchas veces he tenido que dar prioridad al trabajo. Sin vos no lo habría logrado.

A mi familia quienes, desde la distancia me han brindado su cariño incondicional y apoyo para seguir adelante. También a María Teresa y a Tita quienes han sido como una familia en Madrid. Ya volverá el tiempo de volver a pasearnos por aquella *mansión del pájaro serpiente*.

A mis amigos y amigas. No escribo una lista porque no quisiera ni olvidarme de nadie ni llenar muchas hojas. Ya sea en Guatemala, en Madrid o allá *donde acaben los caminos* siempre podremos empezar una nueva historia o, como en otras ocasiones, continuar con alguna que hayamos empezado antes.

Madrid, mayo de 2015

Angel Giovanni Ramírez García
Instituto de Física Teórica UAM-CSIC

# Quantum Entanglement in Random and Inhomogeneous Spin Chains

by
Angel Giovanni Ramírez García

Submitted to the Department of Theoretical Condensed Matter Physics in partial fulfillment of the requirements for the degree of Doctor

## Abstract

We present the study of quantum entanglement in 1D random systems and inhomogeneous systems. We use a combination of the methods of exact diagonalization and a fermionic version of the Dasgupta-Ma renormalization group. We also introduce a new tool for the study of random hopping models based on the study of random permutations. These methods allow us to describe, in some cases, the states of the systems as a valence bond structure.

We study the low-energy states of the 1D random-hopping model in a strongly disordered regime. Indeed, we analyze the properties of entanglement focusing on the similarities between the conformal field theory predictions for the clean case and the strong disorder renormalization group predictions. The entanglement structure is shown to depend solely on the probability distribution for the length of the effective bonds. Parity oscillations are absent in von Neumann entropy with periodic boundary conditions, but appear in the higher moments of the distribution, such as the variance. The particle-hole excited states leave the bond structure and the entanglement untouched. Nonetheless, particle addition or removal deletes bonds and leads to an effective saturation of entanglement at an effective block size given by the expected value for the longest bond.

We also study the engineer of an exponential deformation for 1D critical local Hamiltonians, based on the renormalization group arguments. We analyze the properties of the entanglement that present a volume growth for the entanglement entropy in the ground state which looks like a rainbow connecting the two halves of the chain. This effect is exemplified in the XX and Heisenberg models. For the XX inhomogeneous model we characterize the crossover between the critical and the maximally entangled ground state in terms of the entanglement entropy and the entanglement spectrum. We also show that, in the weak inhomogeneity limit, the rainbow state is a thermo field state of a conformal field theory with a temperature proportional to the inhomogeneity parameter. We also propose an extension of the model to higher dimensions.

Finally, we study the time-evolution of some valence bond states, e.g. the rainbow and dimer states, after a global quench to a homogeneous Hamiltonian in 1D. After the quench, the entanglement of the half-chain of the rainbow state decreases linearly with time and, after it reaches a minimal value, it increases again to (approximately) its initial value. The dimer state presents the opposite case, the entanglement grows linearly with time to a maximal value, then it decreases to reach its initial value. Furthermore, we propose a ballistic picture, as a generalization of the quasiparticle picture, which seems to explain the linear behaviour of the entanglement. We also use this ballistic picture to study the time-evolution of the dimer state in Rindler space-time.

**Keywords:** quantum entanglement, entanglement entropy, entanglement spectrum, entanglement measurements, many-body physics, random systems, disordered systems, inhomogeneous systems, renormalization group, conformal field theory.

# Quantum Entanglement in Random and Inhomogenous Spin Chains

por
Angel Giovanni Ramírez García

Presentado al Departmento de Física Teórica de la Materia Condensada como requisito previo a optar al título de Doctor

## Resumen

En este trabajo presentamos el estudio del entrelazamiento cuántico en sistemas aleatorios y sistemas no homogéneos en 1D. Para ello hemos usado una combinación de los métodos de diagonalización exacta y una versión fermiónica del método de grupo renormalización de Dasgupta-Ma. También proponemos un método basado en el estudio de permutaciones aleatorias. La aplicación de estos métodos permite, en algunos casos, la descripción de los estados del sistema como una estructura de enlaces de valencia.

Por un lado estudiamos los estados de baja energía de un sistema en 1D con acoplos aleatorios fuertemente desordenados. Analizamos las propiedades del entrelazamiento enfocando en la semejanza entre las predicciones de la teoría de campos conformes asociada al caso homogéneo y las predicciones del grupo de renormalización para el caso fuertemente desordenado. Mostramos cómo depende la estructura de entrelazamiento de la distribución de la probabilidad de la longitud de los enlaces efectivos. Además mostramos la existencia de oscilaciones de paridad que, aunque no se presentan en el caso de un sistema con condiciones de contorno periódicas, sí aparecen en momentos de orden superior, como la varianza. En cuanto a los estados excitados, mostramos que el estado partícula-hueco no altera la estructura de enlaces, por lo que no afecta el entrelazamiento. Sin embargo, los estados excitados obtenidos al agregar o quitar partículas sí afectan la estructura de enlaces, lo que causa una saturación del entrelazamiento para un tamaño efectivo de bloque dado por el valor esperado de la longitud del enlace más largo.

Por otro lado, basándonos en argumentos de grupo de renormalización, hemos diseñado una deformación exponencial de los enlaces para un sistema crítico descrito por un Hamiltoniano local en 1D que presenta un entrelazamiento máximo. Mostramos que éste presenta un crecimiento volumétrico en la entropía de entrelazamiento del estado fundamental, que tiene la forma de un arcoíris (*rainbow*) conectando las dos mitades de la cadena. Estudiamos este efecto en los modelos XX y de Heisenberg. Para el modelo XX, estudiando la entropía y el espectro de entrelazamiento, encontramos una caracterización de la transición entre el estado fundamental para un sistema crítico y el estado fundamental para el sistema máximamente entrelazado. También mostramos como el estado *rainbow* puede interpretarse como el estado *thermo field* de una teoría de campo conforme con una temperatura que es proporcional al parámetro que determina la no homogeneidad. También, proponemos una extensión para un modelo en 2D.

Finalmente, estudiamos la evolución temporal de algunos estados que presentan una estructura de enlaces de valencia, por ejemplo el estado *rainbow* y el estado dimerizado, después de un *quench* a un Hamiltoniano homogéneo en 1D. La evolución temporal del entrelazamiento, para el caso del estado *rainbow* decrece con el tiempo hasta un valor mínimo y luego aumenta hasta casi alcanzar su valor inicial. Por el contrario, en el estado dimerizado, el entrelazamiento aumenta hasta un valor máximo y luego disminuye hasta su valor inicial. También proponemos una descripción ballística, que generaliza la

descripción basada en cuasi-partículas, y que parece explicar el comportamiento lineal del entrelazamiento. Además, usamos la descripción balística para estudiar la evolución temporal del entrelazamiento del estado dimerizado en un espacio-tiempo de Rindler.

**Keywords:** quantum entanglement, entanglement entropy, entanglement spectrum, entanglement measurements, many-body physics, random systems, disordered systems, inhomogeneous systems, renormalization group, conformal field theory.

# Contents

**1 Introduction** **1**
1.1 Entanglement in history . . . . . 1
1.2 Entanglement and its measures . . . . . 3
1.3 Entanglement in many-body systems . . . . . 4
1.4 Entanglement and the area law . . . . . 8
1.5 Motivations and outline . . . . . 10

**2 Quantum Many-Body Models** **13**
2.1 Introduction . . . . . 13
2.2 Free Fermion models . . . . . 14
2.3 Spin models . . . . . 16
2.4 Jordan-Wigner transformation . . . . . 17
2.5 Entanglement in Free Fermion systems . . . . . 18
2.6 Corrections to the scaling of Entanglement . . . . . 19
2.7 Entanglement in Inhomogeneous systems . . . . . 21

**3 Random Systems: The Random Hopping Model** **27**
3.1 Introduction . . . . . 27
3.2 Entanglement in the Ground State . . . . . 30
3.3 Bond-length distribution . . . . . 37
3.4 Random permutations . . . . . 42
3.5 Entanglement in Low-energy Excited States . . . . . 45

**4 Engineering the Inhomogeneity: the Rainbow State** **51**
4.1 Introduction . . . . . 51
4.2 The rainbow state model . . . . . 53
4.3 Entanglement over the Rainbow . . . . . 61
4.4 Generalizing the Rainbow State . . . . . 75
4.5 Qubistic picture of the Rainbow State . . . . . 79

**5 Quenched Dynamics of Valence Bond States** **81**
5.1 Introduction . . . . . 81
5.2 Quenching a Free Fermion State . . . . . 82
5.3 Quenching from Dimer to Clean . . . . . 84
5.4 Quenching from Rainbow to Clean . . . . . 85
5.5 The Ballistic Bond Picture . . . . . 90
5.6 Quenching a Dimer State on a Rindler Space-time . . . . . 100

**6 Conclusions and Future work** **103**

**Bibliography** **117**

**A Technical details** **119**
A.1 Conformal representation . . . . . 119
A.2 Strong Disorder Renormalization Group . . . . . 120
A.3 Brief summary of the quasi-particules picture . . . . . 121

**Acronyms** **123**

# Chapter 1

# Introduction

## 1.1 Entanglement in history

In the first decades of the twentieth century quantum mechanics was already established empirically and its mathematical foundations were under study. Nonetheless, its philosophical implications were still unclear. The Copenhagen Interpretation was the first general attempt to understand the microscopic world using the formalism of quantum mechanics theory. But one of the most important debates in physics (and philosophy) was about to begin: the completeness of the theory. A fundamental contribution to this debate was given by Einstein *et al.* (1935) using a *Gedankenexperiment*,[1] which subsequently became known as the Einstein-Podolsky-Rosen (EPR) paradox, which argues that we cannot maintain both an intuitive criterion of local action and the completeness of the quantum description by means of the wave function. See figure 1.1 for a description of the EPR paradox.

Schrödinger (1935a) called *Verschränkung*[2] this inability to describe the quantum states of two systems after a temporary physical interaction in the same way as before the interaction. In his discussions about separated systems he stated: *"I would not call that one, but rather the characteristic trait of quantum mechanics, the one that enforces its entire departure from classical lines of thought"* (Schrödinger, 1935b, 1936). Following the debate, Bohr (1935) replied to Einstein insisting on about the unambiguous meaning of his criterion of physical reality when it is applied to quantum phenomena.

The debate also derived into the philosophical realm, where it stayed for many years. New contributions in physical terms included a proposal of a non-local hidden-variable theory by Bohm (1952a,b) and the description of a simplified version of the EPR *Gedankenexperiment* with spin-1/2 particles proposed by Bohm and Aharonov (1957). Finally, it was Bell (1964, 1966) in a discussion about the mathematical implications of hidden-variable theories who showed that local hidden variables cannot reproduce

[1] German word for thought experiment
[2] German word for entanglement

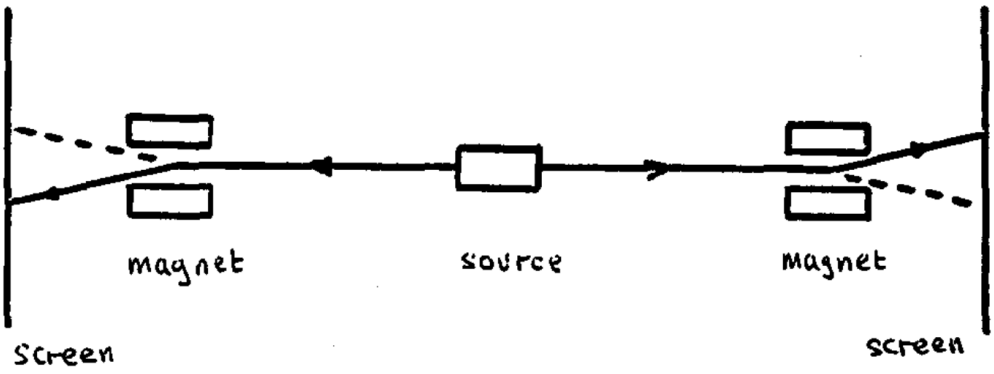


Figure 1.1: Bohm-Aharonov's setup for the Einstein-Podolsky-Rosen *Gedankenexperiment*. Two particles of spin-1/2 in a singlet state, i.e. total spin zero, are separated in opposite directions from their common source. The separation method does not influence the total spin and the particles move far enough to avoid their interaction. Each particle is sent into Stern-Gerlach magnets which separate the spin-up and spin-down components along any axis the observer decides to measure. With this setup, the spin components of the particles will anti-correlate in any axis. (Original figure from Bell, 1981).

the measurement correlations that quantum mechanics predicts. In other words, Bell showed that the predictions of quantum mechanics contradict local-realistic views of the EPR paradox and require some sort of action at a distance even though they strictly respect the postulates of special relativity. Bell's inequalities became a bound to the correlations predicted by local-realistic theories. See figure 1.2 for an example of Bell's measurements.

The establishment of that limit opened a door for experimental tests. Clauser *et al.* (1969) proposed an optical version of the Bell's setup to measure pairs of photons emitted in an atomic radioactive cascade. Freedman and Clauser (1972) realized the experiment with atoms of calcium and they found a violation of the Bell's inequalities. But the experimental setup still needed to solve several loopholes, e.g. the detection efficiency, the fair sampling, the freedom of choice. Aspect *et al.* (1981) improved the setup and were able to measure the linear-polarization correlation of photons. The experiment confirmed the predictions of quantum mechanics and the violation of Bell's inequalities. The result was also confirmed using more complex techniques and more refined experiments with the same conclusions (Aspect *et al.*, 1982b,a; Tittel *et al.*, 1998; Rowe *et al.*, 2001; Ursin *et al.*, 2007).

Thus, as Schrödinger predicted, entanglement in composite systems has become the characteristic feature of quantum mechanics and is a key element in the foundations of the theory. Therefore, its characterization is of great interest in many areas of physics where our ability to control single quantum systems, e.g. scanning tunnelling microscopy, cold atoms or ion traps, allows us to reach unexplored regimes in physics. Nowadays, entanglement is the fundamental resource in many of the applications of quantum information and quantum computation. These two areas attract a large interest since

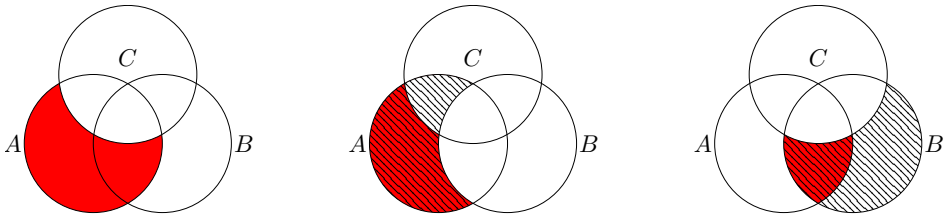


Figure 1.2: Description of Bell's inequalities: The picture shows that the event $P(A \cap \bar{C})$ in red in the left diagram is composed of the two mutually exclusive events, which also appear (in red) as components in the other two events $P(A \cap \bar{B})$ in the centre and $P(B \cap \bar{C})$ in the right. So, classically, Bell's inequality $P(A \cap \bar{C}) \leq P(A \cap \bar{B}) + P(B \cap \bar{C})$. In quantum mechanics, dichotomous measure of events can not be simultaneously done.

the demonstration by Shor (1994) of the ability of quantum computers to speed-up the process of finding prime factors of an integer. Experimental developments has allowed to reach milestones such quantum teleportation of entangled states by Ma *et al.* (2012) over 143 km between the two Canary Islands: La Palma and Tenerife.

## 1.2 Entanglement and its measures

Entanglement is defined as the property of those pure states which do not allow a description as product of states, i.e. *non-factorizable* states. For a composite system divided in two parts $A$ and $B$ with Hilbert space $\mathcal{H} = \mathcal{H}_A \otimes \mathcal{H}_B$, a factorizable state can be written as

$$|\psi\rangle = |\psi_A\rangle \otimes |\psi_B\rangle,$$

where states $|\psi_A\rangle$ and $|\psi_B\rangle$ describe $A$ and $B$ respectively. Factorizability of states can be determined using the Schmidt decomposition (Schmidt, 1907), all states in $\mathcal{H}$ can be expressed as

$$|\psi\rangle = \sum_{i=1}^{\chi} d_i |a_i\rangle \otimes |b_i\rangle,$$

where $|a_i\rangle$ and $|b_i\rangle$ are orthonormal states of $\mathcal{H}_A$ and $\mathcal{H}_B$ respectively. The Schmidt coefficients satisfy $d_i > 0, d_i \in \mathbb{R}$ and normalize $|\psi\rangle$. The Schmidt number (or Schmidt rank) $\chi$ is bounded by the dimension of Hilbert spaces of $A$ and $B$, i.e. $\chi \leq \min\{\dim\mathcal{H}_A, \dim\mathcal{H}_B\}$. Based on the Schmidt decomposition, a state is factorizable if $\chi = 1$, in case $\chi > 1$ the state is not factorizable, i.e. it is entangled.

Factorizability defines absence of entanglement. But in order to quantify entanglement it is convenient to use the density matrix description of the state. Von Neumann (1932) introduced the density matrix formalism in order to study mixed states that were needed to develop both quantum statistical mechanics and a theory of quantum

measurements.

There are different measures of entanglement such as von Neumann entropy, Rényi entropies, etc. but we will focus our description of entanglement in terms of the former. The density matrix operator of a pure state $|\psi\rangle$ is defined as $\rho = |\psi\rangle\langle\psi|$. From the point of view of an observer restricted to part $A$, the state is mixed and can be described by the reduced density matrix $\rho_A = \mathrm{Tr}_B \rho$. We can define von Neumann's entropy of this reduced density matrix

$$S_A = -\mathrm{Tr}\rho_A \log \rho_A.$$

Let us remark that for a pure state, $S_A = S_B$. Von Neumann's entropy satisfies $S_A \geq 0$. Moreover, $S_A = 0$ only for factorizable states, i.e. when there is no entanglement. Von Neumann's entropy is also called the entanglement entropy or the entropy of entanglement.

Why is $S_A$ called an entropy? There is a deep relation with the concept of entropy in statistical mechanics and information theory. Indeed, von Neumann's entropy is a quantum analogue of Gibbs entropy. But in contrast, it is not related to thermal fluctuations. The entanglement entropy can be argued to measure quantum correlations between subsystems. In classical information theory, the action of sending a message is also viewed as the action of correlating the sender and the receiver. The average amount of information contained in that message is measured with Shannon's entropy (Shannon, 1948). Von Neumann's entropy is just Shannon's entropy of the eigenvalues of the reduced density matrix, which can be regarded as a probability distribution. Quantum information theory builds upon this deep relation between entanglement and information.

## 1.3 Entanglement in many-body systems

How does entanglement behave in real quantum systems composed by many parts? Those systems are required for the study of many relevant condensed matter applications, such as superconductivity, magnetism, quantum Hall effect, superfluidity, etc. as well as new synthetic setups such as cold atoms in optical lattices, trapped ions, superconducting qubit systems, etc.

Low dimensional systems are of special relevance since they present stronger correlation effects and a higher deviation from the predictions of mean field theory. Spin chains are 1D systems consisting of an array of $N$ sites, labeled as $n = 1, 2, \ldots, N$. Each site can be identified with a spin-$s$ particle in one of its $d = 2s + 1$ different states, with a local Hilbert space $\mathcal{H}_1 = \mathbb{C}^d$.

One of the first successes of quantum many-body physics was the understanding of the magnetic properties of materials, which could not be explained within classical me-

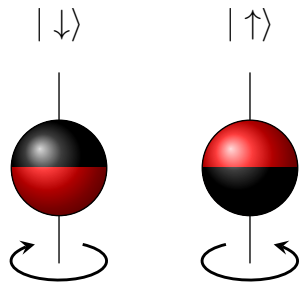


AFM: $|\uparrow\downarrow\rangle$ or $|\downarrow\uparrow\rangle$

FM: $|\uparrow\uparrow\rangle$ or $|\downarrow\downarrow\rangle$

Singlet: $\frac{|\uparrow\downarrow\rangle - |\downarrow\uparrow\rangle}{\sqrt{2}}$

Triplet: $\frac{|\uparrow\downarrow\rangle + |\downarrow\uparrow\rangle}{\sqrt{2}}$, $|\uparrow\uparrow\rangle$ and $|\downarrow\downarrow\rangle$

Figure 1.3: Representation of the spin-1/2 system. Left: spin-down and spin-up for one particle. Right: for two particles where states can be ferromagnetic (FM) or antiferromagnetic (AFM); or with total spin 0 (singlet) or total spin 1 (triplet).

chanics (van Vleck, 1932). Heisenberg (1928) studied this problem, taking into account the exchange interaction between electrons.

He proposed a simple model with a Hamiltonian based on a nearest neighbours interaction in a spin chain:

$$H = J \sum_i \vec{S}_i \cdot \vec{S}_{i+1}.$$

Let us focus on the case of spin-1/2 (see in figure 1.3 the representation of states of spin-1/2 particles). The spin operators $\vec{S}$ are then defined in terms of the Pauli matrices $S^q = (1/2)\sigma^q$. For $J < 0$ the ground state (GS) is ferromagnetic (FM) and $(N+1)$-fold degenerate. All the spins of the particles align without the need for any external magnetic field. This FM state can be chosen to be a product state $|\uparrow\rangle \otimes \cdots \otimes |\uparrow\rangle$ or $|\downarrow\rangle \otimes \cdots \otimes |\downarrow\rangle$. In this case it does not present entanglement and its entanglement entropy is zero. For $J > 0$ the GS is an anti-ferromagnetic (AFM) state, which is non-degenerate and presents entanglement. In fact the AFM state is much more complex than the FM one as we will see below.

The importance of the Heisenberg model goes beyond its description of quantum magnetism. Other phenomena can be also described by the same mathematical formalism. Different concepts and techniques have been developed from the study of this model. The exact solution of the spin-1/2 antiferromagnetic model was obtained with the Ansatz proposed by Bethe (1931). Furthermore, numerical studies benefited from the development of the numerical renormalization group (NRG) introduced by Wilson (1975) who applied it to solve the Kondo model: a spin impurity in a Fermi sea (see figure 1.4).

The applicability of Wilson's NRG to other systems was not straightforward. White (1992, 1993) found that an estimate of the wave function could be used to select the most representative local states for each block (see figure 1.4). That selection can be made optimal with the reduced density matrix. At each renormalization group (RG) step those block states can be used to build a new variational Ansatz for the global

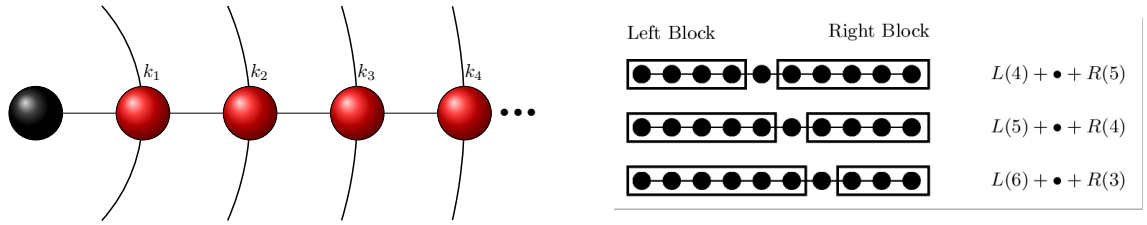


Figure 1.4: Left: Representation of the NRG's blocks applied to the Kondo model where the leftmost site (black) represents a magnetic impurity and others represent momentum shells in the Fermi sea. At each RG step the magnetic impurity swallows the contiguous momentum shell and renormalizes. Right: Representation of the DMRG's blocks where each node represents a physical site encapsulated in blocks. At each step the full wave-function of the system is estimated variationally from the states defining the blocks and the central site. This wave function is then used to renormalize the growing block, in this case, the left block. (Original DMRG figure from Rodríguez-Laguna, 2002).

GS, thus closing the cycle. This constitutes the density matrix renormalization group (DMRG) method.

The DMRG has shown its worth giving insight in the understanding of other problems such as the confirmation of the conjecture proposed by Haldane (1983) about the existence of a gap in the spectra for integer spin Heisenberg chains. Haldane based the conjecture on a map to an non-linear sigma model $O(3)$ which was known to have a gap because of topological reasons.

The performance of DMRG depends on the number of states per block required to achieve a certain accuracy. This number was found to be bound for 1D gapped systems. This feature made DMRG a very powerful numerical instrument. But, to understand the physical reason behind the success of DMRG we need to take a step back in time.

Affleck, Kennedy, Lieb and Tasaki (AKLT) presented a model similar to the Heisenberg Hamiltonian in 1D for spin-1 (Affleck *et al.*, 1987, 1988) whose GS was rather simple. This state was based on the introduction of an auxiliary space of two spin-1/2 per site where a valence bond state is established between nearest neighbors (see figure 1.5). Fannes *et al.* (1992) extended the idea of valence bons states and generalized to translation invariant states, which they called finitely correlated states (FCS). Klümper *et al.* (1993); Lange *et al.* (1994) applied the AKLT idea to the GS of those models with an explicit FCS form. They called matrix product state (MPS) to the common representation for those GSs

$$|\psi\rangle = \sum_{s_1 s_2 \ldots s_N}^{d_1} \mathrm{Tr}\left[A_1^{s_1} A_2^{s_2} \cdots A_N^{n_N}\right] |s_1, s_2, \ldots, s_N\rangle,$$

where matrices $A_i^{s_i}$ correspond with the auxiliary space used for the site-representation. The dimension of the matrices is related to the Schmidt number, and is called the bond dimension. See in figure 1.6 the graphical representation of an MPS.

Östlund and Rommer (1995) showed that the fixed point limit of the DMRG leads

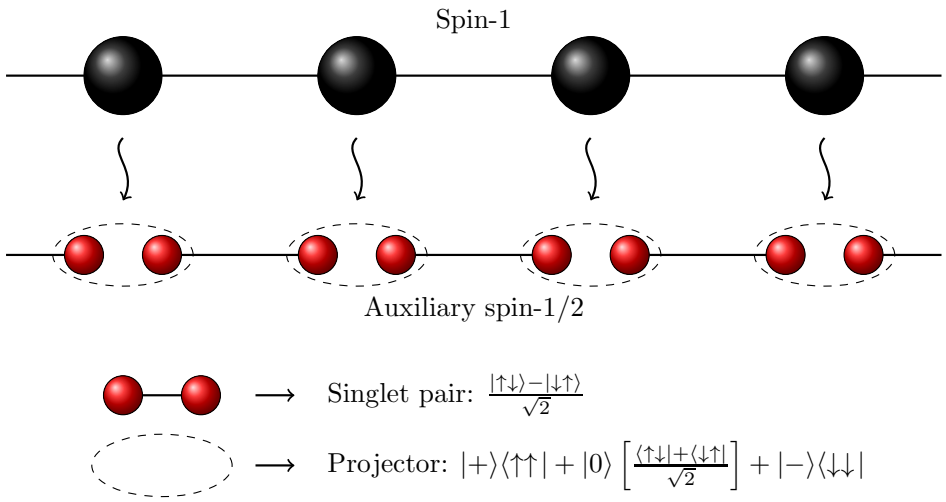


Figure 1.5: Representation of the ground state of the Affleck, Kennedy, Lieb and Tasaki model for a spin-1 chain. Each spin-1 particle (in black) is expressed with two auxiliary spin-1/2 particles (in red) where a valence bond solid in a singlet pair is established between nearest neighbors. The representation of the original particle then relies on the projection on the total spin-1 subspace.

to an Ansatz which can be explored variationally and is fundamentally independent of the renormalization scheme. They proposed a set of MPS as a variational family for the study of infinite homogeneous systems but the results were not precise enough as those obtained with the DMRG method. Dukelsky *et al.* (1998) presented more evidence of the equivalence of DMRG and MPS comparing the spectrum of the reduced density matrix obtained with both methods. These results confirmed the relation between the number of states required for a good representation by the DMRG method and the dimension of the matrices required by the MPS method. This relation was confirmed when Daley *et al.* (2004) introduced the time evolution block decimation (TEBD) in terms of MPS without an explicit relation to the DMRG method.

The large list of successes of the DMRG method for 1D systems unveiled the idea that the MPS could provide an efficient and accurate description of the low energy states of spin chains. The idea of MPS is extensible to higher dimensional systems where the auxiliary space per site is represented with a tensor. Thus, the system can be seen as a tensor networks (TN) and the representation of its state is known as projected entangled pair states (PEPS) (Verstraete and Cirac, 2004) for 2D systems or, in general, tensor product state (TPS) for any dimension. A TPS can be represented as

$$|\psi\rangle = \sum_{\alpha_{12},\alpha_{13},\alpha_{14}} A^{s_1}_{\alpha_{12},\alpha_{13},\alpha_{14}} A^{s_2}_{\alpha_{12}} A^{s_3}_{\alpha_{13}} A^{s_4}_{\alpha_{14}} |s_1, s_2, s_3, s_4\rangle,$$

where $A^{s_i}$ is a tensor and its rank depends on the number of links connecting site $i$ (cf. figure 1.6).

The field of TN constitutes a collection of techniques which captures relevant entan-

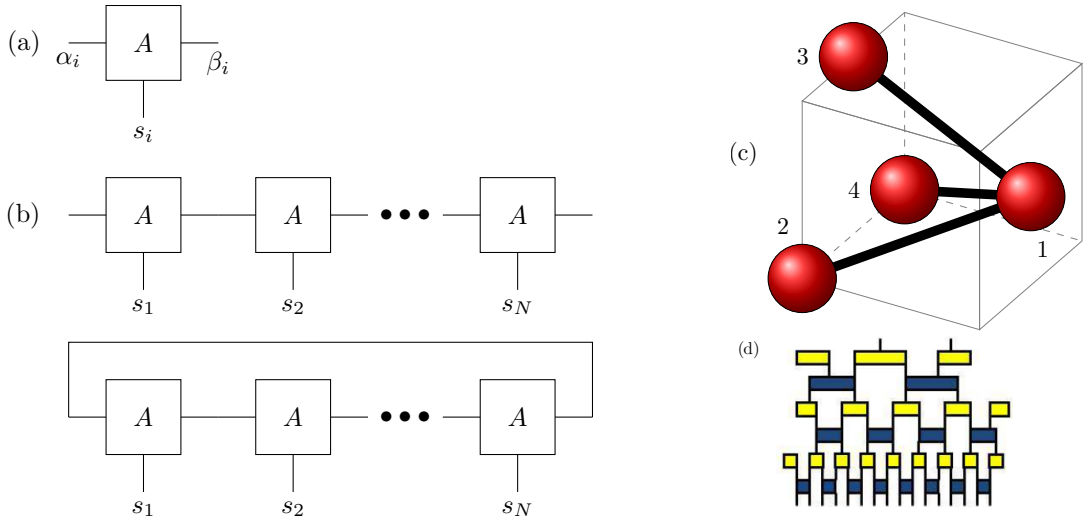


Figure 1.6: Graph representation of tensor networks. (a) Matrices $A^{s_i}_{\alpha_i,\beta_i}$ represented in terms of a rank-3 tensor where the index $s_i$ represents the spin particle in the $i$-th site and indices $\alpha_i$ and $\beta_i$ are related to the auxiliary space used in the representation of the $s_i$ particle. (b) The matrix product state for a 1D system with open an periodic boundary conditions. (c) 2D system of 4 sites. Each site is represented with an auxiliary space and links between sites are established in terms of that space. (d) Typical multiscale entanglement renormalization Ansatz and its pattern of isometries which represents a sequence of unitaries and isometries. (Original MERA figure from Cirac and Verstraete, 2009).

glement properties of 1D systems in terms of the MPS or, in case of 2D systems, using the PEPS or the multiscale entanglement renormalization Ansatz (MERA) (Vidal, 2007, 2008) which is a variational extension of the MPS which includes new layers of tensors representing different levels of block renormalization.

## 1.4 Entanglement and the area law

Entropy found an unexpected application in black hole physics. The black-hole entropy is the measure of the inaccessibility of information for an external observer, i.e. any particular internal configuration, and not to a thermal entropy inside the black hole. Bekenstein (1973) based on analogies between thermodynamics and black hole physics proposed

$$S \propto \mathcal{A},$$

where $\mathcal{A}$ the horizon area. Hawking (1975) fixed the proportionality constant proposed by Bekenstein.

The Bekenstein-Hawking law of black-hole entropy inspired Bombelli *et al.* (1986) and later (and independently) Srednicki (1993) to compute the entropy of the reduced density matrix of a real scalar field satisfying the Klein-Gordon equation when properly

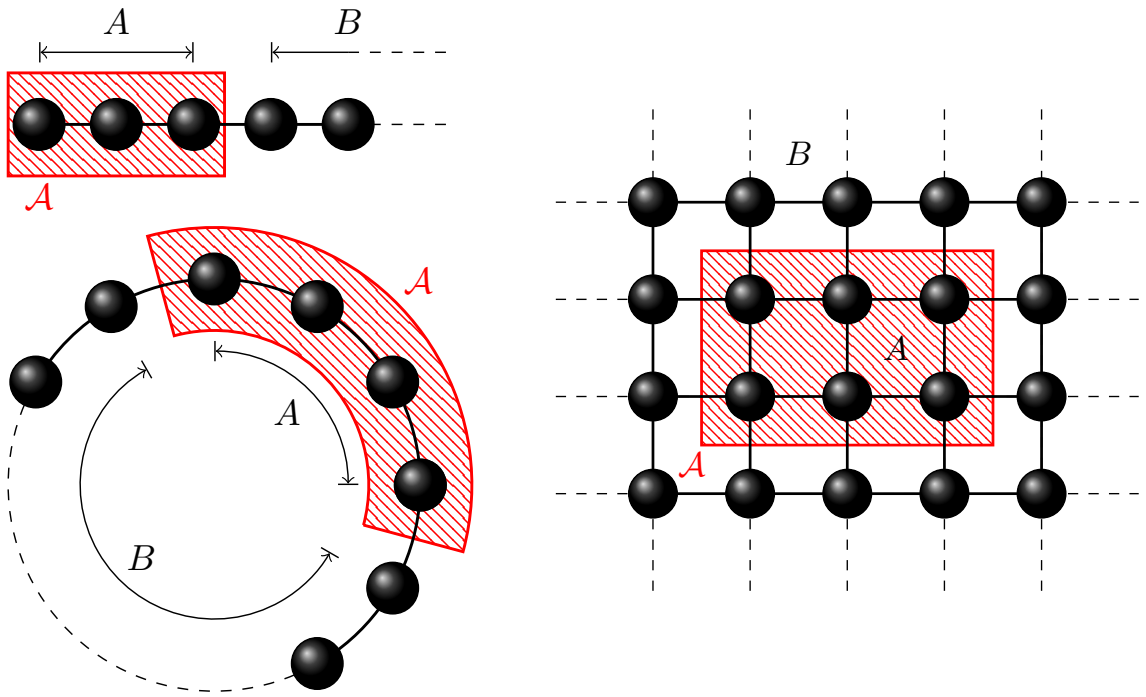


Figure 1.7: Representation of a bipartite system $A : B$ separated by an area $\mathcal{A}$. If the system is gapped and fulfills the area law the entanglement entropy will be proportional to the area $\mathcal{A}$. Left: 1D systems with open and periodic boundary conditions where $\mathcal{A}$ may consist in one or two points connecting $A$ and $B$. Right: 2D system where $\mathcal{A}$ is the perimeter around $A$.

regularized also follow an area law. This computation proved that the area law is more general and not only tied to black hole physics.

The first sufficiently general theorem was given by Hastings (2007) who proved that GSs of 1D systems with a finite gap in the spectrum would saturate their entanglement entropy. The saturation length depends on the correlation length. See figure 1.7.

What happens if the system is gapless? In general we do not have a rule. A special case is composed of those gapless systems which are described with a conformal symmetry. Conformal field theory (CFT) in 1+1 dimension is characterized by an infinite dimensional symmetry group (Di Francesco *et al.*, 1997). Holzhey *et al.* (1994) showed that the entanglement entropy of a block of size $\ell$ in a free boson field in 1D is given by

$$S \sim \frac{c}{3} \log \ell,$$

where $c$ is the central charge of the associated CFT. This expression was confirmed by Vidal *et al.* (2003) for several models and a more general study of entanglement entropy in CFT was made by Calabrese and Cardy (2004).

Entanglement has become a very useful tool to study the structure of complex quantum states, such as the GS of interacting systems (Amico *et al.*, 2008), since geometry and quantum structure are linked via the area law (Eisert *et al.*, 2010). Moreover, entanglement is a key resource which is *as real as energy* (Horodecki *et al.*,

2009) and has potential for many applications of quantum information, but also in some unexpected areas such as its relation to the holographic principle (Ryu and Takayanagi, 2006).

## 1.5 Motivations and outline

Quantifying entanglement is still an open problem, especially for multipartite systems. The entanglement can be quantified in bipartite systems, as we discussed above, using the entanglement entropy which is in many cases bounded by an area law. Nonetheless, some critical 1D systems violate this area law and present logarithmic corrections which are parametrized by the central charge of the associated CFT. Furthermore, other violations to the area law may appear in random systems and inhomogeneous systems.

There is a large interest on inhomogeneous systems since, in reality, even a crystalline solid contains lattice defects, e.g. point defects, impurities, dislocations or grain boundaries. Thus, crystals show more or less random deviations from the ideal lattice structure. The question of how this disorder influences the properties of a crystal, arises naturally.

In chapter 2 we describe some spin chains and 1D fermionic models which can be applied in the study of random systems and inhomogeneous systems. We explore the ground state and low-energy excited states, which allow in some cases a valence bond structure description. We present the method used to study the entanglement properties of the systems and the scaling behavior of the entanglement. We also discuss an RG method specifically designed for the study of the inhomogeneous fermionic systems.

In chapter 3 we discuss the fermionic systems with random hopping. Those systems have been studied from different perspectives and they have been found as a rich source of problems and surprises. The case of 1D systems with strong off-diagonal disorder is known to present logarithmic violations of the area law, although they are known to be non-conformal. The logarithmic corrections are parametrized with an *effective* central charge related to the CFT associated to the clean system

$$S \sim \frac{c_{eff}}{3} \log \ell.$$

We analyze the properties of entanglement in random hopping models, focusing on the similarities between the CFT predictions for the clean case and the strong disorder RG predictions. We use a combination of methods: exact diagonalization, a transformation of the Dasgupta-Ma strong disorder renormalization group (SDRG) and a new tool based on the study of random permutations. All techniques coincide in providing a compelling image, based on a bond-picture.

In chapter 4 we discuss the engineering of an inhomogeneous 1D fermionic system, in

order to obtain a maximal growth of the block entropy in the ground state that we have called *the rainbow state* in which sites symmetrically placed with respect to the center are maximally entangled. We analyze a deformation of critical local 1D Hamiltonians, which interpolates between a logarithmic law for the growth of the entanglement entropy and a volume law

$$S \sim N.$$

The couplings between neighboring sites decay exponentially, as we move away from the middle point. The deformation parameter allows us to interpolate between the uniform model, described by CFT, and the strong disorder limit when the GS becomes a rainbow state.

Moreover, we study the GS of the deformed system in the vicinity of the homogeneous model, based on the applicability of field-theoretic methods. We also study the entanglement spectrum and its relation with the entanglement spacing. From this relation arises the interpretation the ground state of the system as a thermo field state which links the entanglement structure to the emerging geometry of space-time.

In chapter 5 we study the time evolution of different valence bond states (VBSs) after a global quench to a homogeneous Hamiltonian in 1D. We discuss the evolution of a fermion state expressed as a Slater determinant after a quench to a free fermion Hamiltonian. We present the evolution of the entanglement in quenches to clean Hamiltonians, first starting from a rainbow state and then, starting from a dimer state.

The analysis of the correlation between pairs of sites suggests the motion of certain objects or quasi-particles, but with apparent *superluminal* velocity. Of course, no locality principle is violated, because the quench is global. Indeed, we propose a generalization of the quasi-particle picture, which we have called the *ballistic picture*. Furthermore, we use this ballistic picture to show how to predict the entanglement evolution of dimerized states and other bond structures. We also study the time evolution of these bond states under a Hamiltonian with a position-dependent speed of light, i.e. a Rindler Hamiltonian.

# Chapter 2

# Quantum Many-Body Models

## 2.1 Introduction

Quantum many-body systems are models which allow us to illustrate important notions about macroscopic physics, e.g. magnetic behaviour, in terms of microscopic elementary interactions between the constituents of that system. In addition to their physical interest, the development of new methods for their study has given an impulse to other fields such as quantum integrability (Baxter, 1981), quantum groups (for a review see the book by Gómez *et al.*, 1996), quantum computation and information (Nielsen and Chuang, 2010) or quantum simulators (Lewenstein *et al.*, 2007).

Early studies of many-body quantum mechanics used to make the assumption that each particle moves under the effective field created by all the others, i.e. Hartree-Fock or mean-field type methods (Ashcroft and Mermin, 1976). These techniques are very successful to explain many properties of the electrons in solids, through the use of the Fermi liquid approximation or Density Functional Theory (Hohenberg and Kohn, 1964; Kohn and Sham, 1965). Nonetheless, they are unable to take completely into account the effect of strong correlations, which are a key in most magnetic properties of materials, superconductivity (Bardeen *et al.*, 1957a,b), quantum Hall effect (Laughlin, 1981) or topological insulators (Fu and Kane, 2007).

Furthermore, the advent of new technologies such as cold atoms in optical lattices or trapped ions (Bloch *et al.*, 2008; Lewenstein *et al.*, 2012), allows to engineer quantum systems in which strong correlations are not avoided, but looked for. The reasons can be to mimic other quantum systems (e.g. superconductors) or to harness the specific effects of quantum correlations to profit from them, building better computation and communication technologies.

## 2.2 Free Fermion models

Consider a system of $N$ sites, whose dynamics is described by the Hamiltonian

$$H = -\sum_{i,j=1}^{N} t_{ij}\, c_i^\dagger c_j + \text{h.c.} \tag{2.1}$$

where $t_{ij}$ is the $(N \times N)$ hopping matrix, $c_i^\dagger$ and $c_i$ are, respectively, the fermionic creation and annihilation operators on site $i$, and they satisfy anticommutation relations

$$\{c_j, c_k^\dagger\} = \delta_{jk},$$
$$\{c_j, c_k\} = \{c_j^\dagger, c_k^\dagger\} = 0.$$

The elements of the hopping matrix are chosen to satisfy $t_{ij}^* = t_{ji}$ in order for the Hamiltonian (2.1) to be hermitian.

The Hamiltonian (2.1) which is quadratic in fermionic operators, is also called free fermion Hamiltonian. Moreover, free fermion Hamiltonians are solvable in terms of single-body states that are occupied by particles which move independently of each other. Diagonalizing the hopping matrix $tv_k = \epsilon_k v_k$ allows to obtain the single-body energy levels $\epsilon_k$ and the single-body modes $v_{k,i}$ which determine a canonical transformation

$$b_k^\dagger = \sum_i v_{k,i} c_i^\dagger, \tag{2.2}$$

$v_{k,i}$ is an unitary matrix, thus the new operators $b_k^\dagger$ also follow fermionic commutation relations, i.e. $b_k$ are also fermionic operators.

All eigenstates of the Hamiltonian (2.1) have the form

$$|\psi\rangle = \prod_{k \in \Omega} b_k^\dagger |0\rangle, \tag{2.3}$$

where $|0\rangle$ is the Fock vacuum, which is annihilated by the operators $b_k$. The energy for the state (2.3) is $E = \sum_\Omega \epsilon_k$. The set $\Omega$ contains the single particle energy levels that are occupied. Therefore, the ground state (GS) is given by filling up all modes with negative energy, i.e. $\Omega = \{k \mid \epsilon_k < 0\}$. It is also customary to fix the number of particles, in that case the energy of the highest occupied mode is called the Fermi energy $\epsilon_F$.

The correlation matrix $C$ has elements defined by

$$C_{ij} \equiv \langle GS | c_i^\dagger c_j | GS \rangle \tag{2.4}$$

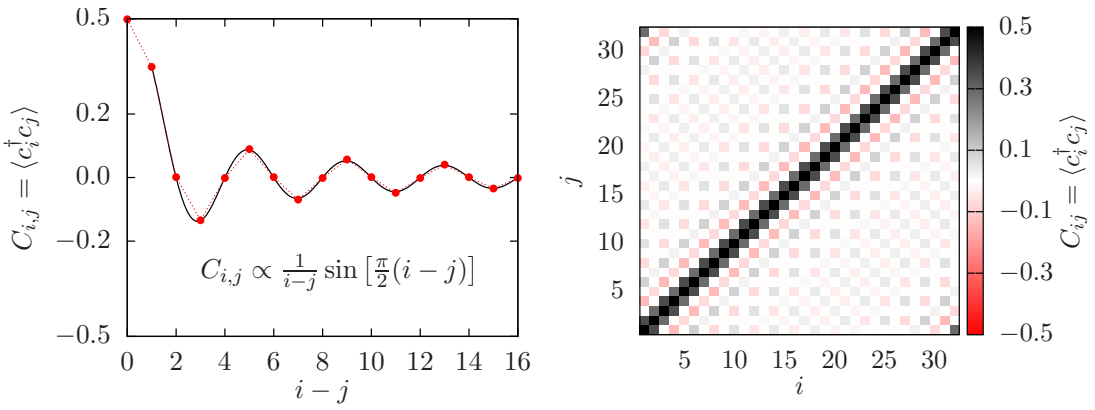


Figure 2.1: Structure of the correlation matrix defined by equation (2.4) for a system of $N = 32$ sites with periodic boundary conditions. Left: correlation of the $i$-th site with all other sites in the system. Right: projection to see the correlation of each site $i$ with each site $j$.

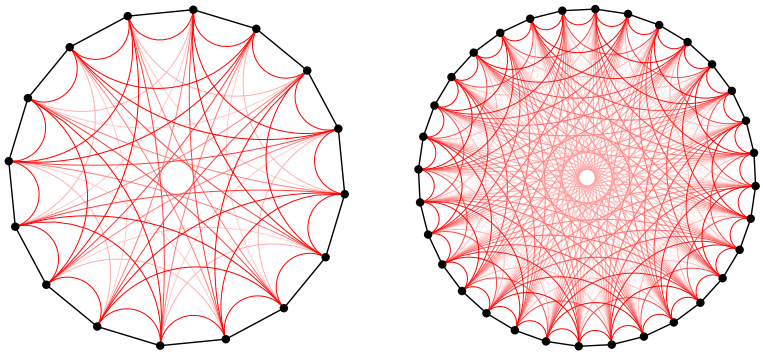

Figure 2.2: Structure of the correlation matrix defined by equation (2.4) with periodic boundary conditions for systems of size $N = 8$ (left), $N = 16$ (centre), $N = 32$ (right).

which, in terms of the single-body modes is

$$C_{ij} = \sum_{k=1}^{n_F} \bar{v}_{k,i} v_{k,j}, \tag{2.5}$$

where $n_F$ is the number of fermions in the system. Figure 2.2 shows the structure of the correlation matrix for a 1D system with periodic boundary conditions (PBC) for different system sizes. The intensity of each line connecting two sites is related to $|C_{ij}|$ as discussed in appendix A.1.

In this thesis, we focus on the study of GSs and low-energy excited states. Following the description introduced by Ibáñez Berganza *et al.* (2012), the low energy excited states can be called *compact* if all the occupied modes are contiguous in energy space, otherwise they are *non-compact*.

For compact excited states, we denote by $|x\rangle$ the state obtained by removing $x$ particles ($x < 0$), or adding $x$ particles ($x > 0$) to the GS.

We will consider the non-compact excited state called particle-hole (PH) which is obtained by moving one particle below the Fermi point to another symmetric mode

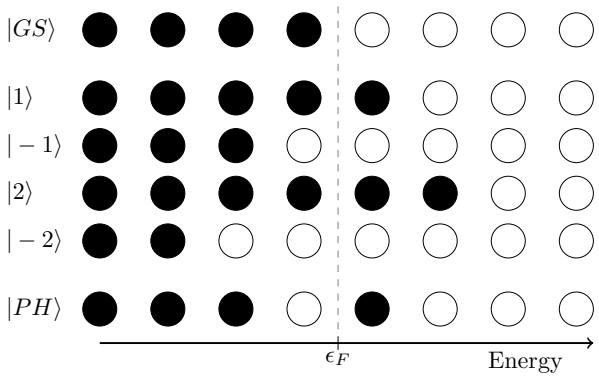


Figure 2.3: Summary of some low energy excitations for a system of size $N = 8$ at half filling. The ground state (GS) in the first line is for reference of the Fermi level. Below the GS appear some examples of compact excited states and finally, the last line is the particle-hole (P-H) excited state, which is a non-compact excited state.

above the Fermi point. See figure 2.3 for a summary of those states.

## 2.3 Spin models

The Heisenberg model is a fundamental key for quantum magnetism as well as for other phenomena that can be effectively described by quantum spin operators $\vec{S}$. Additionally, its mathematical structure allows the understanding of a wide range of concepts and techniques, i.e. it is a prototype model to study integrability or conformal field theory (CFT).

Consider a 1D system of $N$ spin-1/2 particles with PBC, its dynamics is described by the Hamiltonian

$$H = J \sum_{i}^{N} \vec{S}_i \cdot \vec{S}_{i+1}, \tag{2.6}$$

where $J$ is an exchange interaction parameter, that is positive for antiferromagnetic chains and negative for ferromagnetic ones. $\vec{S}_i$ are spin operators: they form a representation of the algebra of SU(2), a set of operators whose commutation rules are

$$\left[S_i^a, S_i^b\right] = i\epsilon^{abc} S_i^c. \tag{2.7}$$

Furthermore, spins at different sites commute. The boundary conditions require $S_{N+1} = S_1$. The Hamiltonian (2.6) was solved exactly by Bethe (1931), which was the origin of the Bethe Ansatz.

Precisely, in Heisenberg chains there is a famous conjecture posed by Haldane (1983) suggesting that there is a *gap*, i.e. a finite difference in energies between the ground and the first excited state, for integer spin Heisenberg chains, and no gap for half integer

chains. There is no proof, only a plausibility argument brought by topological reasoning.

A generalization of the Heisenberg model is to consider different exchange couplings for each direction: $J_x$, $J_y$ and $J_z$. Indeed, some interesting cases appear for special sets of couplings, when $J_x = J_y$ the Hamiltonian (2.6) becomes

$$H = \sum_{i=1}^{N} J_x(S_i^x S_{i+1}^x + S_i^y S_{i+1}^y) + J_z S_i^z S_{i+1}^z, \tag{2.8}$$

and is called the XXZ model, which is integrable. Furthermore, it is customary to introduce an anisotropy parameter $J_z = \Delta$ and fixing $J_x = 1$. The system is gapless in the range $-1 < \Delta \leq 1$ (Yang and Yang, 1966a,b,c).

For $\Delta = 0$ it is called the XX model, its dynamics is defined by the Hamiltonian

$$H = J_x \sum_{i=1}^{N} S_i^x S_{i+1}^x + S_i^y S_{i+1}^y = \frac{J_x}{2} \sum_{i=1} \left( S_i^+ S_{i+1}^- + S_i^- \sigma_{i+1}^+ \right), \tag{2.9}$$

where $S_j^{\pm} = S_j^x \pm i S_j^y$ are the raising and lowering operators which flip the spin in the site $j$. This model depends only on one parameter, however we can let it vary depending on site $J_x = J_i$. In this case we obtain the inhomogeneous XX model and its dynamics is defined by

$$H = \sum_{i=1} \frac{J_i}{2} \left( S_i^+ S_{i+1}^- + S_i^- S_{i+1}^+ \right), \tag{2.10}$$

the XX model is critical. It is also exactly solvable by the Jordan-Wigner transformation that we discuss below, even in the inhomogeneous case.

## 2.4 Jordan-Wigner transformation

Jordan and Wigner (1928) introduced a transformation which allows to map a 1D system in spin representation onto an equivalent system in terms of fermionic operators. It provides a better way to understand physical properties of spin systems by mapping them into a mathematically equivalent but physically different system.

Using the Jordan-Wigner (JW) transformation, we can map the Hamiltonian (2.10) into a free fermions Hamiltonian. Therefore we only need to solve the single-body problem which involves diagonalizing a $(N \times N)$ matrix instead of the $(2^N \times 2^N)$ matrix related to the many-body problem. This feature allows us to study fairly large systems.

The spin operators $S^+$ and $S^-$ can be represented exactly in terms of the fermionic

operators $c$, so for the $j$-th site

$$S_j^- = \left(\prod_{\ell=1}^{j-1} e^{i\pi n_\ell}\right) c_j = (-1)^{N_{j-1}} c_j,$$
$$S_j^+ = c_j^\dagger \left(\prod_{\ell=1}^{j-1} e^{i\pi n_\ell}\right) = c_j^\dagger (-1)^{N_{j-1}},$$

where $n_i = c_i^\dagger c_i$ is the occupation in the $i$-th site and $N_j = \sum_i^j n_i$, i.e. the transformation include a phase factor which depends on the number of fermions at the left of $i$.

Now, the transformation of the product of spin operators is

$$S_i^+ S_{i+1}^- = c_i^\dagger (-1)^{N_{i-1}} \ (-1)^{N_i} c_{i+1} = c_i^\dagger c_{i+1},$$
$$S_i^- S_{i+1}^+ = (-1)^{N_{i-1}} c_i \ c_{i+1}^\dagger (-1)^{N_i} = c_{i+1}^\dagger c_i,$$

then, the inhomogeneous Hamiltonian (2.10) has a fermionic representation like Hamiltonian (2.1). There arises a relation between the hopping matrix with the exchange coupling

$$t_{ij} = -\frac{J_i}{2}\delta_{|i-j|,1}. \tag{2.11}$$

The phase factor introduced by the transformation represents a problem in case of PBC since in general $S_N^+ S_1^- \neq c_N^\dagger c_1$. Instead, we have

$$S_N^+ S_1^- = (-1)^{n_F} c_N^\dagger c_1, \tag{2.12}$$

where $n_F = \sum_i^N n_i$ is the number of fermions in the system. In the sector of even $n_F$ both models have the same boundary conditions. If $n_F$ is odd, PBC map to anti periodic boundary conditions (APBC).

## 2.5 Entanglement in Free Fermion systems

Consider the GS of a 1D system of free fermions, with $N$ sites with dynamics described by the Hamiltonian (2.1). Let us study the entanglement of for a given block $B$ of $\ell$ sites in the system. As described above, the physics of the low-energy eigenstates can be analyzed finding the correlation matrix restricted to the block $B$, which is given by

$$C(\ell) = \begin{pmatrix} C_{1,1} & C_{1,2} & \cdots & C_{1,\ell} \\ C_{2,1} & C_{2,2} & \cdots & C_{2,\ell} \\ \vdots & \vdots & \ddots & \vdots \\ C_{\ell,1} & C_{\ell,2} & \cdots & C_{\ell,\ell} \end{pmatrix}, \tag{2.13}$$

where each element $C_{i,j}$ is obtained with equation (2.5). A second way to find the correlation matrix (2.13) is based on the measurement on the reduced density matrix $\rho_B$

$$C_{ij} \equiv \langle GS|c_i^\dagger c_j|GS\rangle = \mathrm{Tr}\rho_B c_i^\dagger c_j. \tag{2.14}$$

According to Wick's theorem (Peschel, 2003) this fixes $\rho_B$ completely. Indeed, the reduced density matrix $\rho_B$ can be written as a tensor product of density matrices of single-mode blocks

$$\rho^B = \bigotimes_k^\ell \rho_k,$$

where $\rho_k = \nu_k d_k^\dagger d_k + (1-\nu_k) d_k d_k^\dagger$ or

$$\rho_k = \begin{pmatrix} \nu_k & 0 \\ 0 & 1-\nu_k \end{pmatrix}, \tag{2.15}$$

for some $d$ and $d^\dagger$ which are other fermionic operators which we want to find.

Combining equations (2.14) and (2.15) we can assert that the eigenvalues of the correlation matrix for the block must coincide with the $\nu_k$ and can be used to determine the eigenvalues of the reduced density matrix, i.e. the entanglement spectrum.

The family of $\alpha$-th order Rényi block entropies can be obtained as a sum of the entropies of each $\rho_k$

$$S_\alpha(B) = \frac{1}{1-\alpha} \sum_k \log\left[\nu_k^\alpha + (1-\nu_k)^\alpha\right], \tag{2.16}$$

and the von Neumann entropy for the block corresponds to the limit $\alpha \to 1^+$

$$S_1(B) = -\sum_k \left[\nu_k \log(\nu_k) + (1-\nu_k)\log(1-\nu_k)\right]. \tag{2.17}$$

## 2.6 Corrections to the scaling of Entanglement

Consider an infinite critical system in 1D, described by a certain CFT with a central charge $c$. The $\alpha$-order Rényi entanglement entropy for a block $B$ of $\ell$ contiguous sites with the rest of the system is given by (Holzhey *et al.*, 1994; Vidal *et al.*, 2003; Calabrese and Cardy, 2004, 2009)

$$S_\alpha(\ell) \simeq \frac{c}{6}\left(1 + \frac{1}{\alpha}\right)\log\ell + c'_\alpha, \tag{2.18}$$

where $c'_\alpha$ is a non-universal constant.

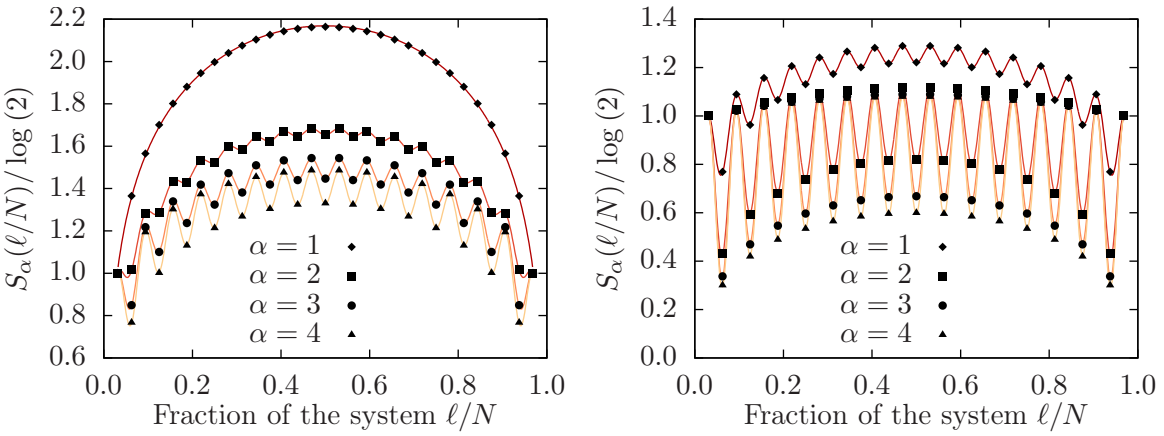


Figure 2.4: Entanglement entropy $S_\alpha(\ell)$ for the homogeneous XX model of $N = 32$ sites for different block size $\ell$. Left: for periodic boundary conditions. Right: for open boundary conditions. Solid lines are fits to equations (2.23) and (2.25).

Let us study the corrections related to the finite size of the system. For a finite system of size $N$ with PBC, the corrections to the von Neumann entropy of the block $B$ follows the law (Holzhey *et al.*, 1994; Calabrese and Cardy, 2004, 2009)

$$S_1^{CFT}(\ell) \approx \frac{c}{3} \log\left[\frac{N}{\pi} \sin\left(\pi \frac{\ell}{N}\right)\right] + c_1', \tag{2.19}$$

and the $\alpha$-order Rényi entropy follow the law

$$S_\alpha^{CFT}(\ell) \approx \frac{c}{6}\left(1 + \frac{1}{\alpha}\right) \log\left[\frac{N}{\pi} \sin\left(\pi \frac{\ell}{N}\right)\right] + c_\alpha', \tag{2.20}$$

In the limit $\ell \ll N$, equations (2.19) and (2.20) recover the law given by equation (2.18). For open boundary conditions (OBC), the universal corrections depend on the position of $B$. If one of the borders of $B$ coincide with the border of the system then, the number of bonds connecting the block with the rest of the system is one half of the number of bonds for the PBC case. Thus, the von Neumann entropy follows the law

$$S_1^{CFT}(\ell) \approx \frac{c}{6} \log\left[\frac{2N}{\pi} \sin\left(\pi \frac{\ell}{N}\right)\right] + \tilde{c}_1', \tag{2.21}$$

and the $\alpha$-order Rényi entropy follow the law

$$S_\alpha^{CFT}(\ell) \approx \frac{c}{12}\left(1 + \frac{1}{\alpha}\right) \log\left[\frac{2N}{\pi} \sin\left(\pi \frac{\ell}{N}\right)\right] + \tilde{c}_\alpha', \tag{2.22}$$

where $\tilde{c}_\alpha'$ is a non-universal constant. The scaling behaviour for each case represent logarithmic violations of the area-law, which was discussed in section 1.4. Furthermore, the finite size scaling of the entropy in finite chains is useful to find the central charge $c$ of the theory.

The logarithmic corrections given by equations (2.19) and (2.20) only describe the

leading behaviour of the entanglement entropy. Moreover, for $\alpha > 1$ the Rényi entropies present parity oscillations (Xavier and Alcaraz, 2011; Calabrese and Cardy, 2009) whose amplitude increases with the order $\alpha$. In case of $\alpha = 1$, i.e. the von Neumann entropy, the parity oscillations only appear for OBC.

Calabrese and Essler (2010) introduced a new term to describe the parity oscillations for systems with PBC which follow a Luttinger liquid theory

$$S_\alpha(\ell) \approx S_\alpha^{CFT}(\ell) + f_\alpha \cos(2k_F\ell) \left[\frac{2N}{\pi} \sin\left(\pi\frac{\ell}{N}\right) \sin\left(k_F\right)\right]^{\frac{-2K}{\alpha}}, \tag{2.23}$$

where $K$ is the Luttinger parameter, $k_F$ is the Fermi moment and $f_\alpha$ is a non-universal parameter which, to reproduce the behaviour of the von Neumann entropy of a system with PBC is defined as $f_1 \equiv 0$. For the homogeneous XX model $K = 1$ and $k_F = \pi/2$ at half-filling and $f_\alpha$ is a function defined by

$$f_\alpha = \frac{2}{1-\alpha} \left[\frac{\Gamma\left(\frac{1}{2} + \frac{1}{2\alpha}\right)}{\Gamma\left(\frac{1}{2} + \frac{1}{2\alpha}\right)}\right]^2. \tag{2.24}$$

Fagotti and Calabrese (2011) derived the term to describe the parity oscillations in systems with OBC

$$S_\alpha(\ell) \approx S_\alpha^{CFT}(\ell) + f_\alpha \cos(2k_F\ell) \left[\frac{4N}{\pi} \sin\left(\pi\frac{\ell}{N}\right) \sin\left(k_F\right)\right]^{\frac{-K}{\alpha}}, \tag{2.25}$$

where $f_1 \equiv -1$ and for $\alpha > 1$

$$f_\alpha = \frac{2}{1-\alpha} \left[\frac{\Gamma\left(\frac{1}{2} + \frac{1}{2\alpha}\right)}{\Gamma\left(\frac{1}{2} + \frac{1}{2\alpha}\right)}\right]. \tag{2.26}$$

Figure 2.4 shows the von Neumann and the $\alpha$-order Rényi entropies for the homogeneous XX model with $N = 32$ sites with PBC (left panel) and OBC (right panel) for different block-sizes. Solid lines are fits to equations (2.23) and (2.25).

## 2.7 Entanglement in Inhomogeneous systems

Let us consider a 1D inhomogeneous system with $N$ spin-1/2 particles, and choose exchange couplings $J_i > 0$ in the strongly inhomogeneous regime, i.e. $J_i$ may span very different values. The dynamics of the system is described by the Hamiltonian (recall Hamiltonian (2.10))

$$H = \sum_{i=1} \frac{J_i}{2} \left(S_i^+ S_{i+1}^- + S_i^- S_{i+1}^+\right). \tag{2.27}$$

Within this regime, we can rely on the strong disorder renormalization group (SDRG) scheme devised by Dasgupta and Ma (1980) in order to obtain the GS. This renormalization scheme is a decimation procedure in which one chooses the strongest coupling, $\max\{J_i\}$, to establish a singlet bond between the two neighboring sites, i.e. $J_k$ localizes a singlet state $(|\uparrow\downarrow\rangle - |\downarrow\uparrow\rangle)/\sqrt{2}$ between sites $k$ and $k+1$. Then, using second order perturbation theory, one finds the effective coupling between the two neighbours of the singlet

$$J_k^{(R)} = \frac{J_{k-1}J_{k+1}}{J_k}. \tag{2.28}$$

After this step, we obtain a Hamiltonian for the $N-2$ active sites with an effective term for the two decimated sites. The renormalization continues by choosing the next largest coupling between the active sites. Therefore, some effective couplings may emerge at long distances since, after some iterations, previously renormalized sites dilute in the original system.

Finally, the iterative procedure leaves us a structure of singlet bonds connecting sites over arbitrarily long length scales in the $N$-sites system, allowing us to picture the GS as a singlet *bond structure*. Moreover, it allows to understand that the entanglement entropy of a block $B$ can be obtained by counting the number of singlet bonds connecting the block with the rest of the system (Refael and Moore, 2009). Remarkably, the Dasgupta-Ma renormalization group (RG) has recently received an interpretation within the the tensor networks (TN) and holography language (Goldsborough and Römer, 2014). In the framework of TN, each renormalization step can be seen as a disentangler operation between the sites contained in the bond (Cirac and Verstraete, 2009).

We translate the original SDRG scheme into a fermionic description (Ramírez *et al.*, 2014b, 2015) using the JW transformation. The inhomogeneous hopping model is a 1D system of $N$ sites, its dynamics is described with the fermionic version of Hamiltonian (2.27):

$$H = \sum_{i=1} \frac{t_i}{4} c_i^\dagger c_{i+1} + \text{h.c.} \tag{2.29}$$

mapping the exchange couplings $J_i$ as inhomogeneous hopping amplitudes $t_{ij} = t_{i,i+1} = t_i$ according to equation (2.11).

The JW transformation is a non-local transformation which requires a modification of the SDRG scheme to take into account the fermionic nature of the particles. Effective hoppings between non-contiguous sites are equal to the corresponding coupling in the XX model multiplied by a phase, $t = (-1)^{n_F} J/2$, which depends on the number of fermions $n_F$ between the two sites. In order to obtain further insight into the reason for this transformation, consider a 1D chain of $N = 4$ sites depicted in figure 2.5. Two singlet bonds are established between sites 1 and 4 and between sites 2 and

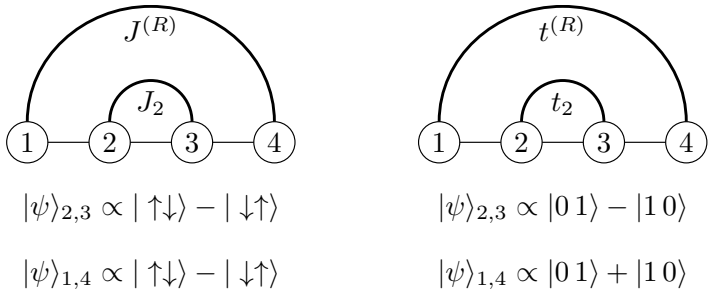


Figure 2.5: Modification to the renormalization rule of the SDRG. Left: for spin systems following equation (2.28). Right: for fermionic systems following equation (2.30).

3. When transformed, via the JW transformation, into a fermionic state, it becomes $\left(c_1^\dagger + c_4^\dagger\right)\left(c_2^\dagger - c_3^\dagger\right)|0\rangle$.

This rule can be implemented with a simple modification of the RG prescription. Since a single fermion is always added at each RG step,

$$t_k^{(R)} = -\frac{t_{k-1}t_{k+1}}{t_k}. \tag{2.30}$$

This implies that the hoppings can be either positive or negative. When they are positive, a singlet-type *bond* is established between both sites, of the form $|\Psi^-\rangle \propto |01\rangle - |10\rangle$. If the hopping is negative, the corresponding triplet-type *anti-bond* is established: $|\Psi^+\rangle \propto |01\rangle + |10\rangle$. Both types of bonds share many properties, such as the entanglement. They both represent different flavors of a Bell pair.

The decimation scheme follows the same procedure: one chooses the strongest coupling, $\max\{|t_i|\}$ and establishes a single-particle state as a bond on top of it (see figure 2.6 (a)). Then, the two neighboring sites are joined by a renormalized (effective) link. The strongest link and its two neighbours are replaced by this (weaker) renormalized link (cf. figure 2.6 (b)-(c)). We can then proceed to pick the second strongest link and iterate the process until all the links have been renormalized (assuming a system with even number of sites). At some moment, the strongest link will be one of the renormalized links in previous iterations. Thus, a long-distance bond will be established between two sites which were not nearest neighbours.

How do we explain the long-distance bonds from the fermionic perspective? The physical picture is illustrated in figure 2.6. Let us consider the particle at the rightmost site. It has a certain probability of hopping to its left, whenever the inner bond particle is also at its left site. At this moment, the inner bond becomes doubly occupied. The original particle inside the inner bond is not allowed to hop rightwards, but it may hop leftwards. As particles are indistinguishable, the total procedure can be described as a tunneling of one particle through an established bond. The associated probability amplitude of this event is much lower than the probability amplitude of hopping in the inner bond, thus accounting for the large differences in energy between them. This procedure, which is akin to the Anderson mechanism describing the interaction between

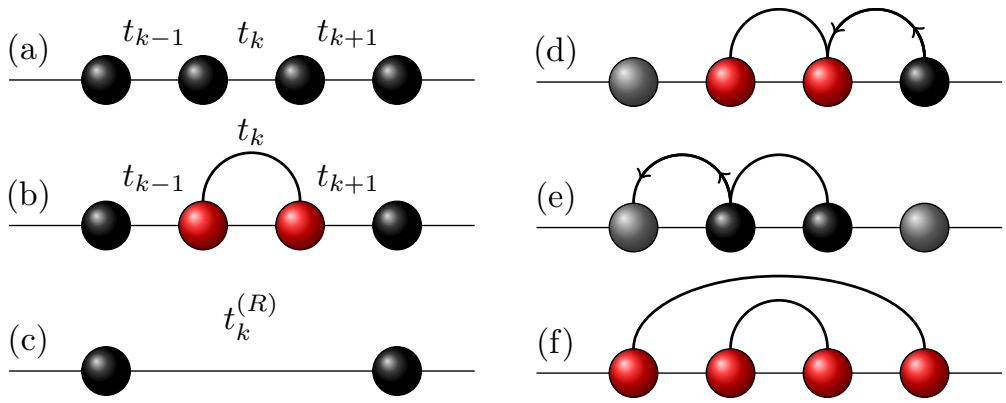


Figure 2.6: The RG procedure: (a) initial system of size $N$. (b) The strongest link $t_k$ establishes a single-particle state. (c) The links $t_{k-1}, t_k, t_{k+1}$ are replaced by an effective link $t_k^{(R)}$ given by equation (2.30), the system now has an effective size $N-2$. Illustration of the physical picture which induces long-distance bonds: (d) A bond has been established on the central link, which is very strong. A particle at the right extreme attempts to jump in. (e) Sometimes, the particle succeeds, and the central bond becomes doubly occupied. The left particle must jump out. (f) We can view the full procedure as a tunneling event through the occupied bond, with a much lower associated probability amplitude.

a magnetic impurity and the spin of a conduction electron, can be assigned an effective hopping amplitude using second-order perturbation theory, thus obtaining expression (2.30). Similarly, one can think of the second-order procedure which allows to find an effective Heisenberg Hamiltonian with $J \approx t^2/U$ from a Hubbard system in the limit $U \gg t$.

When the decimation procedure is finished, we obtain a bond-structure, such as one of those illustrated in figure 2.7, with many bonds of length one, but still with a certain fraction covering larger distances. Notice that the bond structure factorizes into pairs, i.e. there is a pairing of the sites: $\{(i_1, j_1), (i_2, j_2), \cdots, (i_{L/2}, j_{L/2})\}$, such that the GS for the system factorizes into the product of a singlet state for every pair. In other words, each pair $(i_k, j_k)$ is disentangled from the rest of the system.

In such state the reduced density matrix $\rho_B$ of any block $B$ (cf. figure 2.7) has a very characteristic spectrum $\{\lambda_p\}$ (Refael and Moore, 2009): if $n_B$ is the number of bonds connecting $B$ with the rest of the system, the eigenvalue $2^{-n_B}$ appears with multiplicity $2^{n_B}$. Thus, the von Neumann entropy can be easily computed

$$S_1(B) \equiv -\sum \lambda_k \log \lambda_k = n_B \log 2, \tag{2.31}$$

i.e. the number of broken Bell pairs multiplied by $\log(2)$, which is the entropy associated to a single bond. Moreover, any $\alpha$-order Rényi entropy takes the same value of the von Neumann entropy since, within the RG approximation, the entanglement properties of the GS are independent of order $\alpha$. The validity of the renormalization scheme improves when the renormalized link is much stronger than the surrounding ones. The

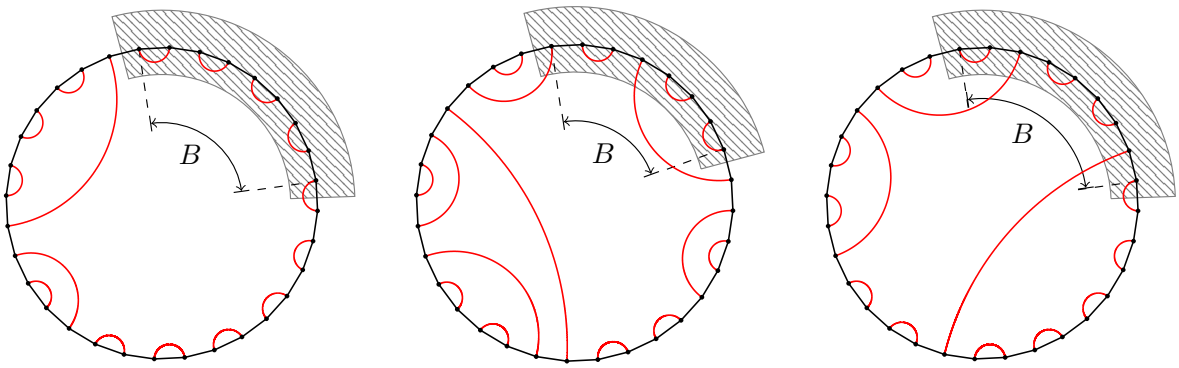


Figure 2.7: Example of bond structures for a system of size $N = 32$ with periodic boundary conditions. The entanglement entropy is proportional to the number of links connecting the block $B$ with the rest of the system: one link (left), two links (centre) and three links (right).

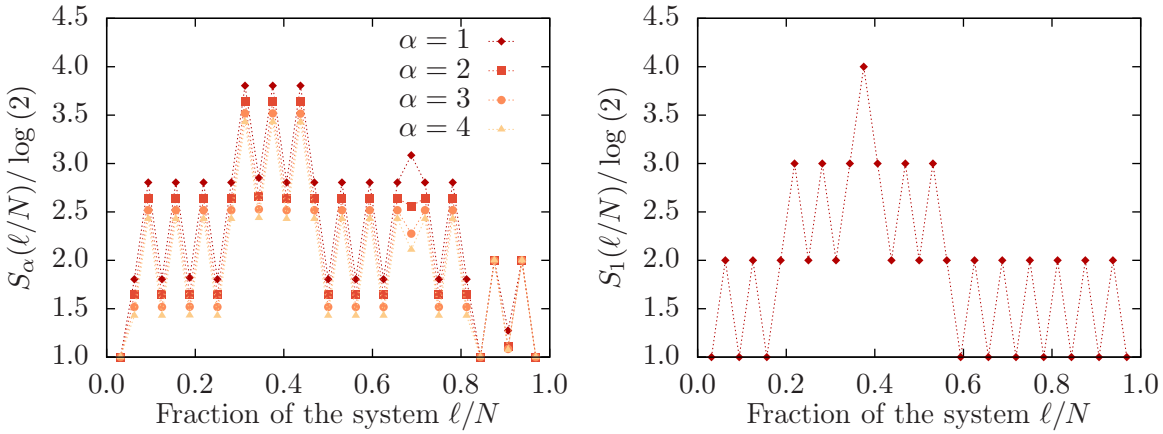


Figure 2.8: Entanglement entropy $S_\alpha(\ell)$ for one realization of the inhomogeneous XX model of $N = 32$ sites for different block size $\ell$. Left: using the exact diagonalization method. Right: using the strong disorder renormalization group method.

bond structures in figure 2.7 are also built with the same technique used to build the correlation structures in figure 2.2.

Since we are interested in the inhomogeneous hopping XX model, we can obtain the entanglement entropy using either the method of the exact diagonalization of the hopping matrix described in section 2.5 or we can use the method of strong disorder renormalization group described in this section to find the singlet bond structure which represent the GS. However, the GS of the homogeneous system, which is associated to a CFT, presents the structure of resonating valence bond (RVB), i.e. a linear superposition of valence bond states.

Figure 2.8 shows the von Neumann and the $\alpha$-order Rényi entropies for one realization of the inhomogeneous XX model with $N = 32$ sites with PBC for different block-size $\ell$ obtained by the exact diagonalization method (left) and by the strong disorder renormalization method (right). For both cases, the hopping amplitudes are chosen such that they differ by different orders of magnitude.

# Chapter 3

# Random Systems: The Random Hopping Model

## 3.1 Introduction

The interplay between entanglement in low-dimensional systems and disorder has proved to be a rich source of problems and surprises. Anderson's theorem (Anderson, 1958) states that, in one-dimensional systems with uncorrelated disorder in the local potential, all single-body states will localize and, thus, real space blocks within the ground state (GS) present nearly no entanglement. Entanglement entropy is, nonetheless, a good indicator of the localization-delocalization quantum phase transition in higher dimensions (Jia *et al.*, 2008). On the other hand, off-diagonal disorder, as it appears in the random variants of the XX or Ising models, leads in certain cases to long-range correlations and logarithmic violations of the area law.

There is ample evidence that the inclusion of strong off-diagonal disorder between nearest neighbors gives rise to a disorder-averaged von Neumann entropy with scaling corrections similar to those given by the conformal field theory (CFT) discussed in section 2.6, but with a different *effective* value for the central charge $c$ (Refael and Moore, 2009):

$$\langle S(\ell)\rangle \approx \frac{c\log d}{3}\log \ell + c', \tag{3.1}$$

where $\log(d)$ is the von Neumann entropy of the GS of a system with two sites, $d = 2s+1$ is the dimension of the local Hilbert space for the spin-$s$ particles and $\langle\cdot\rangle$ stands for the average value over disorder realizations. Indeed, the striking similarities between the clean system, i.e. homogeneous system, and the strongly disordered systems are even deeper than the expression given in equation (3.1) suggests, since they also appear in the averages for the correlation functions and the finite-size effects in entanglement (Fagotti *et al.*, 2011). Nonetheless, some other magnitudes behave in a rather different

way, such as the Rényi entropies which, unlike the clean case, coincide with the von Neumann case, as we will see in the following pages.

The aim of this chapter is to illuminate the surprising relation between entanglement in critical states, as described by CFT and the average entanglement entropies in strongly disordered systems. Let us study the random-XX model or, in other terms, the fermionic random-hopping model in 1D of $N$ sites, whose dynamics is described by the Hamiltonian

$$H = -\sum_i t_i c_i^\dagger c_{i+1} + \text{h.c.} \tag{3.2}$$

For the clean case, i.e. $t_i = t$, $\forall i$, that is the free fermion model described in section 2.2, the system is critical and the central charge of the associated CFT is $c = 1$. The factor $\log(d)$ in the Hamiltonian (3.2) is found by considering the entanglement entropy between the sites in a system of size $N = 2$, i.e. $\log(d) = \log(2)$. Thus, we have

$$\langle S(\ell)\rangle \approx \frac{\log 2}{3}\log \ell + c'. \tag{3.3}$$

Whenever the $t_i$ are different, the Hamiltonian (3.2) is called an *inhomogeneous hopping* model which, as described in section 2.5, is exactly solvable. Diagonalizing the hopping matrix one obtain the energy levels $\epsilon_k$ and the modes $v_{k,i}$, where $k$ denotes the eigenvalue index and $i$ the actual site.

When the different *hoppings* $t_i$ vary slowly with position, they can be regarded as a modulation on the propagation of the particles, or the speed of sound. Indeed, a careful choice for the $t_i$ can be used to model quantum matter on a curved space-time background (Boada *et al.*, 2011).

The modes of the Hamiltonian (3.2) have some generic mathematical properties, such as chiral symmetry (or parity symmetry): a canonical transformation $c_i^\dagger \to (-1)^i c_i^\dagger$ transforms $H \to -H$. Thus, if $\{v_{k,i}\}_{i=1}^N$ is a mode with energy $\epsilon_k$, then $\{(-1)^i v_{k,i}\}_{i=1}^N$ is also a mode with energy $-\epsilon_k$. In absence of zero modes, the GS can be proved to take place at half filling and is spatially homogeneous.

We have considered the $\{t_i\}$ to be independent random variables extracted from a probability distribution $p_\delta(t)$ pertaining to the following family

$$p_\delta(t) \equiv \frac{1}{\delta} t^{-1+\frac{1}{\delta}}, \tag{3.4}$$

where $\delta$ is a parameter that characterizes the strength of randomness. Note that $p_\delta$ is normalized for $0 < t < 1$ and $\delta > 0$

$$\int_0^1 dt\; p_\delta(t) = 1. \tag{3.5}$$

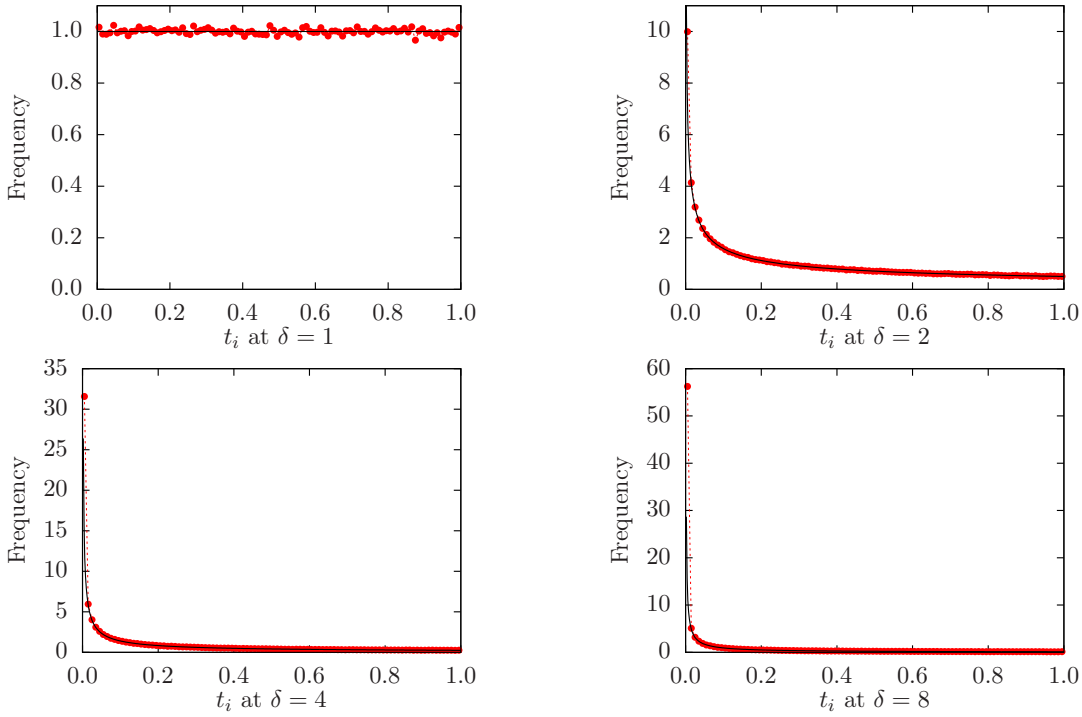


Figure 3.1: Histograms for the distribution of $t$ obtained for $10^6$ samples for different values of $\delta = 1, 2, 4, 8$. The solid line is the theoretical distribution given by equation (3.4).

See in figure 3.1 the effect of different values of $\delta$ in the range of values for $t_i$. For $\delta = 1$ (in panel top left) we obtain the uniform distribution where all values of $t$ between 0 and 1 are equally probable. For $\delta > 1$, the small values of $t$ near 0 are more probable than those near 1.

We will focus on the $\delta \to \infty$ limit, the so-called strong disorder regime (Refael and Moore, 2009), in which the sampled $t$ span many orders of magnitude in the interval $(0, 1)$. In this regime, the renormalization group (RG) derived by the fermionic system, which we introduced in section 2.7 gives an accurate description of the GS. Moreover, under successive applications of the strong disorder renormalization group (SDRG) approach, the probability distribution for the remaining hoppings, $p_\delta(t)$ flows by increasing the value of $\delta$ and $\delta \to \infty$ is the (unattainable) infinite-randomness fixed point (IRFP) (Fisher, 1995; Fisher and Young, 1998).

As we stated in section 2.7, when the SDRG method is finished, the GS can be written as a product of valence bond states. For the clean case the GS presents the structure of a resonating valence bond (RVB) which is described by the CFT. On the other hand, the GS of the system in the IRFP, presents a structure of *random valence bond* or random singlet which is not described by any CFT.

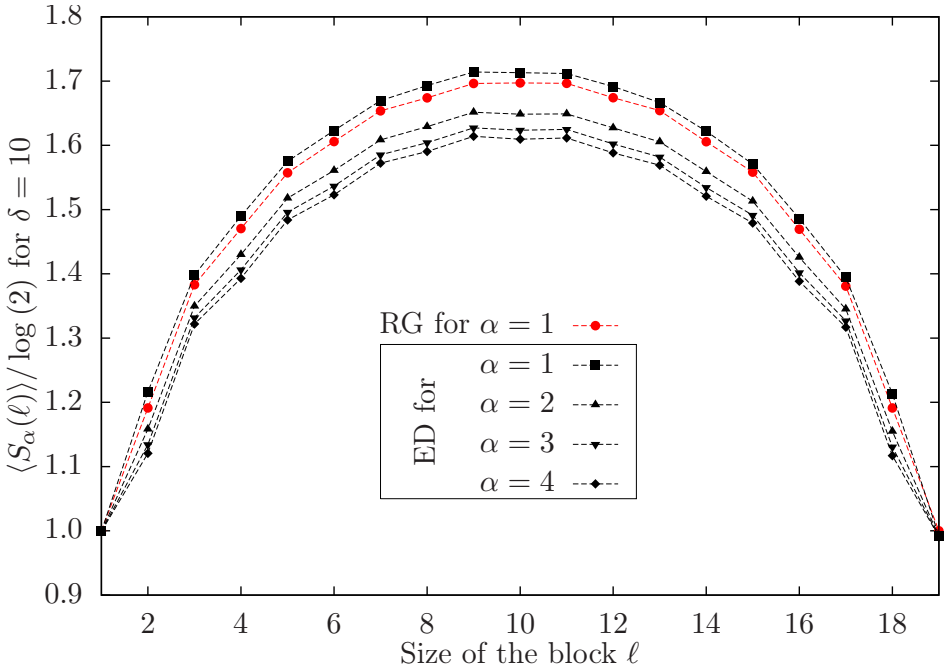


Figure 3.2: Average von Neumann and Rényi block entropies $\langle S_\alpha(\ell)\rangle$ for a $N = 20$ system with $\delta = 10$, comparing exact diagonalization (ED) and RG results for $10^6$ realizations. Notice that the RG gives the same curve for all Rényi orders, which is closest to the von Neumann entropy obtained by exact diagonalization.

## 3.2 Entanglement in the Ground State

Let $\langle S_\alpha(\ell)\rangle$ be the disorder-averaged Rényi entropy of order $\alpha$ for a block $B$ of $\ell$ sites with the rest of the system given by

$$\langle S_\alpha(\ell)\rangle = \frac{1}{N_s}\sum_{1}^{N_s} S_\alpha^{(i)}(\ell), \tag{3.6}$$

where $N_s$ is the number of samples, i.e. the different disorder realizations, and $S_\alpha^{(i)}(\ell)$ is the von Neumann entropy of the inhomogeneous system obtained in the $i$-th realization by means of the methods described in section 2.7. When $\alpha = 1$, i.e. the von Neumann entropy, we will sometimes drop the index.

Figure 3.2 compares the averaged Rényi entropies obtained with both methods exact diagonalization and RG, for a chain of $N = 20$ sites with periodic boundary conditions (PBC) and $\delta = 10$. As we discuss in section 2.7, in the strong inhomogeneity limit the SDRG approach yields the same curve for all orders of the Rényi entropy $\langle S_\alpha(\ell)\rangle$, while they differ for exact diagonalization. Notice that, while we approach the IRFP, each realization goes further in the strong inhomogeneous limit and the average entropy obtained by the RG method is closest to the $\langle S_1(\ell)\rangle$ obtained by exact diagonalization.

The difference between the RG predictions and the exact diagonalization results can be ascribed to inaccuracies in the bond-structure picture. Figure 3.3 shows a set of histograms of the values of the von Neumann entropy for two different blocks with even

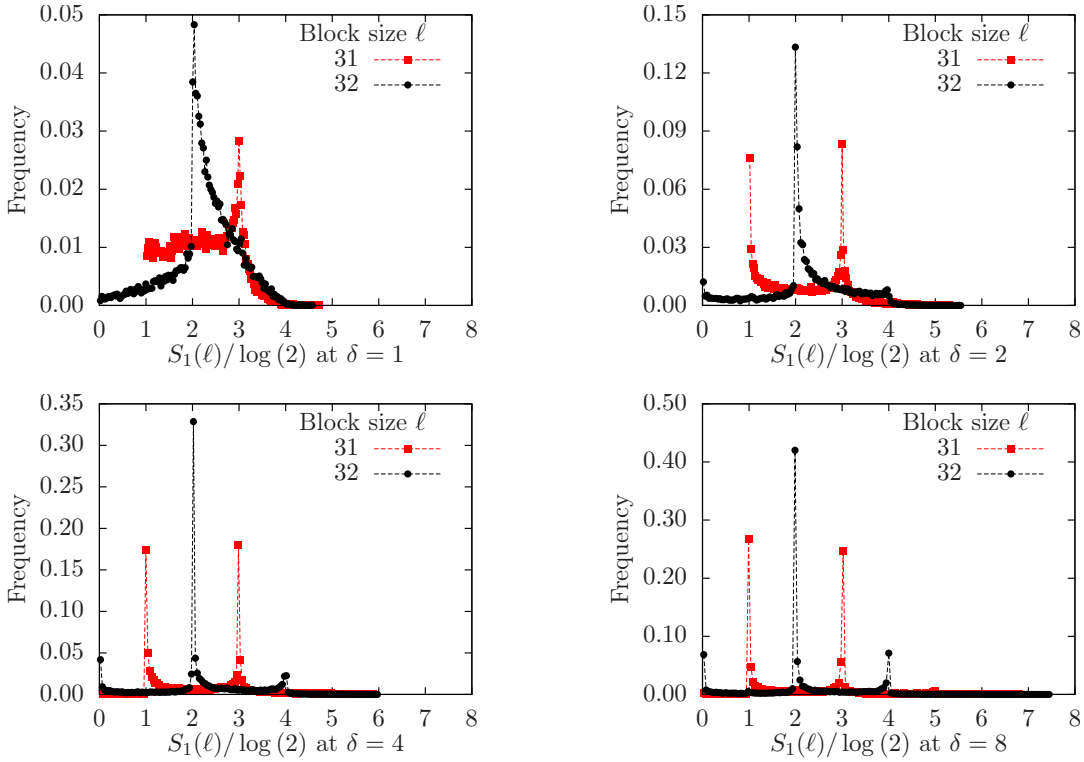


Figure 3.3: Histogram for the von Neumann entropy for odd-size blocks (red) and even-size blocks (black) for different values of $\delta$ and $N = 64$ for $2 \times 10^4$ samples.

and odd number of sites for different disorder realizations. Notice that, as $\delta$ increases, the behavior becomes closer to the bond-structure picture, which predicts a set of delta peaks at integer multiples of $\log(2)$ (Laflorencie, 2005).

The average half-chain von Neumann entropy $\langle S_1(N/2)\rangle$ is especially useful for determining the global behavior, disregarding finite-size effects. We have run five million realizations of the disorder with $\delta = 10$ and $N$ in the range from 128 to 4 096 and obtained the average half-chain entropy as a function of $N$ using the Dasgupta-Ma RG, as shown in the left panel of figure 3.4. The fit to (recall equation (3.1))

$$\langle S(\ell)\rangle \approx \frac{c \log d}{3} \log \ell + c', \tag{3.7}$$

is very accurate (Laflorencie, 2005; Refael and Moore, 2004): $\langle S_1(N/2)\rangle$ grows logarithmically with a factor $c\log(2)/3$ and the fit for $c \approx 1.00066$, i.e. very close to 1. The additive constant is $c' \approx 0.783095$.

The average entropy for blocks of different sizes is shown in the right panel of figure 3.4. We depict $\langle S_1(\ell)\rangle - \langle S_1(N/2)\rangle$ as a function of the fraction of the chain occupied by the block, $\ell/N$ using the same data. All the points collapse to a single scaling function, which we fit to a CFT finite-size form (Calabrese and Cardy, 2004)

$$\tilde{S}(\ell) = S(\ell) - S(N/2) \approx \frac{c \log(2)}{3} \log\left[\sin\left(\pi \frac{\ell}{N}\right)\right], \tag{3.8}$$

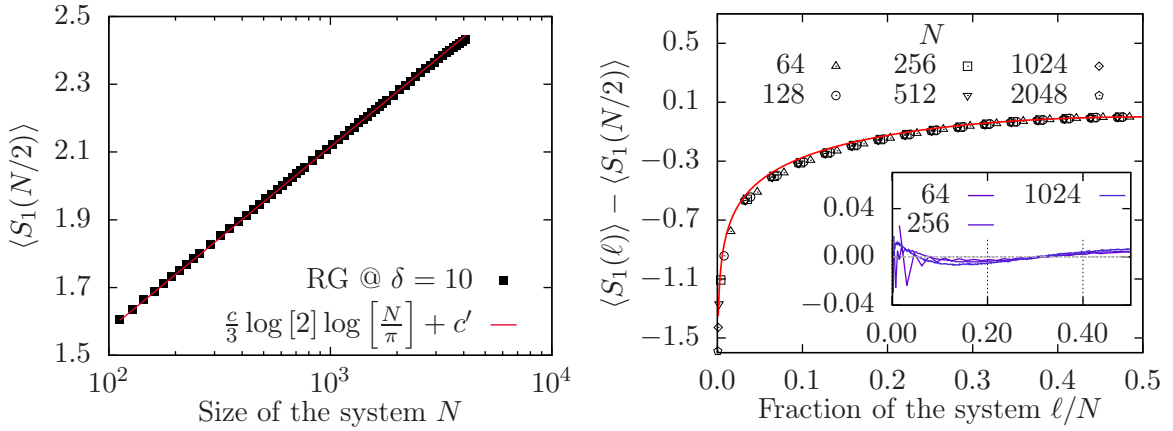


Figure 3.4: Average von Neumann entanglement entropy. Left: at half-chain $\langle S_1(N/2)\rangle$ showing the characteristic logarithmic scaling with prefactor close to $\log(2)/3$. Right: vertically shifted data $\langle S_1(\ell)\rangle - \langle S_1(N/2)\rangle$ for different system sizes $N$ which collapse into the continuous line, fitting $\tilde{S}(\ell)$. Inset: residual error when the fitted expression is compared with the data, note the presence of higher harmonics.

and plot the resulting curve along with the points. The difference between the fitting curve and the points is apparent, so we proceed to substract them and plot the result in the inset of the right panel of figure 3.4. The residual appears to correspond to *higher harmonics*, showing that a different scaling function, $Y(x)$, is required to account for the finite-size effects (Fagotti *et al.*, 2011). The Fourier series representation of that function can be written as

$$Y(x) = \left[1 + \sum_{j=1}^{\infty} k_j\right] \sin(x) - \sum_{j=1}^{\infty} \frac{k_j}{2j+1} \sin[(2j+1)x], \tag{3.9}$$

and the more general expression for the finite-size average von Neumann entropy is given by

$$S(\ell) \approx \frac{c\log(2)}{3} \log\left[\frac{N}{\pi} Y\left(\pi\frac{\ell}{N}\right)\right] + c', \tag{3.10}$$

where the contribution of the first modes provides a good approximation to the entropy. Fitting the finite-size data to this new functional form with $c = 1$, using the first mode only, we find the additive constant $c' \approx 0.7338$ and the amplitude of the first mode $k_1 = 0.1025$, which are close to the value $c' \approx 0.726$ reported by Laflorencie (2005) and the value $k_1 = 0.115$ obtained by Fagotti *et al.* (2011).

Despite the many similarities between the average behavior of entanglement in the random hopping model and a conformally invariant system in 1D, there are also substantial differences. One of the most relevant is in the Rényi entropies. In the conformal case they present characteristic parity oscillations (Xavier and Alcaraz, 2011;

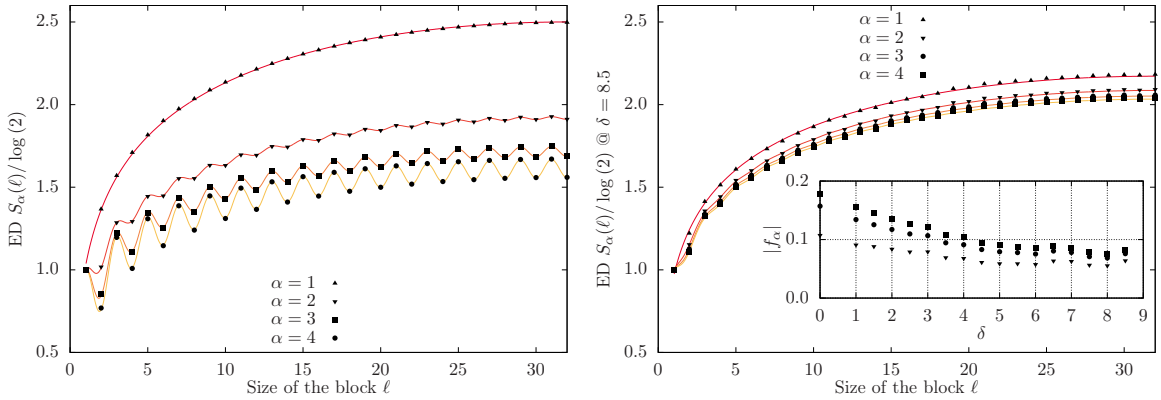


Figure 3.5: Rényi block entropies for a system of $N = 64$ sites with PBC. Left: clean case. Notice the strong parity oscillations in the higher order entropies. Right: average Rényi entropies over $2 \times 10^4$ realizations with $\delta = 8.5$. Notice how $\alpha$-order entropies become much closer and how the oscillations attenuate while $\delta$ is increased. The inset shows a decrease in the magnitude of the oscillation amplitude $f_\alpha$ in equation (3.11) as a function of $\delta$.

Calabrese and Essler, 2010):

$$S_\alpha(\ell) \approx \frac{c}{6}\left(1+\frac{1}{\alpha}\right)\log\left[\frac{N}{\pi}\sin\left(\pi\frac{\ell}{N}\right)\right] + c' + (-1)^\ell f_\alpha \left[\frac{N}{\pi}\sin\left(\pi\frac{\ell}{N}\right)\right]^{-2K/\alpha}, \tag{3.11}$$

where $c$ and $c'$ are the same as in equation (3.8), $f_\alpha$ is the oscillation amplitude, which typically increases with $\alpha$, $K$ is the Luttinger parameter ($K = 1$ in our case) and the term $(-1)^\ell$ corresponds to $\cos(2k_F\ell)$, where $k_F = \pi/2$ is the Fermi moment for half-filling. On the other hand, within the valence bond picture, all Rényi entropies are equal to the von Neumann case since, in the strong disorder regime, an $\ell$-size block has $2^\ell$-fold degenerate eigenvalues $2^{-\ell}$ (Refael and Moore, 2009). Then, the $\alpha$ order Rényi entropy is

$$S_\alpha = \frac{1}{1-\alpha}\log 2^{\ell(1-\alpha)} = \log 2^\ell = \ell \log 2. \tag{3.12}$$

Figure 3.5 compares the average Rényi entropies obtained with exact diagonalization in the clean and strongly disordered cases for a system with $N = 64$, $\delta = 8.5$ using $2 \times 10^4$ disorder realizations, for the lowest Rényi orders ($\alpha$ from 1 to 4). The left panel shows the clean case. Notice the strong parity oscillations in the higher order Rényi entropies. The right panel depicts the average Rényi entropies in the disordered case. Notice that their amplitude is substantially lower. The inset in the right panel of figure 3.5 analyses that decrease in amplitude: the $f_\alpha$ factors fitted in equation (3.11) are plotted against $\delta$, the disorder intensity. They can be seen to attenuate very slowly. In fact, even for very large $\delta$ they are still not negligible showing that, for $\alpha > 1$ the

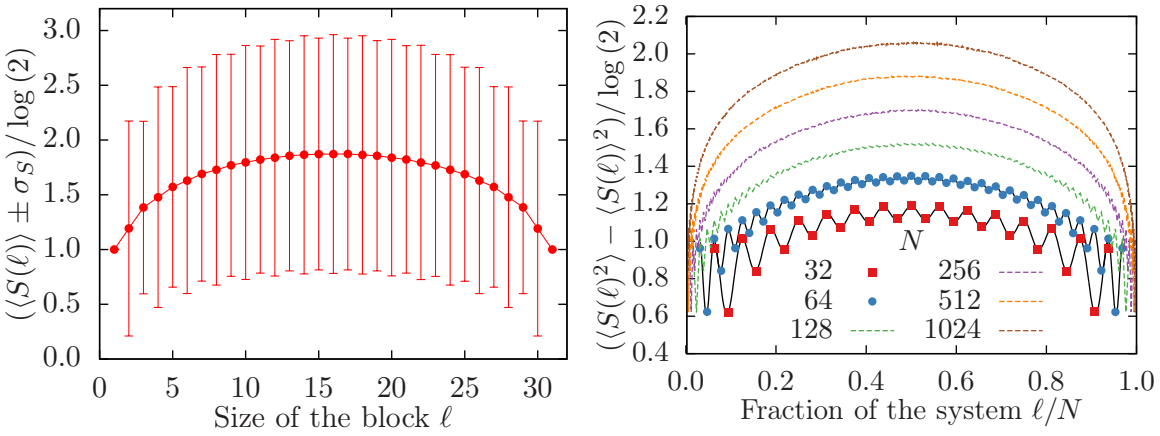


Figure 3.6: Left: average von Neumann entanglement entropy for $\delta = 8$ and $N = 32$, obtained with the RG with error bars given by the standard deviation. Notice the parity oscillation in the error bars, which are larger for even blocks. Right: variance of the von Neumann entropy distribution for different sizes and $\delta = 8$, obtained with the RG. Notice how the parity oscillations fit accurately expression in equation (3.14).

description of the subleading behavior requires the oscillating term. This was shown by Calabrese *et al.* (2010) in the clean case. Nonetheless, for infinite disorder, the effect of $f_\alpha$ will disappear.

### 3.2.1 Oscillations in higher moments

The variance of the von Neumann entropy, defined by

$$\sigma_S^2(\ell) = \langle S^2(\ell)\rangle - \langle S(\ell)\rangle^2 \tag{3.13}$$

also presents interesting universal behavior alike to the CFT predictions, but with an interesting difference: parity oscillations remain even in the strong disorder regime, as the RG calculations show. Figure 3.6 depicts the results of simulations run with $10^6$ samples for sizes $N = 32$, 64, 128, 256, 512 and 1 024, obtained with the RG and $\delta = 8$, along with a very accurate fit to a law similar to expression given in equation (3.11):

$$\sigma_S^2(\ell) = c_\sigma \log(2) \log\left[\frac{N}{\pi}\sin\left(\pi\frac{\ell}{N}\right)\right] + c'_\sigma + (-1)^\ell f_\sigma \left[\frac{N}{\pi}\sin\left(\pi\frac{\ell}{N}\right)\right]^{-2K_\sigma}, \tag{3.14}$$

with $c_\sigma \approx 0.4$, $c'_\sigma \approx 0.46$, $f_\sigma \approx 0.78$ and $K_\sigma \approx 2/3$. Remarkably, the oscillations are also present in the higher order cumulants of the distribution. They are only absent in the first cumulant, i.e. the average.

The origin of those oscillations in the variance of the von Neumann entropy and their accurate fit to the CFT expression is an open problem. These oscillations bear resemblance to the density oscillations found by Song *et al.* (2010) in a clean system, which are explained as an effect of the boundaries and subleading corrections to the CFT prediction.

Notice that the variance is always higher for the even blocks, and the even-odd difference is much larger for smaller blocks. Also let us remark that although the average number of outgoing bonds increases smoothly as we increase the block size, the probability distributions are quite different: even-sized blocks can only cut an even-number of bonds, and viceversa.

### 3.2.2 Open boundary conditions

Let us consider what are the differences in the case of open boundary conditions (OBC). In that case, translational invariance is lost: the entropy of a block depends not only on its size, but also on its distance from the extreme of the chain. It is customary to choose blocks starting from the left extreme. In that case, a block only presents one inner boundary instead of two. The CFT prediction for the clean (critical) case is that the prefactor of the logarithmic term in the expression of the von Neumann entropy is halved. In the disordered case we can also observe a reduction of the entanglement entropy, but with remarkable differences. Figure 3.7 shows the average von Neumann entropy for three sizes ($N = 32$, 64 and 128) with OBC, using $10^6$ realizations with $\delta = 8$. Notice the parity oscillations, which are similar to those appearing in the higher order Rényi entropies with PBC. In fact, a fit to a expression similar to equation (3.11) works very well (Taddia *et al.*, 2013)

$$\begin{aligned}\langle S(\ell)\rangle \approx & \frac{c_{open}}{6}\log(2)\log\left[\frac{N}{\pi}\sin\left(\pi\frac{\ell}{N}\right)\right] + c'_{open} \\ & + (-1)^{\ell} f_{open}\left[\frac{N}{\pi}\sin\left(\pi\frac{\ell}{N}\right)\right]^{-K_{open}}\end{aligned} \tag{3.15}$$

where $c_{open} \approx 1.5$, $c'_{open} \approx 0.76$, $f_{open} \approx -0.24$ and $K_{open} \approx 1$. Thus, even though the entropy is reduced in the case of open boundary conditions, the results in this case differ considerably from the expectation that $c_{open}$ should be one, but the value for $K_{open}$ agrees with previous results obtained for clean systems (Dalmonte *et al.*, 2011; Calabrese *et al.*, 2010).

### 3.2.3 Odd chains

On the other hand, disordered chains present very different behavior when the number of sites is *odd*, as opposed to the clean case. Effectively, in that case one site is not allowed to establish a bond, and entanglement is effectively reduced, see figure 3.8. Moreover, bonds can not be established over the single site and, thus, this site can be regarded as an *opening* in the boundary conditions. Effectively, the average von Neumann entropy becomes nearly flat for intermediate block sizes, showing a *plateau*.

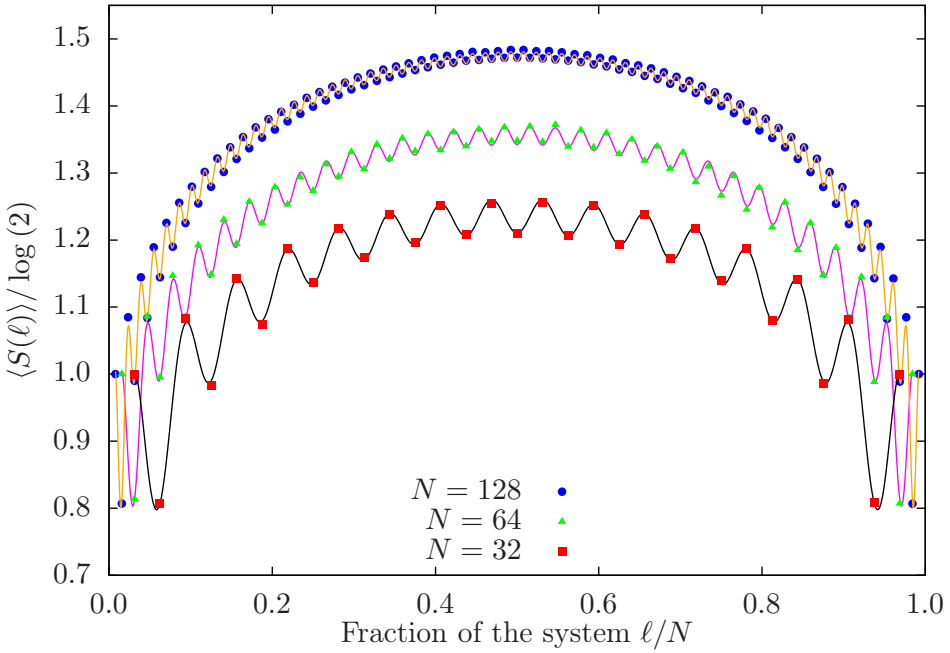


Figure 3.7: Average von Neumann entropy $\langle S(\ell)\rangle$ of the random hopping model with open boundary conditions. Notice the characteristic parity oscillations, which fit to a Luttinger parameter $K = 1/2$.

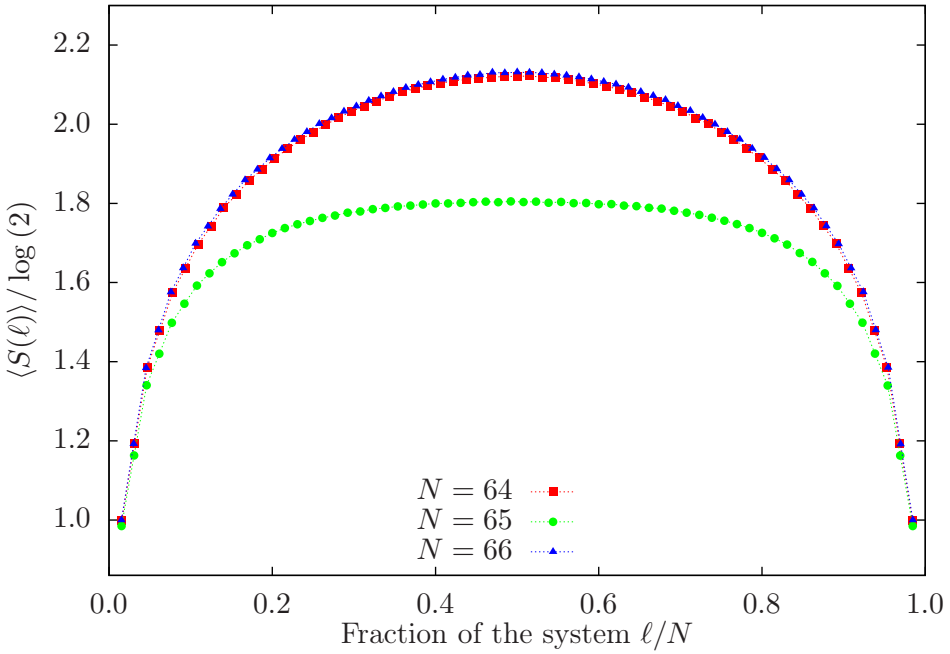


Figure 3.8: Average von Neumann entropy of the random hopping model with periodic boundary conditions for even and odd number of sites. Notice the *plateau* which gets established for intermediate block sizes in the case of odd chains.

## 3.3 Bond-length distribution

In the previous section we have discussed the entanglement structure of the random hopping model in the infinite randomness regime. It is indeed characterized by a random valence bond structure. Let us focus on the combinatorial problem of studying those bonds.

Consider a 1D random hopping chain of length $N$ and PBC, close enough to the IRFP, where the valence bond picture becomes accurate for describing the GS of the system. Given a bond between sites $i_1$ and $i_2$, let $l_b \equiv |i_1 - i_2| \pmod N$ be its length. Let us consider the probability distribution for the bond lengths, $P(l_b)$.

Hoyos *et al.* (2007) indicated a relation between $P(l_b)$ and the mean entanglement entropy in the IRFP, the aim of this section is to show that *all* entanglement properties stem from the knowledge of this distribution and the assumption of (approximate) bond independence, beyond the constraint that two bonds can never cut. The last part of the section is devoted to the introduction of a new model based solely on the analysis of random permutations and, by successive distillation of the basic physics we describe its accurate predictions for the average entropies.

The scaling behavior of $P(l_b)$ has been estimated via the Dasgupta-Ma RG (Fisher, 1994). As the RG proceeds, the typical length scale of the bonds increases. It can be argued that the likelihood of a given site surviving until the typical length scale is $l_b$ scales as $l_b^{-1}$. A bond can be established only between two surviving sites. So, if we assume independence, the probability of establishing a bond of length $l_b$ scales as the product: $P(l_b) \approx l_b^{-2}$. If that probability distribution is assumed to be exact for all (odd) values of $l_b$, the normalization constant should be

$$\sum_{n=0}^{\infty} \frac{1}{(2n+1)^2} = 8/\pi^2. \tag{3.16}$$

But for small values of $l_b$ the fitting exponent deviates from $-2$. For the scaling regime, i.e. $l_b \ll N$, the best fit is found to be $P(l_b) \approx (2/3)\, l_b^{-2}$ (Hoyos *et al.*, 2007).

The average von Neumann entropy of a block $B$ with size $\ell$ is given by the expected number of bonds crossing its boundaries, multiplied by $\log(2)$, see figure 3.9. Let the sites in the block be numbered from 1 to $\ell$ and consider site $i$ and its associated bond. Let $i'$ be the other extreme. The bond will contribute to the entropy if its length is larger than the distance to the boundary. If $i'$ is at the left of $i$, then the bond only contributes if $l_b \geq i$. The expected number of such bonds is $\sum_{l_b=i}^{N/2} P(l_b)$. If $i'$ is at the right of $i$, the bond will contribute if $l_b \geq \ell - i + 1$ and we get $\sum_{l_b=\ell-i+1}^{N/2} P(l_b)$. Summing for all $i$, and considering that leftwards and rightwards bonds are equally likely, we get:

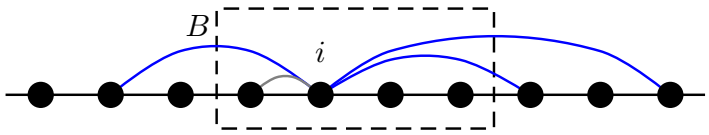


Figure 3.9: Illustration of the bond counting procedure which leads to expression in equation (3.17). Let us consider a block $B$ of size $\ell$. Bonds stemming from site number $i$ will contribute to the block entanglement only if their length is larger than their distance to the boundary (blue bonds only). Notice that actual bonds are only allowed if their length is *odd*.

$$S_1(\ell) = \frac{\log(2)}{2} \sum_{i=1}^{\ell} \left[ \sum_{l_b=i}^{N/2} P(l_b) + \sum_{l_b=\ell-i+1}^{N/2} P(l_b) \right] . \tag{3.17}$$

This expression can be recollected into a more convenient one (Hoyos *et al.*, 2007):

$$S(\ell) = \log(2) \left[ \sum_{l_b=1}^{\ell} l_b P(l_b) + \ell \sum_{l_b=\ell+1}^{N/2} P(l_b) \right] , \tag{3.18}$$

where the first term is the most relevant, since smaller bonds have the largest probabilities. Inserting the previous estimate for $P(l_b) \approx (2/3)\ l_b^{-2}$ into the first term of equation (3.18), we obtain $S(\ell) \approx [\log(2)/3]\ \log(\ell)$, as in equation (3.7).

Top panel in figure 3.10 studies the behavior of $P(l_b)$ by averaging over five million disorder realizations with $N$ ranging from 32 to 512 and $\delta = 10$, in logarithmic scale. The leading $l_b^{-2}$ behavior is apparent, as a fit for intermediate values of $l_b$ shows. The straight line corresponds to the scaling regime approximation, $P(l_b) = (2/3)\ l_b^{-2}$. The large-$l_b$ deviation, for $l_b$ comparable to the system size, is a finite-size correction.

In order to understand the finite size behaviour of $P(l_b)$, let us distribute the $N$ points uniformly in a circumference of diameter 1. The probability for a bond between sites separated $l_b$ lattice units is approximately proportional to the inverse squared of their actual distance, i.e. to their *chord*:

$$\tilde{P}(l_b) \propto \left[ \frac{1}{\sin(\pi l_b/N)} \right]^2 . \tag{3.19}$$

The accuracy of the fit to $P(l_b)$ can be further improved using an *anharmonic* chord approximation:

$$P(l_b) \propto \left[ \frac{1}{Y(l_b)} \right]^{\gamma} , \tag{3.20}$$

with $Y(l_b)$ given by expression in equation (3.9) and only retaining the first anharmonic term. The fit gives $k_1 = 0.12$ and $\gamma = 2.11$, with very good accuracy. Notice that, we

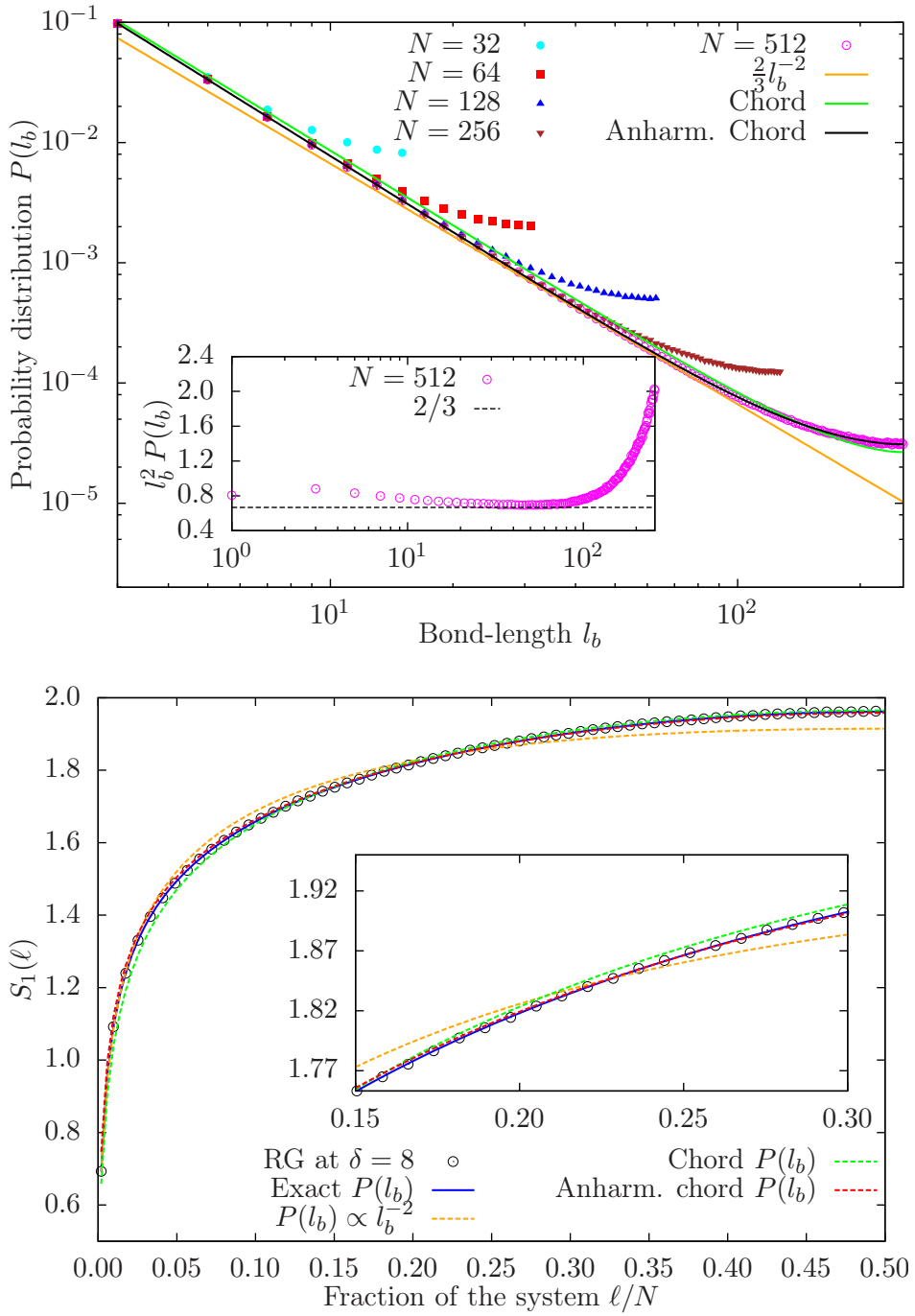


Figure 3.10: Top: Probability distribution for the bond-lengths obtained with the RG and $\delta = 8$ for different sizes. Alongside, the scaling fit to intermediate bond-lengths, $(2/3)\, l_b^2$ and the fits to the chord –equation (3.19)– and the anharmonic chord –equation (3.20)–. Inset: plot of $l_b^2 P(l_b)$, showing the approach to 2/3 during the scaling regime $l_b \ll N$. Bottom: average von Neumann entropy for $N = 512$ and $\delta = 8$ (dots), along with predictions obtained by inserting different approximations to $P(l_b)$ in equation (3.18): the scaling law $P(l_b) \propto l_b^{-2}$, the chord approximations, and the exact $P(l_b)$ obtained from the simulations. Notice that the accurate fit for this last one, validating expression in equation (3.18). Inset: detail of the same plot.

found $k_1 = 0.115$ in case of a fit for the finite-size average von Neumann entropy in section 3.2.

The bottom panel in figure 3.10 compares the average entropy $S(\ell)$ obtained by direct sampling with three possible estimates from the probability distribution for the bond-lengths using equation (3.18): (i) the scaling law $P(l_b) \propto l_b^{-2}$, (ii) the chord and anharmonic-chord laws, equations (3.19) and (3.20) and (iii) the sampled distribution for $P(l_b)$. Notice that approximation (iii) is indistinguishable from the sampled entropy.

It is interesting to ask whether the bond-length samples are actually independent or not. We have investigated the bond-length correlations. Given a bond-structure, consider the list of the bond lengths obtained when the bonds are ordered according to the index of their left-most site: $\{l_{b,1}, l_{b,2}, \cdots, l_{b,N/2}\}$. Let us consider the conditional probabilities $P(l_{b,i}|l_{b,i-1})$, i.e. the probability of finding a bond-length $l_{b,i}$ knowing that the previous bond-length was $l_{b,i-1}$. The independence assumption is equivalent to $P(l_{b,i}|l_{b,i-1}) = P(l_b)$, i.e. that knowledge of the previous bond-length is irrelevant. In fact, this assumption is *false*, e.g., after a bond of length $l_{b,i-1} = 3$, a bond $l_{b,i} = 1$ must ensue. Nonetheless, the difference $|P(l_{b,i}|l_{b,i-1}) - P(l_{b,i})|$ decays to zero very fast when $l_{b,i-1}$ grows. Since the contribution to the entropy is larger for larger bonds, the independence assumption becomes accurate in that case.

### 3.3.1 Order Statistics for the Bond-Length

Let $\pi_k(l_b)$ denote the probability distribution function (PDF) for the $k$-th longest bond. Thus, $\pi_1(l_b)$ will be the PDF for the longest bond in the system, $l_{b,\max}$. Left panel in figure 3.11 shows the histogram found over five million realizations with $\delta = 10$ for $N = 32$ and $N = 64$ with the RG. A thermodynamic limit curve appears for those relatively small sizes, with a peak at $l_{b,\max}/N \approx 0.2$, i.e. the longest bond covers approximately 1/5 of the total system. After the maximal bond, the curve appears almost flat, up to 1/2, which is the maximal realizable value.

The independence assumption allows us to give an estimate for $\pi_1(l_b)$. Let $X$ be a 1D random variable with probability distribution $p(X)$ and $X_{\max,N}$ represent the maximal observation out of a series of $N$ independent realizations. The probability distribution for $X_{\max,N}$ can be found this way: (i) find the cumulative distribution function (CDF) for $X$: $F(x) \equiv P(X > x) = \int_{-\infty}^{x} p(s)\, ds$; (ii) the CDF for the maximal observation is just $P(X_{\max,N} > x) = F(x)^N$; (iii) the probability distribution for the maximal observation is found by differentiation of the CDF: $P(X_{\max,N}) = \partial_x \left[F(x)^N\right]$. Since we have $N/2$ bonds in our system, the CDF for the maximal bond will be $F(l_b)^{N/2}$. Assuming a continuous PDF $P(l_b) \propto l_b^{-2}$, we get the estimate

$$\pi_1(l_b) \propto \left(1 - \frac{1}{l_b}\right)^{N/2-1} \left(\frac{1}{l_b^2}\right). \tag{3.21}$$

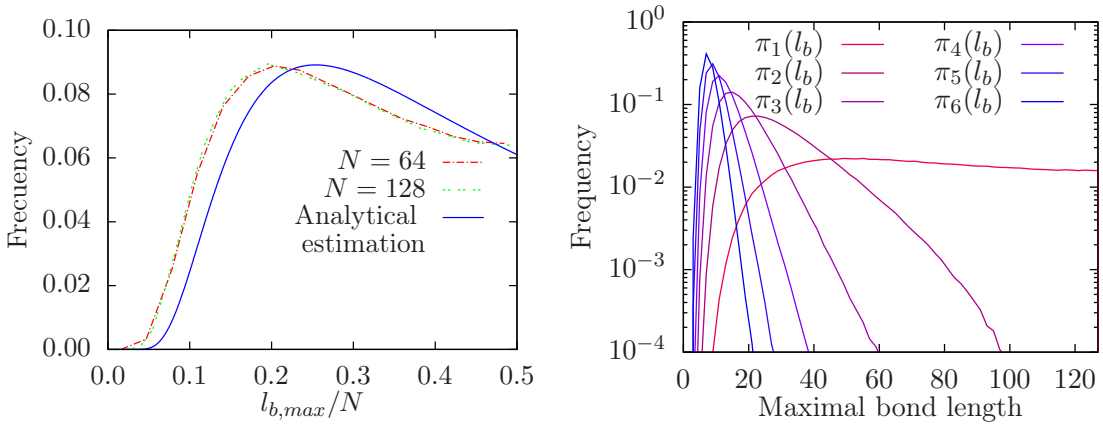


Figure 3.11: Left: Histogram for the maximal bond-length as fraction of the system $l_{b,\max}/N$ in the IRFP ($\delta = 10$). Notice how both curves seem to converge to a thermodynamic limit. For low $l_{b,\max}$, the probability increases fast up to a a value $l^M_{b,\max}/N$, which is close to 0.2. The continuous curve corresponds to the estimate for $\pi_1(l_b)$ given in equation (3.21). Right: Probability distribution functions for the $k$-th longest bond in a chain with 256 sites, with $\delta = 10$ and $10^6$ realizations.

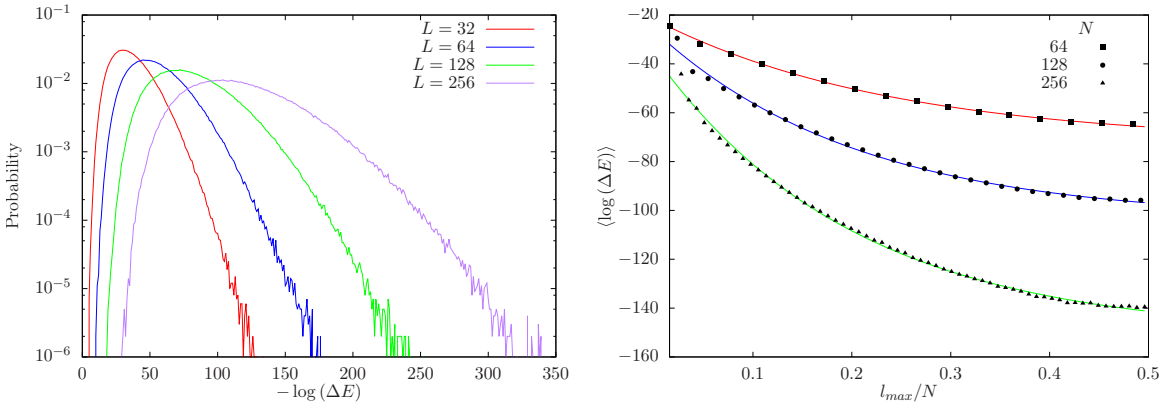


Figure 3.12: Left: Log-Log behaviour of the probability of the logarithm of the energy gap. Right: Average logarithm of the energy gap as a function of the $l_{b,\max}$ in each realization, for three system sizes ($N = 64$, 128 and 256), and $\delta = 8$. Alongside, fit to functional form given by equation (3.22).

This estimate, which is plotted in left panel in figure 3.11, can be used to find the value of $l^M_{b,\max}$, the most likely maximal bond-length. In the thermodynamic limit, $l^M_{b,\max} \approx N/4$. Right panel in figure 3.11 depicts the different $\pi_k(l_b)$, i.e. the PDF for the $k$-th longest bond, for a system with 256 sites and $10^6$ disorder realizations. Notice how they become more and more peaked as $k$ increases.

### 3.3.2 Longest bond and energy gap

The average energy gap $\Delta E$ is known to vanish very quickly in the thermodynamical limit (Fisher, 1994) otherwise, the area law should be satisfied. The left panel in figure 3.12 shows the log-log behavior of the probability of the logarithm of the energy gap, $-\log(\Delta E)$.

In this section we will consider the relation between the average gap and entanglement. Since energy scales are linked to length scales, the connection is made via the longest bond. We have applied the RG method to $10^6$ disorder realizations with $\delta = 8$ for systems of $N = 64$, 128 and 256. The average value of $\log(\Delta E)$ for each value of $l_{b,\max}$ fits to an exponential decay (see the right panel in figure 3.12):

$$\langle \log(\Delta E) \rangle \approx A + B \exp\left(\frac{-l_{b,\max}}{l_0}\right). \tag{3.22}$$

For all attempted values of $N$, $l_0 \approx N/5$, i.e. the expected value for the maximal bond-length.

## 3.4 Random permutations

A simple model can be devised which reproduces most features of the ground state of the random hopping model, in which all the disorder effects are collected into a model of *random permutations*.

Let us consider a variant of the random hopping model in which each new disorder realization is associated with a random permutation $\sigma$ of the set $\{1, \cdots, N\}$. Let us associate the $i$-th element of the permutation, $\sigma_i$, to the $i$-th hopping term of the chain: $t_i = \exp(-\sigma_i)$. The rationale is that the renormalization rule equation (2.30) becomes now additive in the values of $\sigma_i$:

$$\sigma_i^{(R)} = \sigma_{i+1} + \sigma_{i-1} - \sigma_i, \tag{3.23}$$

i.e. the lowest element of the permutation is removed, along with its two neighbors and all three are replaced by a renormalized element. Each random permutation determines a bond-structure, which in turn determines all the correlation and entanglement properties within the GS of the system. Thus, we conjecture that sampling over disorder realizations amounts to sampling over random permutations, i.e. a discrete set of possibilities. Random permutation theory has already made appearance in other areas of physics, such as the statistical mechanics of growing interfaces (Kriecherbauer and Krug, 2010), where it links the shape fluctuations in the Kardar-Parisi-Zhang (KPZ) universality class with the Tracy-Widom probability distributions from random matrix theory.

Our RG flow in the permutation space is not perfectly determined. It sometimes finds *coincidences*, i.e. despite all elements are initially different, after some RG steps, some of them will coincide. If the coinciding elements are sufficiently far apart, the order in which we renormalize them is immaterial. In a few cases, they are close enough, thus forcing to choose one of them randomly in order to proceed. Nonetheless, those coincidences get more and more sparse as the system size grows, and become negligible in the thermodynamic limit.

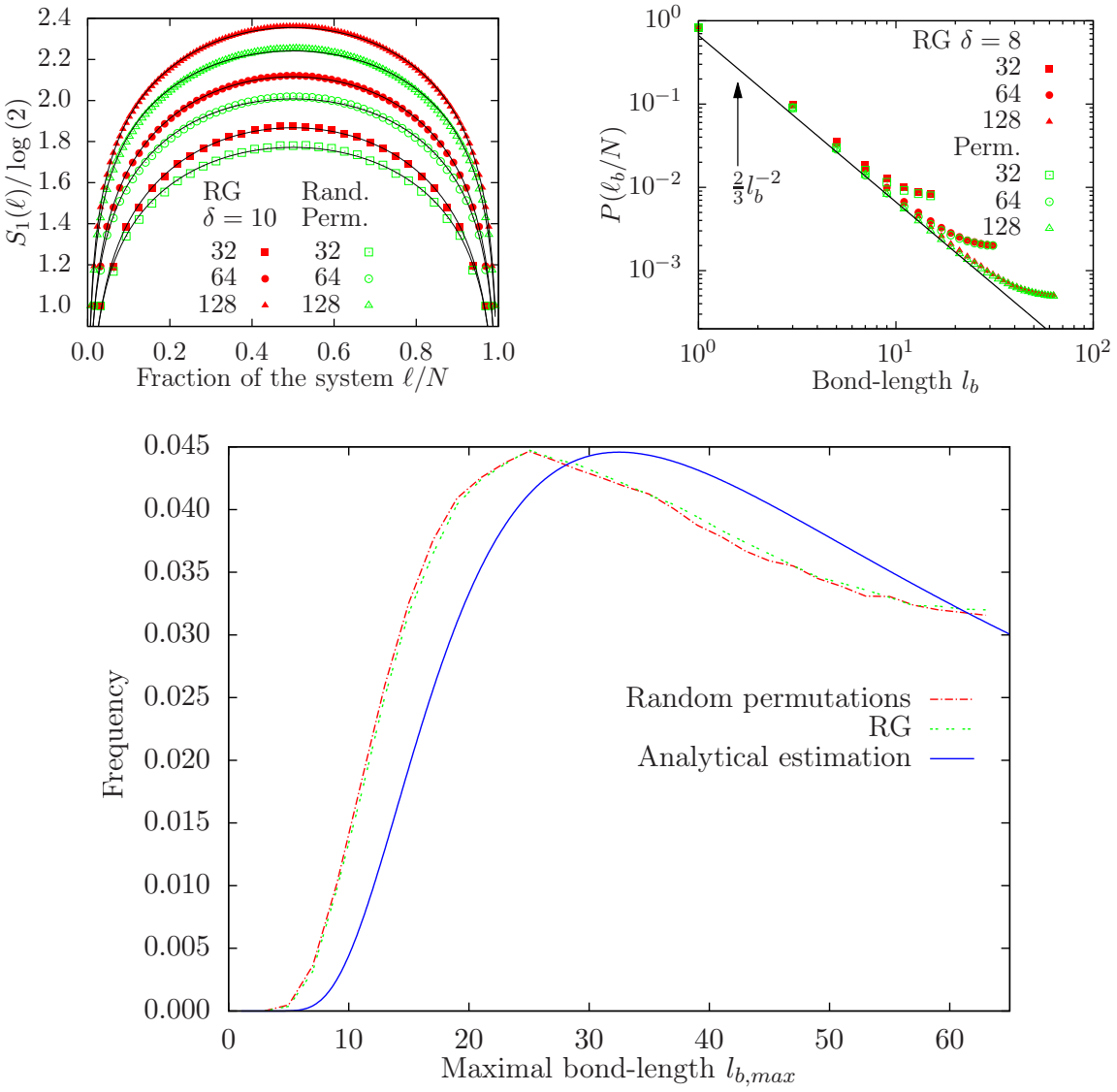


Figure 3.13: Study of entanglement of the ground state of the random permutations model. Top-left: average von Neumann entropy as a function of $\ell/N$, for $N = 32$, 64 and 128. Top-right: Histogram for the bond lengths, $l_b$. Bottom: Histogram for $l_{b,\max}/N$ obtained by RG and random permutations for $N = 128$. Notice how both curves seem to converge to a thermodynamic limit. For low $l_{b,\max}$, the probability increases fast up to a a value $l^M_{b,\max}/N$, which is close to 0.2.

| | Permutations | | | RG | | |
|---|---|---|---|---|---|---|
| $N$ | $c$ | $c'$ | $\chi^2/10^{-4}$ | $c$ | $c'$ | $\chi^2/10^{-4}$ |
| 32 | 1.043 | 0.567 | 2.2 | 1.167 | 0.519 | 2.3 |
| 64 | 1.047 | 0.557 | 1.4 | 1.148 | 0.524 | 1.0 |
| 128 | 1.048 | 0.547 | 1.2 | 1.124 | 0.538 | 0.5 |

Table 3.1: Fitting values for the von Neumann entanglement entropy (see equation (3.8)) to compare the model of random permutations and the RG method for $\delta = 10$ and $5 \times 10^6$ samples.

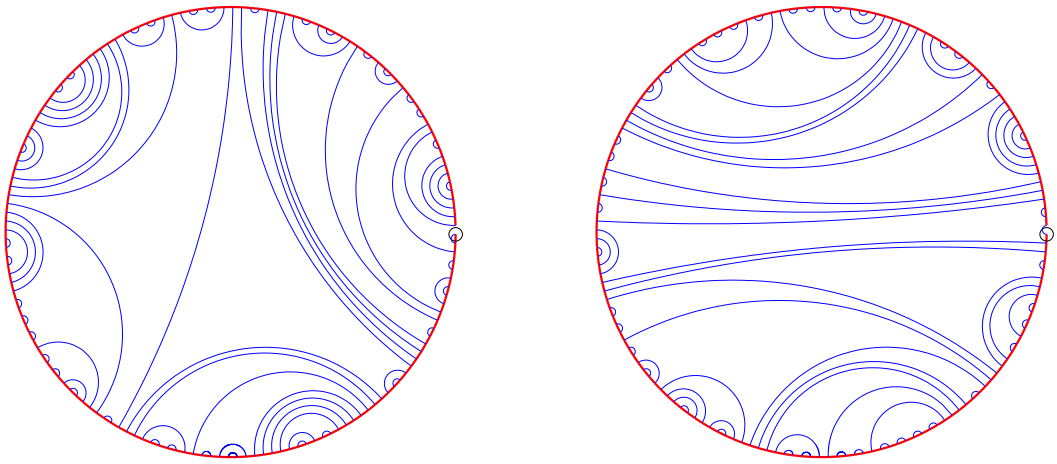

Figure 3.14: RNA folding structures for $N = 160$ to exemplify the scaling relation $\eta + \chi = 2$ with $\eta \approx 1.44$ and $\chi \approx 0.56$.

Let us show that the Dasgupta-Ma RG and the random permutations model give the same results for the entanglement. As it was discussed above, all the relevant magnitudes stem from a single function: the probability distribution for $P(l_b)$. Figure 3.13 shows runs performed for $10^5$ samples for $N = 32$, 64 and 128 for the average von Neumann entropy (top-left), bond length histogram (top-right) and maximal bond length histogram (bottom), along with comparison with the Dasgupta-Ma RG approach. See table 3.1 to compare fits to equation (3.8).

The main feature of the random permutations model is the strong hierarchy among the link strengths. Our model bears strong similarities to the *hierarchical model* of RNA-folding (Müller, 2003; David *et al.*, 2008). In this model, random binding energies are provided for each pair of sites on a 1D chain and bonds are established among them in order with a no-crossing condition. Renormalization group arguments show that the universality class is captured merely by choosing the $N(N-1)/2$ binding energies $\epsilon_{ij}$ such that $\epsilon_{i_1 j_1} \ll \epsilon_{i_2 j_2} \ll \cdots \ll \epsilon_{i_{N(N-1)/2} j_{N(N-1)/2}}$. This RNA model can be considered an infinite-dimensional version of the random hopping model. Indeed, the bond-length distribution and the average entropy are characterized by critical exponents: $P(l_b) \approx l_b^{-\eta}$ and $S(\ell) \approx \ell^{\chi}$. In our 1D case, $\eta = 2$ and $\chi = 0$ (because of the logarithmic behavior).

In the infinite-dimensional RNA case, $\eta \approx 1.44$ and $\chi \approx 0.56$ (See figure 3.14 for an example). They both follow the scaling relation found by David *et al.* (2008), that $\eta + \chi = 2$.

## 3.5 Entanglement in Low-energy Excited States

The entanglement of excited states has been studied recently within the CFT framework (Alcaraz *et al.*, 2011; Ibáñez Berganza *et al.*, 2012; Taddia *et al.*, 2013; Dalmonte *et al.*, 2012; Eloy and Xavier, 2012; Essler *et al.*, 2013). In this section we will extend the techniques developed for the study of entanglement in free fermion systems to study the excited states of the random hopping model. Indeed, entanglement of all eigenstates can be constructed using either exact diagonalization, the fermionic version of the Dasgupta-Ma RG or random permutations approaches.

As has been stated in section 2.7, the eigenstates of the hopping matrix constitute the single-body modes: bonds between pairs of sites, with negative energy and their corresponding anti-bonds, with positive energy. The GS is obtained by filling up the set of all negative energy modes, i.e. all the bonds and none of the anti-bonds. As discussed in section 2.2, the full spectrum of the Hamiltonian is obtained as we either reduce the number of particles to allow empty modes and/or add particles in modes with positive energy. Both negative and positive energy modes, bonds and anti-bonds, provide the same contribution to the entanglement entropy but, when both are present on the same pair of sites, their contribution to entanglement cancels out, leaving two factorized sites.

Figure 3.15 shows the von Neumann entanglement entropy for a clean system of size $N = 32$, the entanglement entropy increases substantially when a particle-hole (PH) excitation is created, i.e. when a particle in an occupied mode is upgraded to an empty state above the Fermi level (Ibáñez Berganza *et al.*, 2012; Essler *et al.*, 2013). Moreover, entanglement remains invariant for *compact states*, i.e. states in which the list of occupied modes presents no holes. Those states are represented by vertex operators.

The situation is very different for the strongly disordered system. Figure 3.16 illustrates the different types of excited states and their effects on entanglement. In the top-left panel we show a possible bond structure describing the GS. The lowest energy excitation is the compact state obtained by either removing the weakest bond or adding a particle on the weakest anti-bond. Both cases result in the longest bond being removed from the system, as shown in the top-right panel. A second compact excitation can be obtained by removing/adding a further particle, as shown in the bottom-left panel. The last panel shows the effect of a PH excitation, in which the longest bond is upgraded to be an anti-bond, which leaves the entanglement structure untouched.

Let $|x\rangle$ denote the excited state in which $x$ particles have been removed from the GS (equivalently, we could say added), and let $S(\ell, x)$ denote the average von Neumann entropy of a block of size $\ell$ within state $|x\rangle$. Left panel in figure 3.17 shows

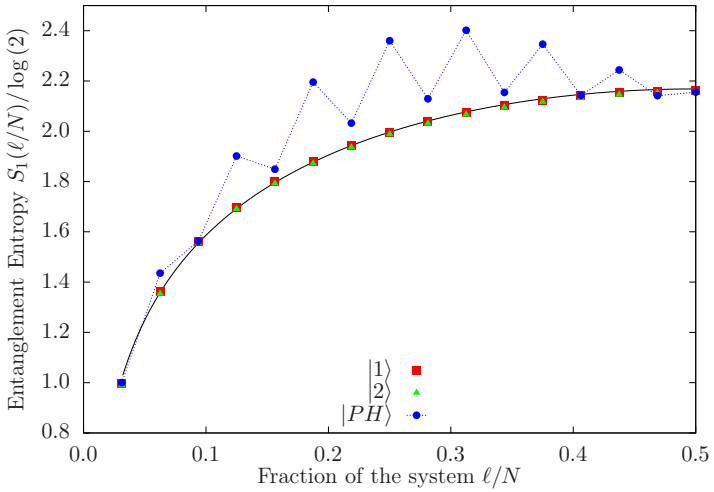


Figure 3.15: Entanglement entropy for low-energy excited states in a clean system of size $N = 32$. The solid line is a fit for the entanglement entropy of the ground state.

this average von Neumann entropy for the GS and three excited states, obtained with exact diagonalization and the RG. The first one, the PH excitation, coincides with the entanglement of the GS. The other two correspond to states $|1\rangle$ and $|2\rangle$, in which one ($S(\ell, 1)$) or two ($S(\ell, 2)$) particles are added or removed. Notice that, in this case, a *plateau* appears for intermediate block sizes, similar to the one appearing for the GS of odd-sized systems. The right panel of figure 3.17 shows how this plateau reduces slowly its height as the number of added/removed particles increases, i.e. the curves $S(\ell, x)$ flatten progressively for increasing $x$.

Left panel in figure 3.18 shows the behavior of $S(\ell, 1)$ for sizes ranging from $N = 32$ to $N = 2048$, as obtained with the RG. All of them present a similar plateau, but at increasing heights. Notice that the sizes are in geometric progression, and the plateau heights appear to grow only arithmetically. This shows that the behavior of $S(N/2, 1)$ is *logarithmic* with the system size $N$. Indeed, let us claim that

$$S(N/2, x) = \frac{c_{ex} \log(2)}{3} \log(N) + c'_{ex}(x). \tag{3.24}$$

with $c_{ex} = 1$. This claim receives support from the results shown in the right panel of figure 3.18, which shows $S(N/2, x)$ as a function of $N$ (in logarithmic scale), for different values of $x$. Notice that all curves are, in fact, parallel straight lines and the slope is indeed close to $\log(2)/3$. The additive constant $c'_{ex}(x)$ is the only difference and its decay with $x$ is shown in the inset of figure 3.18. For the $x = 1$ case, the reduction in the value of the additive constant from the GS can be explained by assuming a reduced *effective system size*, from $N$ to $N/5$, i.e. $c'_{ex}(1) \approx c' - \log(2)\log(5)/3$. This reduction in the effective system size can be explained if we assume that it coincides with the *length of the expected maximal bond* discussed in section 3.3.1.

The curves $S(\ell, 1)$ for different sizes collapse when the maximum value is substracted

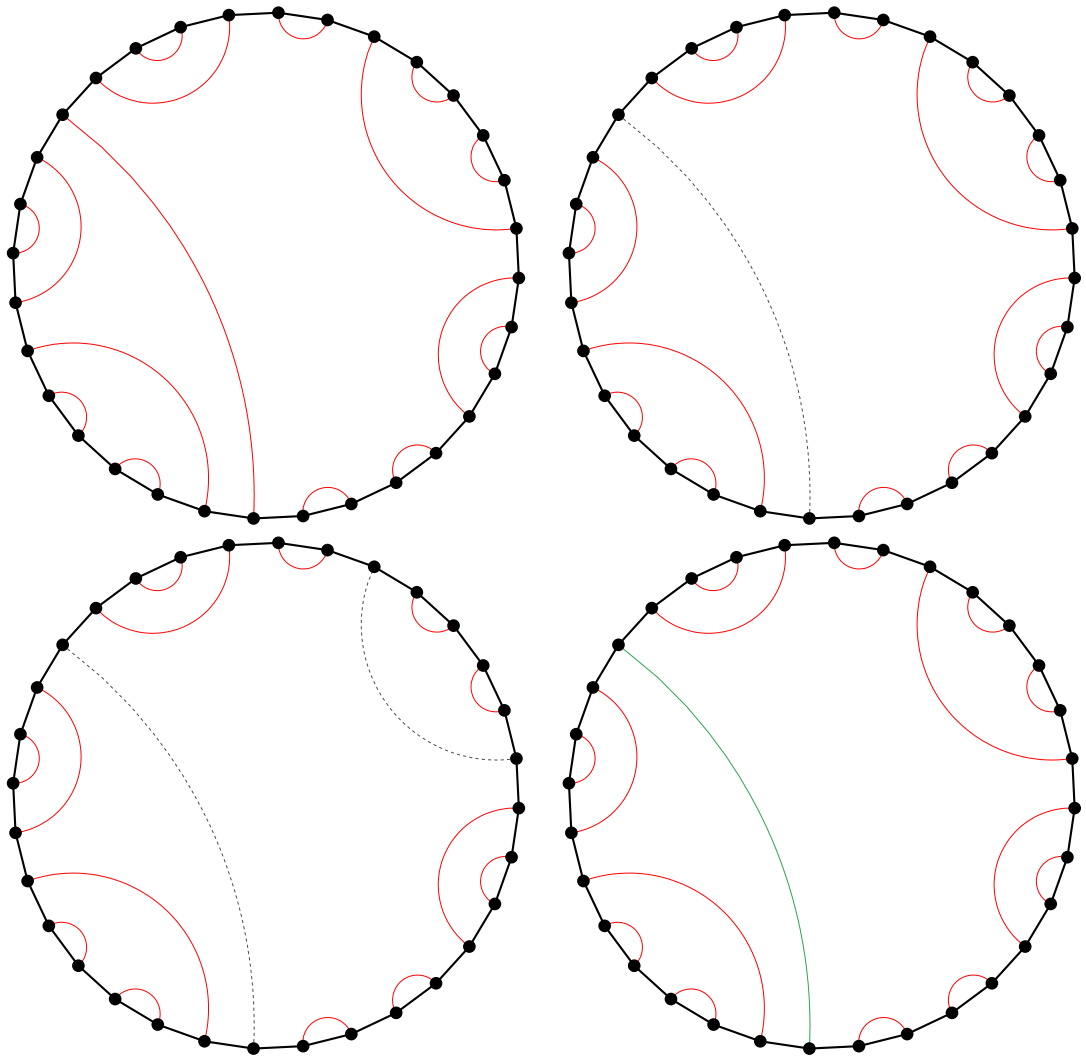

Figure 3.16: Pictorial representation of the excited states. Top-left: Bond-structure of the ground state $|0\rangle$. Top-right: the excited state $|1\rangle$ is obtained by removing the longest bond. Bottom-left: if the second longest bond is removed, the excited state $|2\rangle$ is obtained. Bottom-right: the particle-hole state is built by upgrading the closest particle to the Fermi point to the first mode above it. Due to the particle-hole symmetry, in our case we upgrade the longest bond to the corresponding anti-bond, which presents the same entanglement.

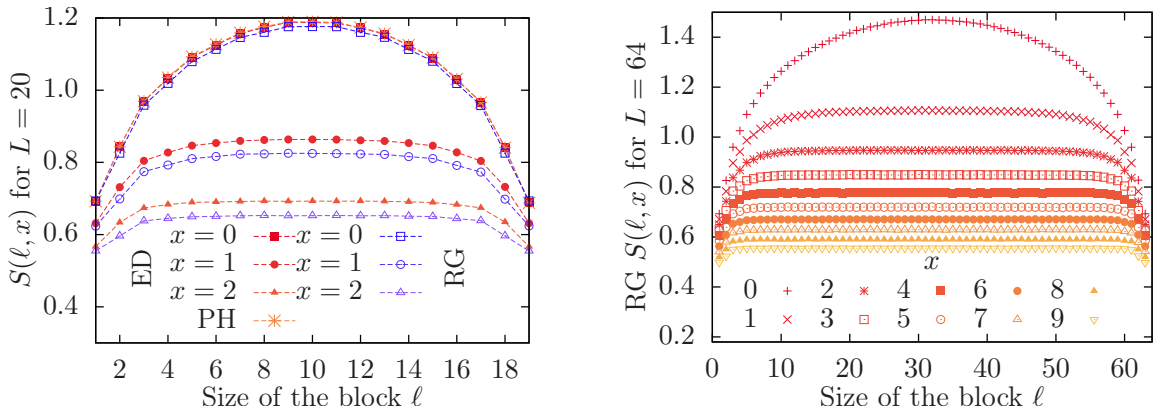


Figure 3.17: Average von Neumann entropy $S(\ell, x)$ at $\delta = 10$. Left: the ground state and low-energy excited states, both with exact diagonalization (solid points) and RG (empty points) for a system of $N = 20$ and $\delta = 10$. Note the decrease of the entropy in the case of excited states $|1\rangle$ and $|2\rangle$, and the invariance for the PH excitation. Right: $S(\ell, x)$ for a system of $N = 64$ sites for different number of removed/added particles $x$ ($x = 0$ corresponds to the ground state).

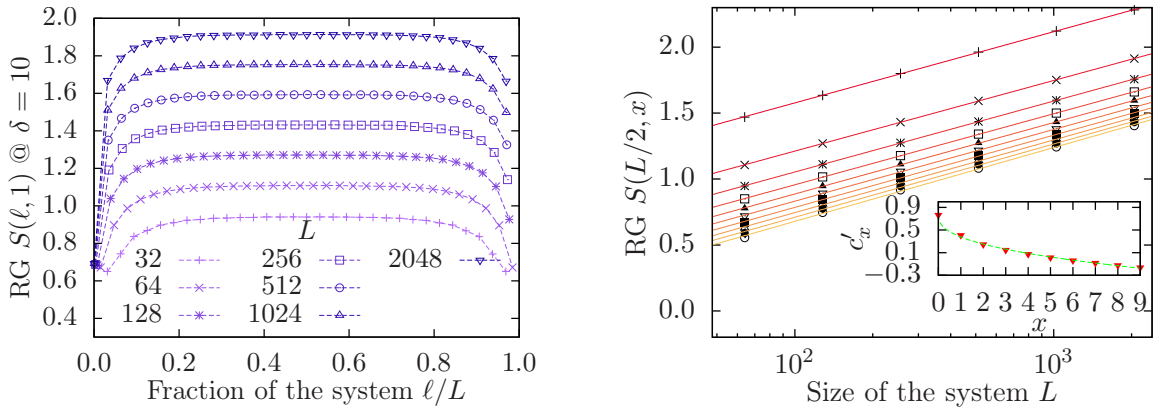


Figure 3.18: Left: $S(\ell, 1)$ for different system sizes $N = 32$, 64, 128, 256, 512 and 1024. Notice that while the sizes grow geometrically, the maximal values of the entropy grow only arithmetically. Right: height of the *plateau* of $S(N/2, x)$ for $0 \leq x \leq 9$ (sorted from top to bottom) as a function of the system size, in solid lines represent the fit to expression given in equation (3.8), and the inset shows the additive constant as function of the removed particles $c'_{ex}(x) = c'_0 - a \log(2) x^b$ with fitting parameters $(a = 0.56, b = 0.4)$.

from the entropy values and, in the thermodynamic limit, they fit to the finite-size form:

$$S(\ell, 1) \approx \frac{c \log(2)}{3} \log(N) + c'_x - \beta e^{-\gamma\sqrt{\ell/N}} \tag{3.25}$$

where $\gamma \approx 10$ allows us to estimate the size of the region in which entropy grows to reach the value $S(N/2, 1)$ as approximately $1/5$ of the total size of the system. Remarkably, $N/5$ is again the average size of the bond of maximal length (cf. left panel of figure 3.11).

From all those analysis we can attempt a physical picture of the entanglement in the first excitation. Removal of the weakest bond is usually the same as a removal of the longest bond, which has a typical size $l_{b,\max} \approx N/5$. Since bonds can not cross, entanglement can grow normally only *within* the region of size $\approx N/5$ which lies under this longest bond. The region outside, with size $4N/5$, is devoid of long bonds, and contributes less to the entanglement. Similar arguments apply for the higher excitations.

# Chapter 4

# Engineering the Inhomogeneity: the Rainbow State

## 4.1 Introduction

The role of coupling inhomogeneity in 1D quantum many-body physics has been addressed from many different points of view. As discussed in chapter 3, quenched disorder in the couplings gives rise to ground states (GSs), which, when averaged, resemble quantum critical states. On the other hand, if the couplings change smoothly enough, they can be regarded as a position-dependent speed of propagation for the excitations, or a local gravitational potential (Boada *et al.*, 2011). Thus, a slow decrease of the couplings to zero can be regarded as a *horizon*. Smoothed boundary conditions, in which the couplings fall to zero in the borders, have been used to reduce the finite-size effects when measuring bulk properties of the GS (Vekić and White, 1993). Moreover, an exponential dependence of the couplings with position is a characteristic of Kondo-like problems (Okunishi and Nishino, 2010) and a hyperbolic dependence, has been used to study the scaling properties of non-deformed systems (Ueda and Nishino, 2009; Ueda *et al.*, 2010).

As we discussed in section 1.4, geometry and quantum structure are linked via the so-called *area laws* (Srednicki, 1993; Eisert *et al.*, 2010). In 1D, the area law means that $S_A$ is bounded by a constant independent on the size of $A$. This statement was proved by Hastings (2007), assuming that the Hamiltonian has finite range (locality), with finite interaction strengths and a gap in the spectrum. Thus, violations of the area law in 1D should therefore come from sufficiently non local Hamiltonians, divergent interaction strengths or gapless systems. The category of gapless systems is the most studied, it includes translational invariant critical systems which are described by a conformal field theory (CFT), for which the gap decays with the system size $N$ as $1/N$, as it was discussed in section 2.6. The area law is nevertheless restored by a massive perturbation leading to an entanglement entropy proportional to the logarithm of the

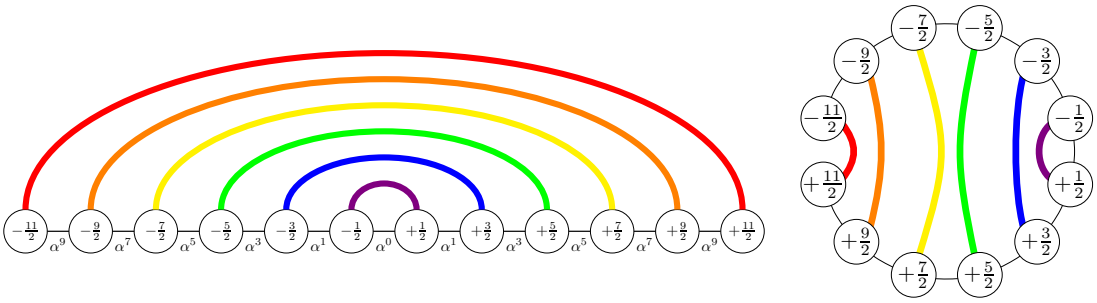


Figure 4.1: Rainbow state both in linear and circular representations, showing the $(-k, +k)$ bonds above the central link. Thus, the entanglement entropy of the left (or right) half of the chain is $L \log 2$.

correlation length in the scaling regime (Calabrese and Cardy, 2004). Other possible violations to the area-law have been also investigated, by means of long-range couplings with a magnetic phase and a Fermi surface with a point of accumulation (Gori *et al.*, 2014) or by the control of the GS degeneracy in a supersymmetric lattice model (Huijse and Swingle, 2013).

A strong violation of the area law takes place in an inhomogeneous XX model in 1D where the exchange couplings between consecutive sites decay exponentially outwards from the center of the chain. In this model, introduced by Vitagliano *et al.* (2010), the decrease of the couplings yields a vanishing gap in the thermodynamic limit, allowing for a violation of the area law, which turns into a *volume law*.

The aim of this chapter is to study how, by tuning the exponential factor, the GS of the system evolves smoothly from a logarithmic law towards a volume law for the entanglement entropy between the left and the right halves of the chain (Ramírez *et al.*, 2014b, 2015).

In the strong inhomogeneity regime, i.e. when the decay of the couplings is very fast, one can use the Dasgupta and Ma (1980) renormalization group (RG) that has been applied successfully to strong disordered fermionic systems with the scheme introduced in section 2.7. The GS is the product state of Bell-pairs symmetrically distributed around the center of the system, as shown in figure 4.1. This resulting GS turns out to be a valence bond state formed by bonds joining the sites located symmetrically with respect to the center. This state was termed *concentric singlet phase* by Vitagliano *et al.* (2010) or simply, *rainbow state* (Ramírez *et al.*, 2014b). The entanglement entropy of half of the chain is given essentially by the number of bonds connecting the left and the right halves. Thus, the volume law for strong inhomogeneous chains can be easily understood from the rainbow picture.

However, for weak inhomogeneities the rainbow picture does not hold because the GS is a *resonating* valence bond state that satisfies a volume law plus logarithmic corrections (Ramírez *et al.*, 2014b, 2015). Thus, we study the model in the weak inhomogeneity regime and its relation to the uniform limit given by a CFT, namely a massless Dirac fermion with open boundary conditions (OBC). One might think that some scaling

limit of the model would correspond to a perturbation of the underlying CFT. However, the perturbation cannot correspond to local operators added to the action, since they do not give rise to volume law entropies. Quite surprisingly, the solution of this puzzle is still provided by the CFT: the GS is a sort of thermal state that satisfies a volume law, with a temperature related to the exponential factor of the hopping amplitudes. From this perspective, the appearance of a volume law in the GS of the model is not surprising at all since, after all, it corresponds to a thermal state. Yet, it comes as a surprise that the state remains pure. The understanding of this apparent contradiction will bring us to unexpected territories that we shall start to explore.

## 4.2 The rainbow state model

Consider an inhomogeneous 1D fermionic system of $N = 2L$ sites with OBC, whose dynamics is described by the Hamiltonian

$$H = -\sum_{i=1}^{N-1} t_i c_i^\dagger c_{i+1} + \text{h.c.} \tag{4.1}$$

where $t_i$ are hopping amplitudes which we are able to engineer, $c_i$ and $c_i^\dagger$ are annihilation and creation operators of spinless fermions on the $i$-th site. As we said in section 3.1, the Hamiltonian (4.1) presents chiral symmetry, for any set of values $t_i$, which implies that for every single-particle eigenstate with energy $\epsilon$ there is another eigenstate with energy $-\epsilon$, which is related by swapping the sign of the components of all odd sites. Thus, the ground state takes place at half-filling. Moreover, the occupation number of every site $i$ is $\langle n_i \rangle = 1/2$, which is a non-intuitive result, given the inhomogeneity of the Hamiltonian and it does not hold for excited states.

Let us describe the family of local Hamiltonians whose GS approaches asymptotically the concentric singlet phase (CSP), also known as rainbow state, and give some heuristic arguments to explain the volume law for the scaling of its entanglement entropy. Consider the set the hopping amplitudes $t_j$ to be parametrized as (cf. figure 4.1 for an illustration)

$$\begin{cases} t_0(\alpha) = 1, \\ t_j(\alpha) = \alpha^{2j}, \quad j = \frac{1}{2}, \dots, L - \frac{3}{2}, \end{cases} \tag{4.2}$$

where, to simplify, we have chosen to label the sites of the chain using half-odd integers, $i = \pm\frac{1}{2}, \pm\frac{3}{2}, \cdots, \pm\left(L - \frac{1}{2}\right)$, in terms of which, the hopping Hamiltonian is given by

$$H \equiv -\frac{t_0}{2} c_{\frac{1}{2}}^\dagger c_{-\frac{1}{2}} - \sum_{i=\frac{1}{2}}^{L-\frac{3}{2}} \frac{t_i}{2} \left[ c_i^\dagger c_{i+1} + c_{-i}^\dagger c_{-(i+1)} \right] + \text{h.c.} \tag{4.3}$$

Via the Jordan-Wigner transformation described in section 2.4, the Hamiltonian (4.3) is equivalent to the XX model for a spin-1/2 chain. For $\alpha = 1$ we recover the well known uniform 1D spinless fermion model with OBC.

In the limit $\alpha \to 0^+$ we obtain the Hamiltonian studied by Vitagliano *et al.* (2010) to illustrate a violation of the area law for local Hamiltonians. Taking $\alpha > 1$ and truncating the chain to the sites $i > 0$, one obtains the Hamiltonian considered by Okunishi and Nishino (2010), which has the scale-free structure of Wilson's approach to the Kondo impurity problem. Furthermore, models where $t_i$ is a hyperbolic function of the site index $i$ were considered in order to measure the energy gap (Ueda *et al.*, 2010).

It is worth to notice the striking similarity between our system and the Kondo chain (Wilson, 1975). Indeed, let us divide our inhomogeneous chain into three parts: central link, left sites and right sites. The left and right sites correspond, in our analogy, to the spin up and down chains used in Wilson's chain representation of the Kondo problem. In both cases, they form a system of free fermions, with exponentially decaying couplings. In the Kondo chain, notwithstanding, the central link becomes a magnetic impurity, which renders the full system non-gaussian.

### 4.2.1 Analysis in the Strong Inhomogeneity Limit

For $\alpha \ll 1$, the couplings become strongly inhomogeneous and, as we discussed in section 2.7, we can apply the strong disorder renormalization group (SDRG) method to find the GS of the system. In our setup, the largest hopping is the central one, $t_0 = 1$, and gets renormalized to $t_0^{(R)} = -\alpha^2$, whose absolute value is larger than $\alpha^3$, which comes next. The engineered parametrization for $t_i$ is such that this situation repeats itself for all RG steps, so the bonds are established in a concentric way around the center, joining sites $+k$ and $-k$, and giving rise to the aforementioned CSP, whose shape looks like a *rainbow* as in figure 4.1. Moreover, notice that the signs alternate. It is easy to see that after the first RG state one can factor out an overall constant $\alpha^2$ in the couplings $t_i$, such that the renormalized Hamiltonian becomes $\alpha^2 H_{L-1} + \text{const}$. In fact, this implies that the rainbow state is a trivial fixed point of the RG with zero correlation length between nearest neighbor sites, except the sites $i = \pm 1/2$.

The SDRG candidate for the GS of the system is a tensor product of bonds on the corresponding sites. Indeed, it can be written as a Fermi state:

$$|GS\rangle = \prod_{k=1}^{L/2} d_k^\dagger |0\rangle, \tag{4.4}$$

where $|0\rangle$ is the Fock vacuum and $d_k^\dagger$ creates either a bond or an anti-bond on a pair of sites, i.e.: $d_k^\dagger \propto c_i^\dagger \pm c_j^\dagger$. The energy gap can be estimated as the effective energy of the

last bond established, which scales as $\alpha^{2L}$ and for $\alpha < 1$ vanishes in the limit $L \to \infty$.

In the $\alpha \to 0^+$ limit of the Hamiltonian (4.3), leading to the rainbow state, is singular: the Hamiltonian decouples in that limit and only the central link survives. Let us consider a very small but non-zero $\alpha$, and study the GS to first order in perturbation theory. The Hamiltonian is always free, so the GS is a Slater determinant given by equation (4.4). The orbital operators, $d_k^\dagger$, can be expanded in terms of the local creation operators:

$$d_k^\dagger = \sum_i \psi_i^k c_i^\dagger, \tag{4.5}$$

where $\psi_i^k$ are the wavefunction components for the single-body associated problem, i.e. eigenvectors of the hopping matrix. It is straightforward to check that $\psi_i^k$ of the form

$$\begin{array}{cccccccccc} & & \cdots & -\frac{5}{2} & -\frac{3}{2} & -\frac{1}{2} & +\frac{1}{2} & +\frac{3}{2} & +\frac{5}{2} & \cdots \\ \psi^1 & = & \cdots & \cdots & \alpha & 1 & 1 & \alpha & \cdots & \cdots \\ \psi^2 & = & \cdots & \alpha & 1 & \alpha & -\alpha & -1 & -\alpha & \cdots \\ \psi^3 & = & \alpha & 1 & \alpha & 0 & 0 & \alpha & 1 & \alpha \end{array} \tag{4.6}$$

are eigenstates of the hopping matrix.

Notice the sign alternation, due to the negative sign in the renormalization prescription (cf. equation (2.30) in section 2.7). It is straightforward to check that all those $\psi^k$ are eigenstates of the hopping matrix to first order in $\alpha$. We can now define two families of states: the bonding and the anti-bonding creating operators, defined as:

$$\left(b_{ij}^+\right)^\dagger = \frac{1}{\sqrt{2}}\left(c_i^\dagger + c_j^\dagger\right), \tag{4.7a}$$

$$\left(b_{ij}^-\right)^\dagger = \frac{1}{\sqrt{2}}\left(c_i^\dagger - c_j^\dagger\right). \tag{4.7b}$$

Thus, in the limit $\alpha \to 0^+$, the GS of the Hamiltonian (4.3) can be written as the concentric singlet state or rainbow state:

$$|R_L\rangle \equiv \left(b^{s_L}_{-L+\frac{1}{2},L-\frac{1}{2}}\right)^\dagger \cdots \left(b^+_{-\frac{5}{2},\frac{5}{2}}\right)^\dagger \left(b^-_{-\frac{3}{2},\frac{3}{2}}\right)^\dagger \left(b^+_{-\frac{1}{2},\frac{1}{2}}\right)^\dagger |0\rangle. \tag{4.8}$$

where $s_L = (-1)^L$ accounts for the proper selection of either a singlet-type bond or a triplet-type bond.

As discussed in section 2.7, the entanglement entropy of any block $B$ is obtained by counting the number of bonds which connects $B$ with the rest of the system. Moreover, within the SDRG method, both the von Neumann and the Rényi entanglement entropies have the same value. Thus, let $B$ be the block containing half of the chain, $L$. Its entanglement entropy is straightforward to compute: $L \cdot \log 2$; i.e. the state is maximally entangled and fulfills a volume law.

The validity of the renormalization scheme improves when the renormalized link is much stronger than the surrounding ones, that is $\alpha \ll 1$. Thus, one can assert that the rainbow state becomes the exact GS of the $H_L$ Hamiltonian in the limit $\alpha \to 0^+$.

### 4.2.2 Analysis in the Weak Inhomogeneity Limit: Continuum Approximation

As described above, the SDRG method provides a valence bond picture of the GS in the strong inhomogeneity limit, which explains in simple terms the volume law. On the other hand, the exact diagonalization method described in section 2.2 is applicable to all values of $\alpha$ and in particular to the weak inhomogeneity limit, i.e. $\alpha \to 1^-$, where one recovers the uniform model, with a logarithmic law described by the CFT. We shall show that the two limits are connected continuously, that is, with no phase transitions between them. This fact offers the possibility of studying the crossover between the log law and the volume law of the entanglement entropies, which exhibits interesting features.

The Hamiltonian (4.1) is quadratic in the fermionic operators. Therefore its spectrum can be obtained by diagonalizing the $2L \times 2L$ hopping matrix which is built

$$t_{ij} = -t_0\, \delta_{ij,-\frac{1}{2}} - t_i \delta_{|i-j|,1}, \quad i,j = \pm\frac{1}{2}, \cdots, \pm\left(L - \frac{1}{2}\right),$$

in terms of eigenmodes $\phi_i^k$ which fulfill $t_{ij}\phi_j^k = E_k \phi_i^k$. If $\phi_i^k$ is an eigenfunction with energy $E_k$, then $(-1)^i \text{sign}(i)\, \phi_i^k$ is another eigenfunction with energy $-E_k$, due to chiral symmetry. Thus, the GS of the system is obtained by filling the lowest energy levels with $L$ fermions, i.e. at half-filling ratio. The GS of the system is given by

$$|R(\alpha)\rangle = \prod_{k=1}^{L} d_k^\dagger(\alpha)|0\rangle, \tag{4.9}$$

where $d_k^\dagger = \sum_i \phi_i^k c_i^\dagger$.

#### Continuum approximation

A first study of the properties of this system was presented by Ramírez *et al.* (2014b) based on numerical analysis of the rainbow state given in equation (4.9). Moreover, the study of the system in the weak inhomogeneity limit motivated the derivation of a continuum approximation of the Hamiltonian (4.3) (Ramírez *et al.*, 2015). This is obtained by expanding the local operator in the $n$-th site, $c_n$ into the slow modes, $\psi_R(x)$ and $\psi_L(x)$ around the Fermi points $\pm k_F$

$$\frac{c_n}{\sqrt{a}} \simeq e^{ik_F x}\psi_L(x) + e^{-ik_F x}\psi_R(x), \tag{4.10}$$

located at the position $x = an \in (-\mathcal{L}, \mathcal{L})$, where $a$ is the lattice spacing and $\mathcal{L} = aL$. In the continuum limit, $a \to 0$ and $L \to \infty$, with $\mathcal{L}$ kept constant. At half-filling, $k_F = \pi/(2a)$ is the Fermi momentum. The equation (4.10) is the familiar expansion used in the uniform case, $\alpha = 1$, that we used to derive the numerical results that presented previously. Plugging equation (4.10) into Hamiltonian (4.3) one obtains

$$H \simeq \frac{ia}{2} \int_{-\mathcal{L}}^{\mathcal{L}} dx\, e^{-\frac{h|x|}{a}} \left[ \psi_R^\dagger \partial_x \psi_R - \left( \partial_x \psi_R^\dagger \right) \psi_R - \psi_L^\dagger \partial_x \psi_L + \left( \partial_x \psi_L^\dagger \right) \psi_L \right], \tag{4.11}$$

where

$$h \equiv -2 \log(\alpha). \tag{4.12}$$

To derive Hamiltonian (4.11), we have assumed that the fields $\psi_{R,L}(x)$ vary slowly with $x$, so that cross terms like $(-1)^{x/a} \psi_R^\dagger(x) \psi_L(x)$ can be dropped. We have also made a gradient expansion $\psi(x + a) \simeq \psi(x) + a \partial_x \psi(x)$, keeping only terms up to the first derivative. The Hamiltonian (4.11) describes the low energy excitations of the original lattice Hamiltonian at half-filling. It is worth to mention that the Hamiltonian (4.11) is a hermitian operator, i.e. $H^\dagger = H$, which is of course a consequence of the hermiticity of the Hamiltonian (4.3). In the continuum limit we shall take $h \to 0$, with $h/a$ kept constant, so that $\alpha \to 1^-$.

The boundary conditions satisfied by the fields $\psi_{L,R}(x)$ at $x = \pm\mathcal{L}$, can be derived from equation (4.10) setting $c_{\pm(L+\frac{1}{2})} = 0$ and taking a continuum limit that yields

$$\psi_R(\pm\mathcal{L}) = \mp i\, \psi_L(\pm\mathcal{L}). \tag{4.13}$$

Then, integrating by parts, one can write Hamiltonian (4.11) as

$$H \simeq ia \int_{-\mathcal{L}}^{\mathcal{L}} dx\, e^{-\frac{h|x|}{a}} \left[ \psi_R^\dagger \partial_x \psi_R - \psi_L^\dagger \partial_x \psi_L - \frac{h}{2a} \mathrm{sign}(x) \left( \psi_R^\dagger \psi_R - \psi_L^\dagger \psi_L \right) \right]. \tag{4.14}$$

The Fermi velocity is then given by $v_F = a$, that we set equal to one by convention (similarly, we replace $h/a \to h$). The single-body spectrum of the uniform model, that is, $h = 0$, can be easily found

$$E_m = \frac{\pi(m + 1/2)}{2L}, \quad m = 0, \pm 1, \ldots \tag{4.15}$$

For the non-uniform model we have the equations

$$i e^{-h|x|} \left[ \partial_x \mp \frac{h}{2} \mathrm{sign}(x) \right] \psi_{R,L}(x) \quad = \quad \pm E \psi_{R,L}(x), \tag{4.16}$$

whose solution is

$$\psi_{R,L}(x) = A_{R,L} e^{h|x|/2} \exp\left[\mp \frac{iE}{h} \text{sign}(x) \left(e^{h|x|} - 1\right)\right]. \tag{4.17}$$

Notice that, in the limit $h \to 0$, one recovers the usual plane-wave solutions $\psi_{R,L} \to A_{R,L} e^{\mp iEx}$. The boundary conditions given by equation (4.13) imply:

$$A_R \exp\left[-\frac{iE}{h}\left(e^{hL} - 1\right)\right] = -\, i\, A_L \exp\left[\frac{iE}{h}\left(e^{hL} - 1\right)\right], \tag{4.18a}$$

$$A_R \exp\left[\frac{iE}{h}\left(e^{hL} - 1\right)\right] = \quad i\, A_L \exp\left[-\frac{iE}{h}\left(e^{hL} - 1\right)\right]. \tag{4.18b}$$

which, eliminating $A_{R,L}$, yields

$$\exp\left[\frac{4iE}{h}\left(e^{hL} - 1\right)\right] = -1. \tag{4.19}$$

The eigenmodes are then given by

$$E_m = \frac{h\pi(m + 1/2)}{2(e^{hL} - 1)} = a(z)\frac{\pi(m + 1/2)}{2L}, \quad m = 0, \pm 1, \cdots \tag{4.20}$$

where $a(z)$, defined as

$$a(z) = \frac{z}{e^z - 1}, \tag{4.21}$$

and

$$z \equiv -2L \log \alpha, \tag{4.22}$$

that can be endowed with a physical interpretation as the the decay length of the hopping amplitudes. We shall see below that $z$ also plays the role of a scaling parameter. Equation (4.21) was interpreted providing an expression for the Fermi velocity (Ramírez *et al.*, 2014b). Notice that $z$ has a finite value in the continuum limit since it can be written as $z = (h/a)\mathcal{L}$. The left panel in figure 4.2 shows the numerical data for the single-particle spectrum of the Hamiltonian (4.3) which corresponds to equation (4.20) with the function $a(z)$ given numerically in the right panel in figure 4.2. As we can see, the analytic expression given by equation (4.21) gives a very good fit of the numerical data.

To find the eigenfunctions with energy $E_m$, we first compute the constants $A_{R,L}$ using the relation given by equations (4.18)

$$A_{R,L} = \exp\left\{\pm i\left[\frac{E_m}{h}\left(e^{hL} - 1\right) - \frac{\pi}{4}\right]\right\}, \tag{4.23}$$

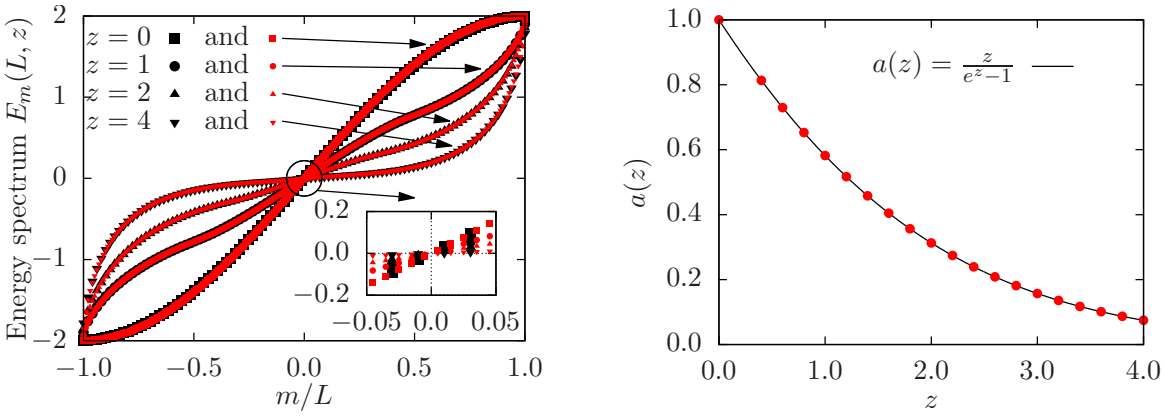


Figure 4.2: Left: Energy spectrum $E_m(L,z)$ for a system of $L=50$ (red marks) and $L=100$ (black marks) for several values of $z$. The numerical data collapse on the same curve, which shows a scaling law as predicted by equation (4.20). Right: The scaling function $a(z)$ that gives the spectrum of the Hamiltonian (4.3) near the Fermi energy. The points are the numerical data, i.e., the slope of the spectrum at the Fermi point, and the continuous line is the analytic result.

and equation (4.10), obtaining

$$\psi_n^{(m)} \simeq e^{h|n|/2} \cos\left[\frac{\pi(n-m)}{2} + \mathrm{sign}(n)\,\frac{\pi(m+1/2)}{2}\,\frac{e^{h|n|}-1}{e^{hL}-1}\right], \tag{4.24}$$

where $n = \pm\frac{1}{2}, \cdots, \pm\left(L-\frac{1}{2}\right)$ and $m = 0, \pm 1, \cdots$. Figure 4.3 shows the numerical and analytic values of $\psi_n^{(m)}$ for $m = 0, 1$ and $z = 1$ and 2. As $hn = zn/L$, we see that for the same value of $z$, all the curves collapse when expressed in the scaled variable $n/L$.

The results obtained so far suggest that the continuum Hamiltonian (4.14) can be brought to the standard canonical form of a free fermion with OBC. To show that this is indeed the case, let us make the change of variables

$$\tilde{x} = \mathrm{sign}(x)\,\frac{e^{h|x|}-1}{h}, \tag{4.25}$$

that maps the interval $x \in [-L, L]$ into the interval $\tilde{x} \in [-\tilde{L}, \tilde{L}]$ where

$$\tilde{L} = \frac{e^{hL}-1}{h}. \tag{4.26}$$

The fermion fields in the variable $\tilde{x}$ are given by

$$\tilde{\psi}_{R,L}(\tilde{x}) = \left(\frac{d\tilde{x}}{dx}\right)^{-1/2} \psi_{R,L}(x) = e^{-h|x|/2}\psi_{R,L}(x), \tag{4.27}$$

that plugged into Hamiltonian (4.14) gives (recall that we set $a = 1$, so $\mathcal{L} = L$)

$$H \simeq i\int_{-\tilde{L}}^{\tilde{L}} d\tilde{x}\,\left[\tilde{\psi}_R^\dagger \partial_{\tilde{x}}\tilde{\psi}_R - \tilde{\psi}_L^\dagger \partial_{\tilde{x}}\tilde{\psi}_L\right]. \tag{4.28}$$

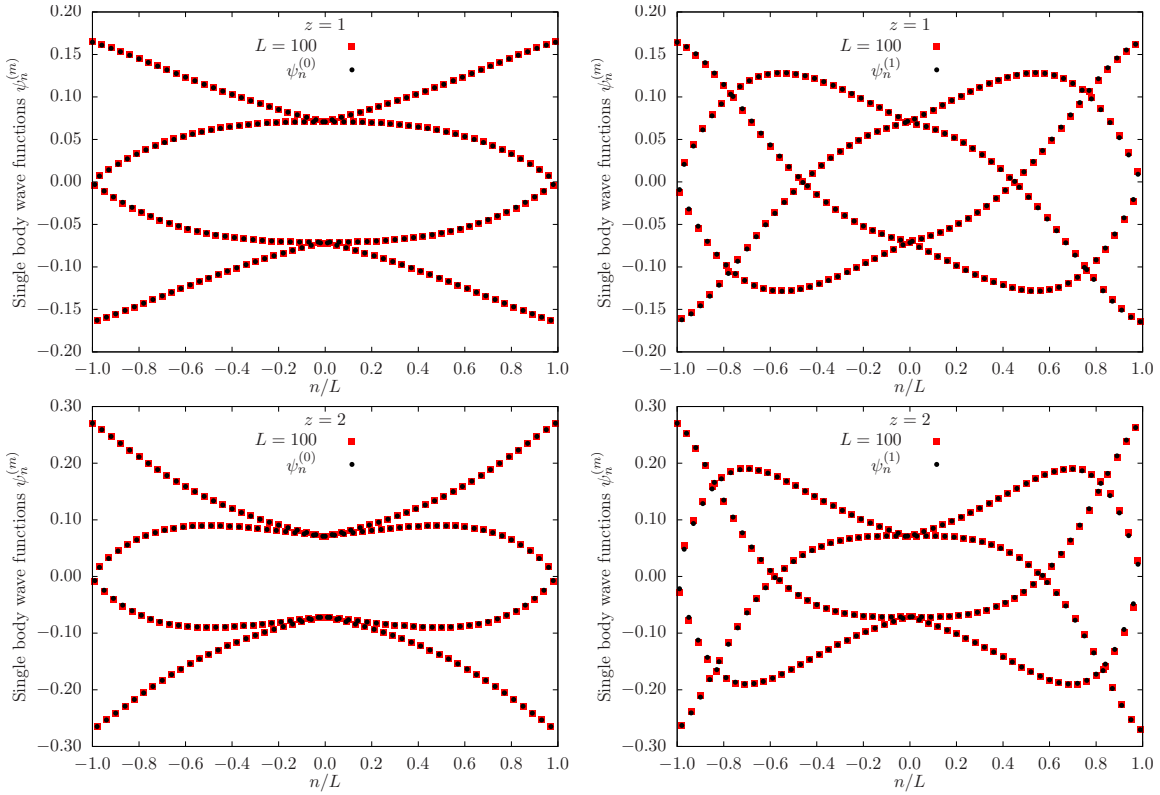


Figure 4.3: Wavefunctions just below the Fermi level ($m = 0$, left column) and the next below the Fermi level ($m = 1$, right column) for $z = 1$ (top) and 2 (bottom). The analytic values of $\psi_n^{(m)}$ are given by equation (4.24).

That is just the free fermion Hamiltonian for a chain of length $2\tilde{L}$. This result suggests that one could try to derive some of the properties of the rainbow Hamiltonian (4.3), from those of the free fermion system. This will be done in the next section when discussing the entanglement properties of the GS.

Notice that equation (4.25) is not analytic at $x = 0$, but if we take $x > 0$ we obtain

$$\tilde{x} = \frac{e^{hx} - 1}{h}, \tag{4.29}$$

which is a conformal transformation (similarly, $\tilde{x} = -(e^{-hx} - 1)/h$ if $x < 0$). If we add the euclidean time coordinate, that is, $x \to x + i\tau$, the transformation given by equation (4.29) becomes periodic in $\tau$ with a period equal to $\beta = 2\pi/h$. This result leads us to associate to the system an effective temperature

$$T = \frac{h}{2\pi}. \tag{4.30}$$

This result will be interpreted below using arguments based on the scaling of the entanglement entropy.

**Validity of the continuum approximation**

As it can be seen above, in the results for the Fermi velocity (cf. figure 4.2) and for the wavefunctions (cf. figure 4.3), the continuum approximation provides very accurate predictions regarding the wavefunctions near the Fermi point and the Fermi velocity. Indeed, that is the expected range of validity of any continuum limit: the long-distance physics which takes place near the Fermi point.

We have explored the limits of the validity of the continuum approximation. Figure 4.4 shows the overlap between the predicted and the numerical single-particle wavefunctions as we go deeper beneath the Fermi surface. The horizontal axis shows the re-scaled wavefunction index $m/L$, which is 0 for the Fermi level and 1 for the deepest one. The vertical axis corresponds to the overlap between the continuum approximation and the actual wavefunction, defined as

$$\mathcal{O} = |\langle \psi_{cont} | \psi_{exact} \rangle|. \tag{4.31}$$

The numerical experiments were performed for $L$ in the range of 50 to 500 and $z = 1$. Notice that for small wavefunction index $m/L$, the overlap is virtually one, but it decreases very fast behind a certain critical value. The explanation is that single-body wavefunctions which are deep below the Fermi energy vary over very small length scales, rendering the continuum approximation inaccurate.

Even if the wavefunctions are not correctly predicted in a one-to-one basis, the complete Slater determinant composing the states can be similar. This possibility is checked in the top-right panel of figure 4.4, where we plot the overlap between the full Slater determinant states (continuum limit and numerical computation) as a function of $z$ for different values of the system size $L$. We can see that below a certain critical $z$, the overlap stays close to one, and then it decreases to zero.

The bottom panel of figure 4.4 shows the region of validity of the continuum approximation in the $(L, z)$ plane, by depicting two lines which mark the level 0.95 and the level 0.9 for the overlap between the numerical GS of the Hamiltonian and the continuum approximation obtained by the deformed uniform wavefunctions.

## 4.3 Entanglement over the Rainbow

The entanglement properties of the rainbow state (cf. equation (4.9)) can be found using the method of exact diagonalization described in section 2.2 which allows us to find the set of eigenvalues $\{\nu_p\}_{p=1}^{\ell}$ of the correlation matrix restricted to the block. The set $\{\nu_p\}$ allows a full computation of the entanglement spectrum, i.e. the spectrum of the reduced density matrix $\rho_B$, which provides the most complete information about entanglement and can help characterize quantum phase transitions (Li and Haldane,

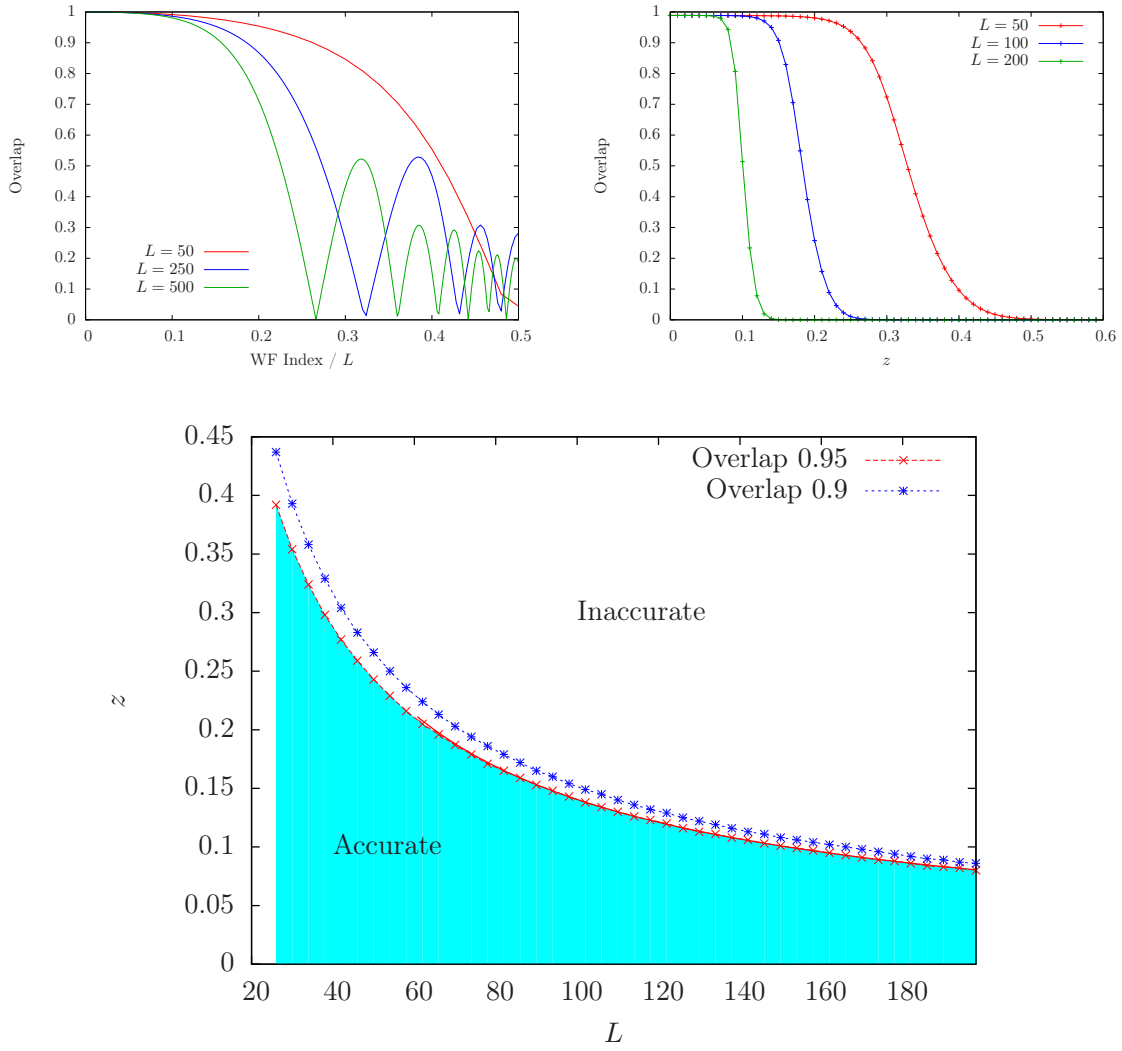


Figure 4.4: Top left: overlap between continuum approximation and numerical single-particle wavefunctions, in a one-to-one basis, for $z = 1$. Top right: overlap between continuum and numerical many-body states, as a function of $z$, for different values of $L$. Bottom: validity region for the continuum approximation, showing the lines of 90% and 95% overlap between the continuum and the exact wavefunctions.

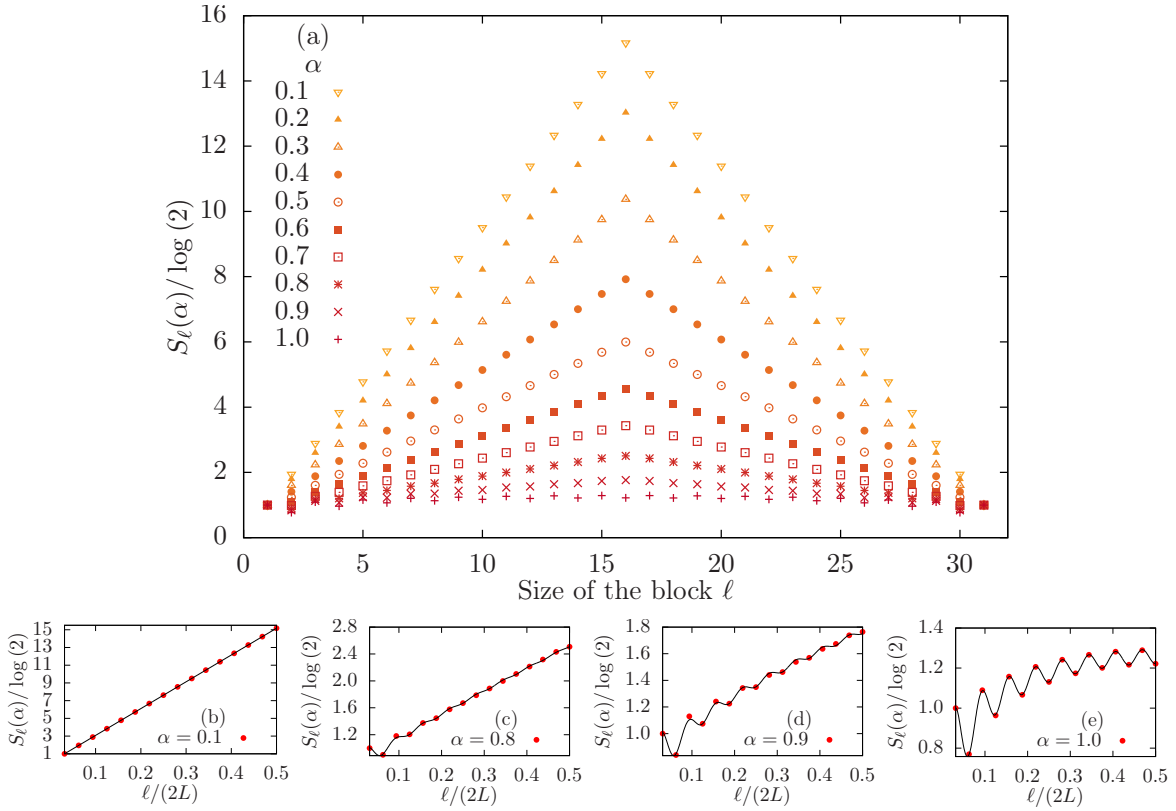


Figure 4.5: (a) Block entropy $S_\ell(\alpha)$, for a system of size $L = 16$ (32 sites). Notice the *tent shape* for small $\alpha$, denoting volumetric growth of the entanglement entropy. (b) For $\alpha = 0.1$; (c) for $\alpha = 0.8$; (d) for $\alpha = 0.9$ and (e) for the uniform case $\alpha = 1$.

2008).

We should remark that the numerical computation of the eigenstates of matrix $t_{ij}$ is an ill-conditioned problem if $z$ is large. Working at double precision the upper bound for $z$ can be estimated as $e^{-z_{\max}} \sim 10^{-16}$, that is $z_{\max} \sim 36$, but we shall be usually working below this value.

### 4.3.1 Von Neumann Entropy

Let us consider the entanglement of a block $B$ formed by the $\ell$ leftmost sites with the rest of the system. Let $S_\ell(\alpha)$ denote the von Neumann entropy of the block $B$. The panel (a) in figure 4.5 shows its dependence with $\ell$ for different values of $\alpha$ in a system with 32 sites, i.e. $L = 16$. For low values of $\alpha$ we observe a characteristic *tent shape*, i.e. an approximately linear growth up to $\ell = L$ (cf. panel (b) in figure 4.5) followed by a symmetric linear decrease, giving the volumetric behavior. As the value of $\alpha$ grows, the slope decreases (cf. panel (c) in figure 4.5) and ripples start to appear (cf. panel (d) in figure 4.5) and for $\alpha = 1$ they recover the parity oscillations (cf. panel (e) in figure 4.5) of the von Neumann entropy with OBC described in section 2.6.

To simplify the analysis we shall consider the von Neumann entropy of the half-chain, $S_L(\alpha)$. Figure 4.6(a) shows the values of $S_L$ for systems of with $L = 50, \ldots, 100$ and

fixed values of $z = 0, \ldots, 4$ (note that $\alpha$ is tuned with $L$ in order to keep $z$ constant). Quite remarkably the half-chain entropy can be fitted to an expression similar to equation (2.21) (cf. section 2.6) just giving to the parameters $c$, $d$ and $f$ a dependence on $z$

$$S_L = \frac{c(z)}{6} \log L + d(z) + f(z) \cos(\pi L) L^{-K}, \tag{4.32}$$

where the functions $c(z)$, $d(z)$ and $f(z)$ are shown in figures 4.6(b)-(d) respectively, together with the corresponding fits, which will be analyzed together with the fits for the Rényi entropies in section 4.3.2. The Luttinger parameter $K$ in equation (4.32) is taken equal to 1, which gives the best fit to the numerical data. Equation (4.32) is motivated by the standard CFT formulas recovered in the case $z = 0$, which corresponds to a conformal theory with central charge $c = 1$ and Luttinger parameter $K = 1$ (cf. section 2.6).

Indeed, in the limit $z \to 0$, we obtain $c(z) \to 0.995$. As $z$ increases, the function $c(z)$ decreases. This result reminds us of the Zamolodchikov $c-$theorem, according to which a certain function $C$ of the coupling constants of a relativistic $1 + 1$ quantum field theory, never increases along the RG flow and equals the central charge of the CFT at the fixed points (Zamolodchikov, 1986; Cardy, 1996). In our case, there is a fixed point at $z = 0$, which corresponds to a free fermion with OBC which has $c = 1$. One should expect that, along the RG flow, the value of $z$ increases while $c(z)$ decreases, approaching zero in the limit $z \to \infty$, where one finds the rainbow state which, as we discuss in 4.2.1, is a trivial fixed point of the RG.

Let us analyze the term $d(z)$ in equation (4.32) which gives rise to the volumetric term in the entanglement, as we will see. Indeed, $d(z) \propto z$ based on the corrections to the scaling of entanglement discussed in section 2.6. The linear increase of $d(z)$ is responsible for the extensive behavior of the entanglement entropy which was discussed in terms of the SDRG applied in the strong inhomogeneity limit in section 4.2.1. In a CFT on a strip of length $2L$, the entanglement entropy of the half line is given by

$$S_L = \frac{c}{6} \log(2L/\pi) + s_1' + 2g + f \cos(\pi L) L^{-K}, \tag{4.33}$$

where the term $\tilde{c}_1'$ (cf. equation (2.21) in section 2.6) is separated into a non-universal constant $s_1'$ and the term $g$ which accounts the boundary entropy of Affleck and Ludwig (1991); Laflorencie *et al.* (2006). We may then interpret $d(z)$ as a $z$ dependent boundary entropy $g(z)$, up to some non universal constants. As the $c$-theorem, there is a $g-$theorem asserts that the $g$ function decreases under the RG flow of the boundary, so long as the bulk theory remains critical during the boundary flow (Affleck and Ludwig, 1993; Friedan and Konechny, 2004). However, there are no reasons for this behavior if the bulk theory also flows with the RG (Green *et al.*, 2008). This is the situation found

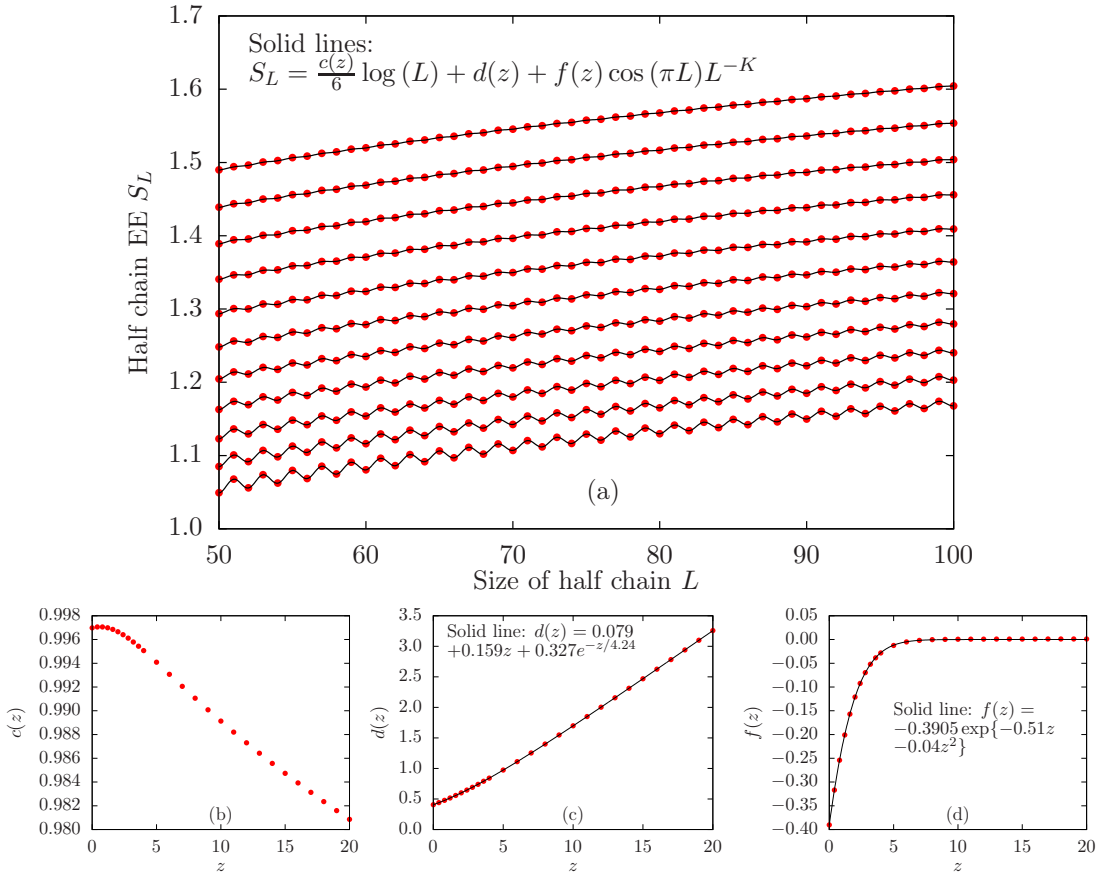


Figure 4.6: (a) Half-chain entanglement entropy $S_L$ as a function of the system half size $L = 50, \ldots, 100$ for $z = 0$ to 4 in steps of 0.4 from bottom to top. Solid lines are fits to equation (4.32) with $\chi^2 \sim 10^{-10}$. The data corresponding to the values $4 < z \leq 20$, not shown in this figure, also satisfy equation (4.32). (b)-(d) Functions $c(z)$, $d(z)$ and $f(z)$, in the interval $z \in [0, 20]$, together with fits for $d(z)$ and $f(z)$.

here, where $d(z)$ increases with $z$, as shown in panel (c) of figure 4.6.

The last term in equation (4.32) describes the parity oscillations of $S_L$, which are clearly visible in panel (a) of figure 4.6 for $z \leq 2$, i.e. the weak inhomogeneity limit. This behavior is characterized by the function $f(z)$, which vanishes for $z \simeq 4$ as shown in panel (d) of figure 4.6. We can use equation (4.32) to study the limit $L \gg 1$ with $\alpha$ kept constant, which implies $z \gg 1$. From panels (b)-(d) in figure 4.6 one finds that $c(z) \to 0$, $d(z) \to 0.318z$ and $f(z) \to 0$ so that

$$S_L \to -0.318 L \log \alpha, \qquad L \gg 1. \tag{4.34}$$

This result cannot be valid for very small $\alpha$ since we know that for the strong inhomogeneity limit, i.e. $\alpha \to 0^+$, the entropy is given by $S_L = L \log 2$. The crossover takes place for $\alpha \sim 1/8$.

These numerical data can be fitted to an expression that contains linear, oscillating and logarithmic terms of $\ell$ with coefficients that depend in a non trivial manner in $\alpha$ and $L$.

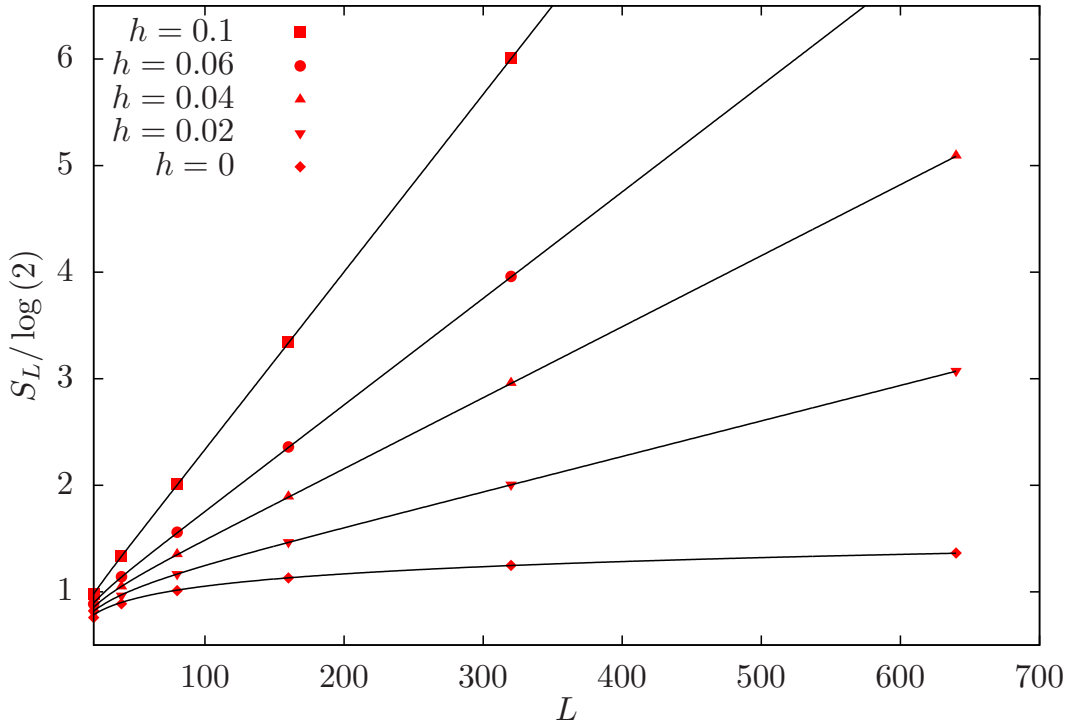


Figure 4.7: Comparing the half-chain entropy for different $L$ and $h$ with the theoretical prediction, equation (4.36).

### Entanglement in the continuum approximation

With the corrections to the scaling of the entanglement discussed in 2.6, we find the von Neumann entropy of the left half of a critical system with OBC is given by

$$S_{CFT}(L) = \frac{c}{6}\log(L) + \tilde{c}'. \tag{4.35}$$

where $c = 1$ for the free fermionic system under study, i.e. for $\alpha = 1$. Taking in combination equations (4.26) and (4.35), we can provide a prediction for the entropy of the half-chain in the deformed GS of the Hamiltonian (4.3). Indeed, substituting $L$ by $\tilde{L}$ (cf. equation (4.26)), we obtain

$$S_{CSP}(L) = \frac{c}{6}\log\left(\frac{e^{hL}-1}{h}\right) + \tilde{c}', \tag{4.36}$$

which is checked in figure 4.7 for low values of $h$, although its validity ranges far beyond that regime close to the conformal point.

Expression given by equation (4.36) can be expanded in the limit when $hL$ is large enough, using the definition for $h$ in equation (4.12), as

$$S_{CSP}(L) \approx \frac{c}{6}hL \approx -\frac{1}{3}L\log\alpha, \tag{4.37}$$

which is in agreement with numerical estimation in equation (4.34),

$$S_L \approx -0.318\ L\ \log(\alpha). \tag{4.38}$$

Notice also that in the limit $h \to 0^+$, i.e. the weak inhomogeneity limit, equation (4.36) becomes equation (4.35).

It is worth to compare equation (4.36) with the entropy of a thermal state at inverse temperature $\beta = 1/T$ in a CFT (Calabrese and Cardy, 2004)

$$S_{CFT}(L) \approx \frac{c}{3} \log\left[\frac{\beta}{\pi} \sinh\left(\frac{\pi L}{\beta}\right)\right] \approx \frac{\pi c L}{3\beta}, \tag{4.39}$$

where we have taken the limit $L \gg \beta$, which leads to an extensive entropy. Comparing equation (4.39) and equation (4.37) we obtain that

$$T = \frac{1}{\beta} = \frac{h}{2\pi}, \tag{4.40}$$

in agreement with equation (4.30), which was based on the analytic extension of the transformation employed to derive the continuum limit, equation (4.25). Thus, we can assert that the rainbow state has an entropy similar to that of a thermal state with temperature given by equation (4.40). We shall verify this result later on in the study of the entanglement spectrum of the system.

### 4.3.2 Rényi Entropies

Let us consider the scaling behaviour of the Rényi entropies described in section 2.6.[1] Thus, let $S_L^{(n)}$ be the $n$-order Rényi entanglement entropy at half-chain for the GS of the free fermion model given by (cf. equation (2.25) in section 2.6)

$$S_L^{(n)} \simeq \frac{1}{12}\left(1 + \frac{1}{n}\right) \log\left(\frac{4L}{\pi}\right) + c_n' + f_n \cos(\pi L) \left(\frac{8L}{\pi}\right)^{-1/n}. \tag{4.41}$$

Moving into the rainbow phase, we can give a first estimate of the Rényi entropies using the SDRG method discussed in section 2.7. According to it, all the $n$-order Rényi entropies are equal among themselves, and equal to the von Neumann entropy (Ramírez *et al.*, 2014a). This approximation becomes exact only in the strong inhomogeneity limit, i.e. $\alpha \to 0^+$. Otherwise, we should make use of the exact diagonalization method discussed in section 2.5.

The numerical computations performed can be compared to a natural extension of

[1] Note the change in the notation to keep $\alpha$ for the deformation parameter

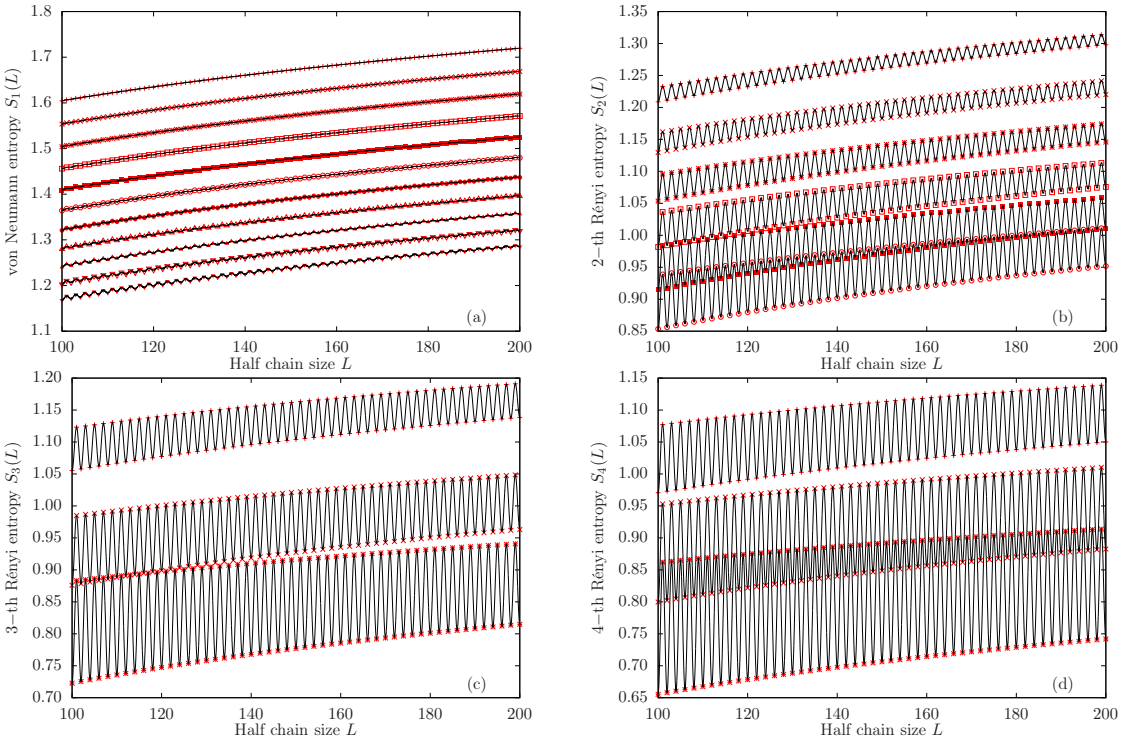


Figure 4.8: Rényi entanglement entropy $S^{(n)}(L)$ of the left half-chain for different values of $z$. Top-left panel $n = 1$ (von Neumann) for $z = \{0, 0.4, 0.8, \ldots, 4\}$ (bottom to top). Top-right panel $n = 2$ for $z = \{0, 0.8, 1.6, \ldots, 4\}$. Bottom panels $n = 3$ (left) and $n = 4$ (right) for $z = \{0, 1, 2\}$. All data show fits to expression given by equation (4.42).

the expression given in equation (4.41):

$$S_L^{(n)}(z) = \frac{c_n(z)}{12}\left(1 + \frac{1}{n}\right)\log\left(\frac{4L}{\pi}\right) + d_n(z) + f_n(z)(-1)^L\left(\frac{8L}{\pi}\right)^{-K/n}. \qquad (4.42)$$

This Ansatz for the Rényi entropies (Ramírez *et al.*, 2015) is a generalization of the Ansatz (Ramírez *et al.*, 2014b) for the von Neumann entropy of the half-chain $S_L^{(1)}(z)$. The comparison is performed in figure 4.8, which shows the Rényi entropies for the half chain for different values of $z$ in each panel, fitting the parameters $c_n(z)$, $d_n(z)$ and $f_n(z)$. The Luttinger constant is kept as $K = 1$. Oscillations in all cases decrease as $z$ increases, but they always increase with the Rényi order $n$.

The functions $c_n(z)$, $d_n(z)$ and $f_n(z)$, are shown in figure 4.9. Their expressions can be derived in terms of the continuum approximation discussed in section 4.2.2, replacing $L$ by $\tilde{L}$ in equation (4.26), and writing

$$\tilde{L} = \frac{e^z - 1}{z}L, \qquad (4.43)$$

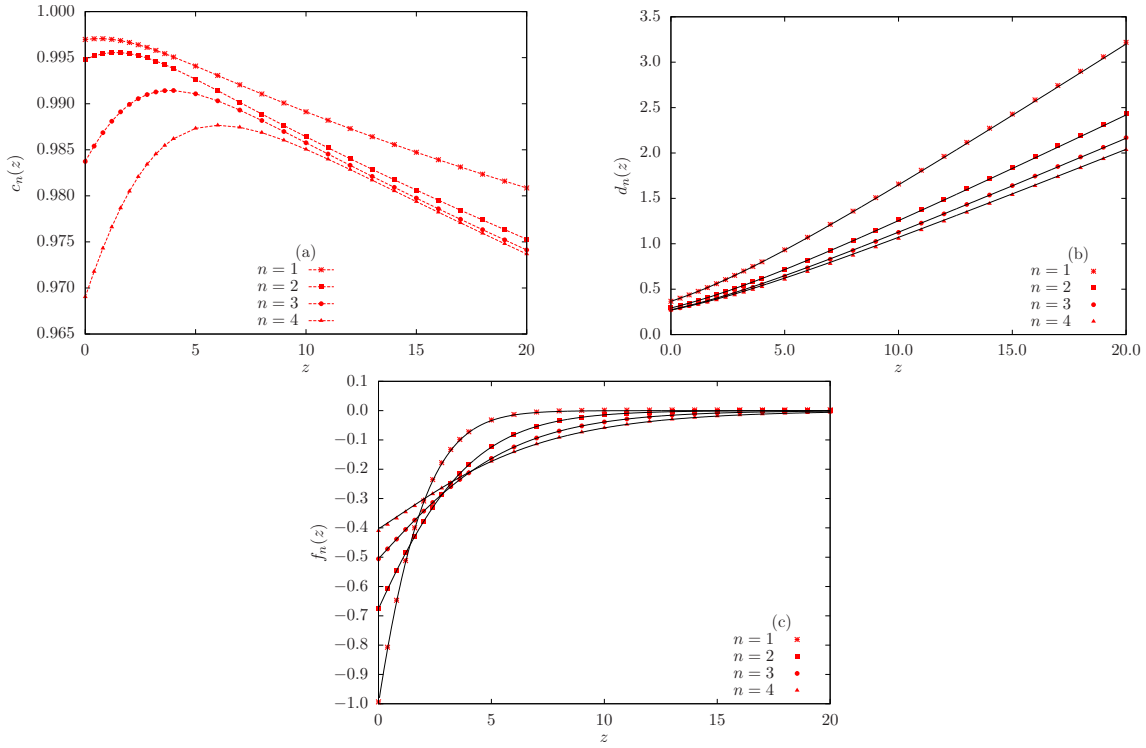


Figure 4.9: Fitting parameters in equation (4.42) as a function of $z$: (a) $c_n(z)$, where the lines are for visual guide only, note the very narrow range of values for $c_n(z)$; (b) $d_n(z)$, where the continuous line is given in equations (4.44) (c) $f_n(z)$, where the continuous line is given in equations (4.44).

which yields

$$c_n(z) = 1, \tag{4.44a}$$

$$d_n(z) = c'_n + \frac{c}{12}\left(1+\frac{1}{n}\right)\log\left(\frac{e^z-1}{z}\right), \tag{4.44b}$$

$$f_n(z) = f_n\left(\frac{e^z-1}{z}\right)^{-1/n}, \tag{4.44c}$$

Figure 4.9 shows the fitting coefficients for the Ansatz of different orders of the Rényi entropy given by equation (4.42), for systems of size $10^2 \leq L \leq 10^3$ and for a range of values $0 \leq z \leq 20$. Panel (a) shows the small variation ($< 4\cdot 10^{-2}$) for $c_n(z)$ in all range of $z$. Panels (b-c) show $d_n(z)$ and $f_n(z)$, solid lines are given by equations (4.44). Notice the perfect agreement between these expressions and the numerical results.

Constants $c'_n$ and $f_n$ defined in equations (4.44) are the only genuinely open parameters in equation (4.42). See in table 4.1 the values for the fitting parameters $c'_n$ and $f_n$. Note the agreement between $f_n$ and the values $f_n^{CFT}$ given by the CFT corrections for the oscillations of the entanglement entropy (cf. equation (2.26)).

| $n$ | $c'_n$ | $f_n$ | $f_n^{CFT}$ | $\chi^2$ |
|---|---|---|---|---|
| 1 | 0.3663 | $-0.9937$ | $-1$ | $9 \cdot 10^{-9}$ |
| 2 | 0.2929 | $-0.6736$ | $-0.67598$ | $2 \cdot 10^{-8}$ |
| 3 | 0.2728 | $-0.5056$ | $-0.50547$ | $6 \cdot 10^{-8}$ |
| 4 | 0.2692 | $-0.4098$ | $-0.40345$ | $3 \cdot 10^{-7}$ |

Table 4.1: Fitting parameters for the expression of the entropy at half chain defined in equation (4.42). The values $f_n^{CFT}$ are obtained from equation (2.26).

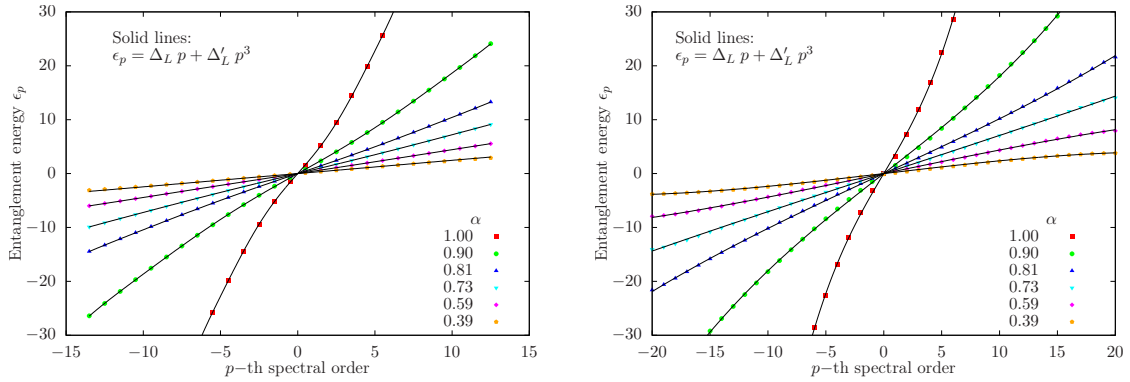


Figure 4.10: Entanglement energies of the half-chain for several values of $\alpha$ and $L = 40$ (left) and $L = 41$ (right) together with a fit to the equation (4.48).

### 4.3.3 Entanglement spectrum and thermo field states

In order to provide a thorough characterization of the entanglement of the half-chain we have analyzed its entanglement spectrum (ES) (Li and Haldane, 2008). The reduced density matrix for a block can always be written as $\rho_B \equiv \exp(-H_E)$, where $H_E$ is called the entanglement Hamiltonian. In the case where the state is a Slater determinant, such as $|R_L(\alpha)\rangle$ (cf. equation (4.9)), $H_E$ can be expressed as a free-fermion Hamiltonian:

$$H_E = \sum_{p=1}^{\ell} \epsilon_p b_p^\dagger b_p + f_0, \tag{4.45}$$

where $\epsilon_p$ are the entanglement energies (EEs), which can be computed from the eigenvalues $\nu_p = \langle b_p^\dagger b_p \rangle$ of the correlation matrix $C_{ij}^B$ obtained by the exact diagonalization method (cf. section 2.2) as

$$\nu_p = \frac{1}{1 + \exp(\epsilon_p)}, \tag{4.46}$$

and the overall constant $f_0$ is given by

$$f_0 = \sum_{p=1}^{\ell} \log(1 + e^{\epsilon_p}). \tag{4.47}$$

Let us consider our block to be the left half-chain. In the limit $\alpha \to 0^+$, we obtain

the rainbow state, which is maximally entangled and the ES is straightforward to describe. Each site makes up a bond with another site outside the block. Thus, each broken bond provides an entanglement mode, $b_p^\dagger$, localized at site $p$, with occupation probability $\nu_p = 1/2$. Applying expression given by equation (4.46), we can see that the entanglement energies are all $\epsilon_p = 0$. In other terms, the entanglement Hamiltonian $H_E = f_0 = L \log 2$ gives the entanglement entropy $S_L = L \log 2$.

Figure 4.10 shows the EE for a chain with $L = 40$ and $L = 41$, for different values of $\alpha$. Note that for $L$ odd there is a zero energy. In agreement with the previous discussion for small $\alpha$, the values of $\epsilon_p$ are located symmetrically around zero. However, as $\alpha$ increases the EE, $\epsilon_p$ increases almost linearly with the eigenvalue index $p$ in the proximity of the zero energy following the law

$$\epsilon_p \approx \Delta_L \, p + \Delta'_L \, p^3, \qquad |p/L| \ll 1, \tag{4.48}$$

where $\Delta'_L \ll \Delta_L$, as shown by Eisler and Peschel (2013). The label $p$ is chosen now as

$$p = \begin{cases} \pm 1/2, \pm 3/2, \cdots, \pm(L-1)/2 & L : \text{even} \\ 0, \pm 1, \cdots, \pm(L-1)/2 & L : \text{even} \end{cases} \tag{4.49}$$

The EEs given by equation (4.48) correspond to the ones where $\nu_p \simeq 1/2$ which therefore contribute the most to the entanglement entropy $S_L$. In fact, making the approximation $\epsilon_p \approx \Delta_L \, p$, we can compute $S_L$ in the limit $L \gg 1$,

$$\begin{aligned} S_L =& \sum_p \left[ \frac{\log(1+e^{\epsilon_p})}{1+e^{\epsilon_p}} + \frac{\log(1+e^{-\epsilon_p})}{1+e^{-\epsilon_p}} \right] \approx 2 \int_{-\infty}^{\infty} dx \, \frac{\log(1+\exp(\Delta_L x))}{1+\exp(\Delta_L x)} \\ =& \frac{\pi^2}{3\,\Delta_L}. \end{aligned} \tag{4.50}$$

This equation is rather interesting since it relates $S_L$ to the inverse of the entanglement spacing $\Delta_L$ and connects with previous results in the literature (Peschel and Truong, 1987; Cardy and Peschel, 1988; Okunishi, 2005; Lepori *et al.*, 2013). First of all, in the critical case, that is $z = 0$, where $S_L \approx 1/6 \log L$, it implies that $\Delta_L \propto 1/\log L$, as shown by Peschel (2004). This result has wider implications that lead to the understanding of the ES as the energy spectrum of a boundary CFT on a strip of effective width $\propto \log L$ (Läuchli, 2013). The computation in equation (4.50) is similar to the one by (Calabrese and Cardy, 2004) for the non critical Ising and XXZ models, which leads to the equation $S_L = c/6 \log \xi$ where $\xi$ is the correlation length and is proportional to the inverse of the level spacing of the spectrum of the corner transfer matrix Hamiltonian on these models.

The dependence of the entanglement spacing $\Delta_L$ on the system size $L$ has a different behavior for $\alpha = 1$ and $\alpha < 1$. Figure 4.11 shows some $\Delta_L$ curves, for different values

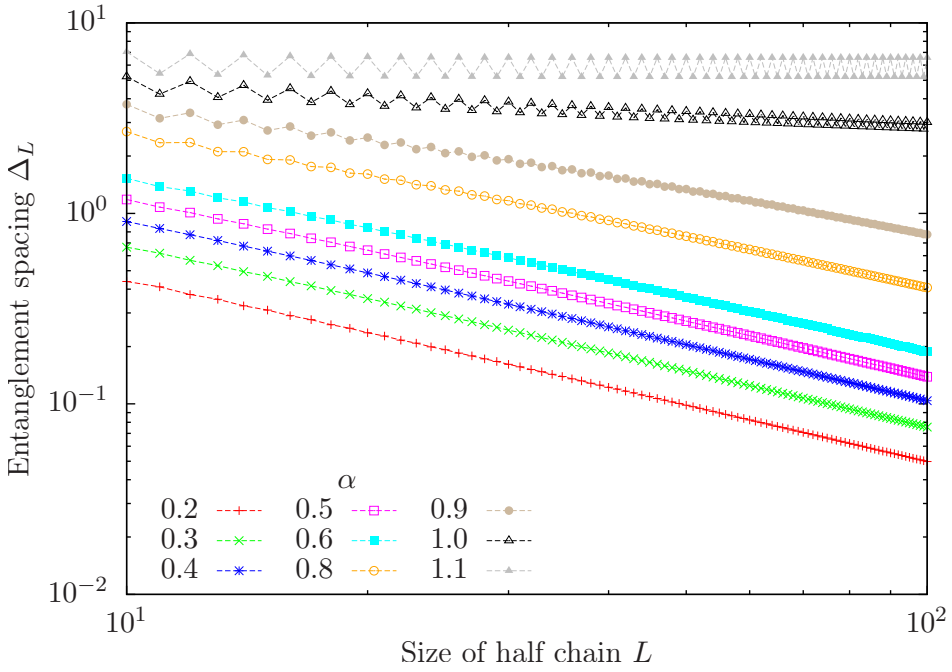


Figure 4.11: Entanglement spacing $\Delta_L$ as a function of $L$ for different values of $\alpha$. Notice the behavior $\propto 1/\log L$ for $\alpha = 1$ and $\propto 1/L$ for $\alpha < 1$ and $L$ large. The case corresponding to $\alpha = 1.1$ shows a qualitatively different behavior.

of $\alpha$, in scale $\log L$. As soon as $\alpha < 1$ and large enough $L$ we obtain a trend towards a power-law decay, which, for large $L$, converges to $\Delta_L \approx 1/L$. Combining this with equation (4.50), yields the volume law for the entanglement entropy: $S(L) \approx 1/\epsilon \approx L$, as expected.

Based on equations (4.32) and (4.50) we proposed the following Ansatz for the entanglement spacing (Ramírez *et al.*, 2014a)

$$\Delta_L \approx \frac{\pi^2/3}{\frac{1}{6}\tilde{c}(z)\log L + \tilde{d}(z) + \tilde{f}(z)L^{-\tilde{K}(z)}}, \tag{4.51}$$

where the functions $\tilde{c}(z)$, $\tilde{d}(z)$, $\tilde{f}(z)$ and $\tilde{K}(z)$ depend on the parity of $L$. This formula is extremely accurate with a $\chi^2$ of order $10^{-12}$ in the range $z \in [0, 2]$. Figure 4.12(a) plots the values of $\Delta_L$ as a function of $L$ for different values of $z$. Notice that the parity oscillations of $L$ are reminiscent to those of $S_L$. The functions $\tilde{c}(z)$, $\tilde{d}(z)$ and $\tilde{f}(z)$ behave in a similar (though not identical) way to their pairs $c(z)$, $d(z)$ and $f(z)$ in the interval $z \in [0, 2]$, especially for even values of $L$. For larger $z$ those fits lose quality. Notice that $\tilde{K}(z)$ is not 1, but close to 0.25.

Finally, in order to verify equation (4.50) we plot in figure 4.13 the product $S_L\Delta_L$, which shows that for $\alpha \leq 1$ the curves approach the constant $\pi^2/3$ for large values of $L$. For $\alpha = 1.1$, which is gapped, the product converges also to a constant, but not $\pi^2/3$, i.e. it corresponds to a model with different qualitative behavior.

For large values of $L$, we can approximate the ES as $\epsilon_p \simeq \Delta_L\, p$, the level spacing

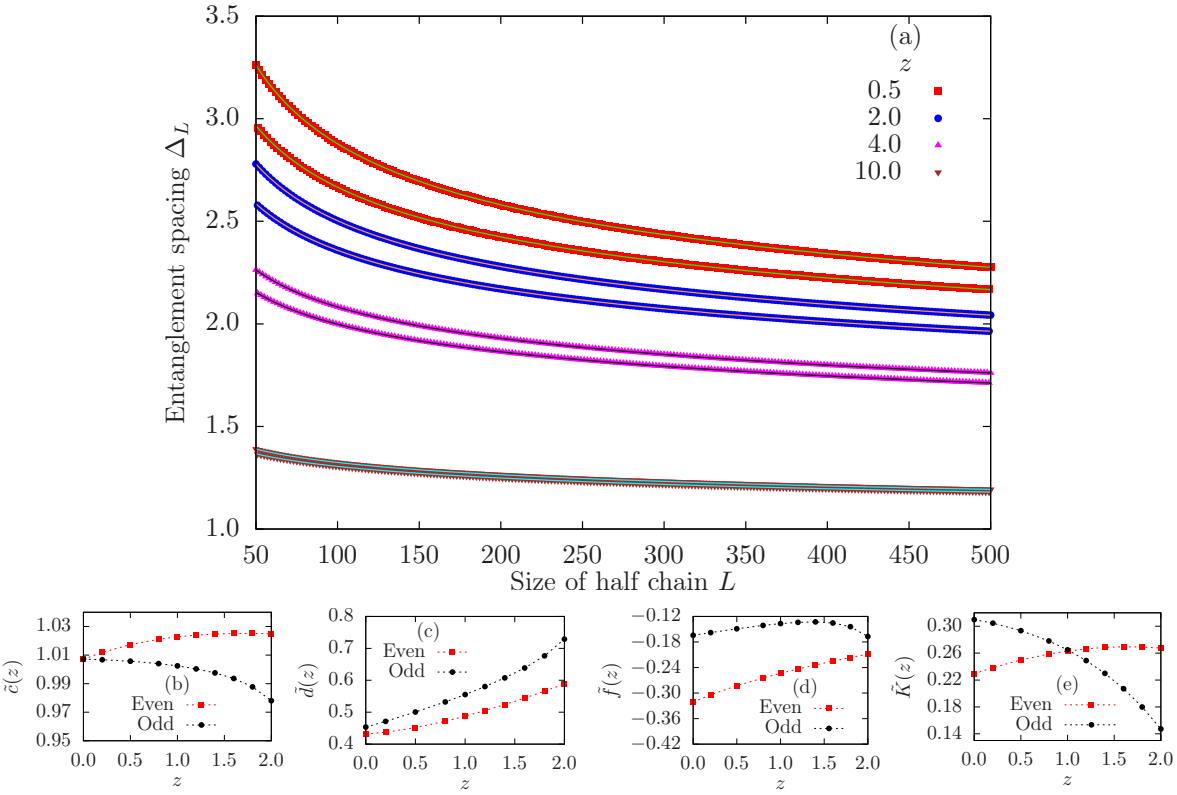


Figure 4.12: (a) Entanglement spacing $\Delta_L$ as a function of the system half size $L = 50, \ldots, 500$. For each value of $z$ the top (bottom) curves correspond to $L$ even (odd). Solid lines are fits to equation (4.51) with $\chi^2 \sim 10^{-12}$. (b)-(e) Functions $\tilde{c}(z)$, $\tilde{d}(z)$, $\tilde{f}(z)$ and $\tilde{K}(z)$, in the interval $z \in [0, 2]$ for $L$ even (odd).

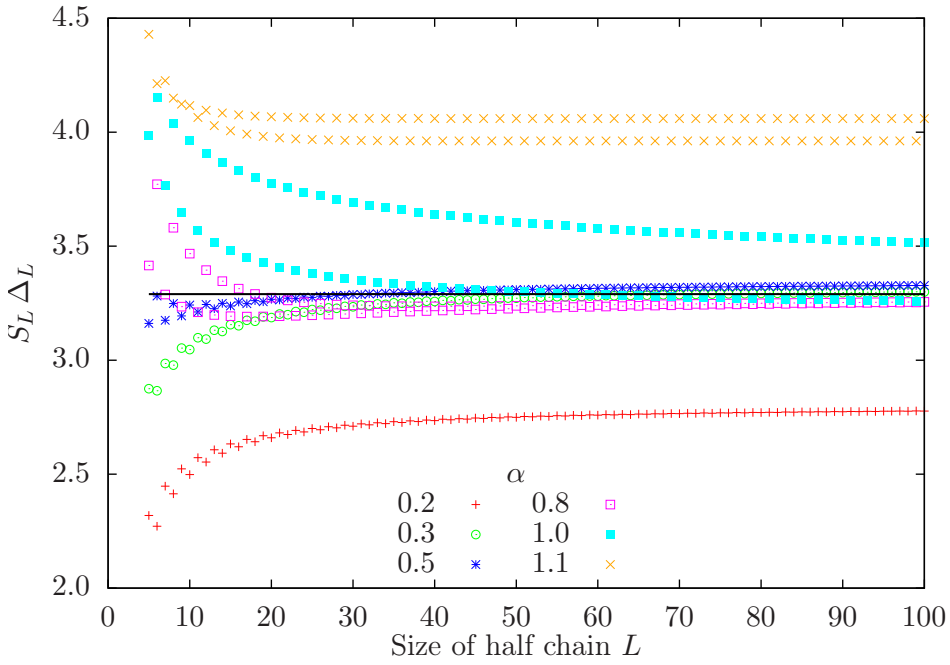


Figure 4.13: Plot of the product $S_L \Delta_L$ to illustrate equation (4.50). The black straight line is the constant $\pi^2/3$.

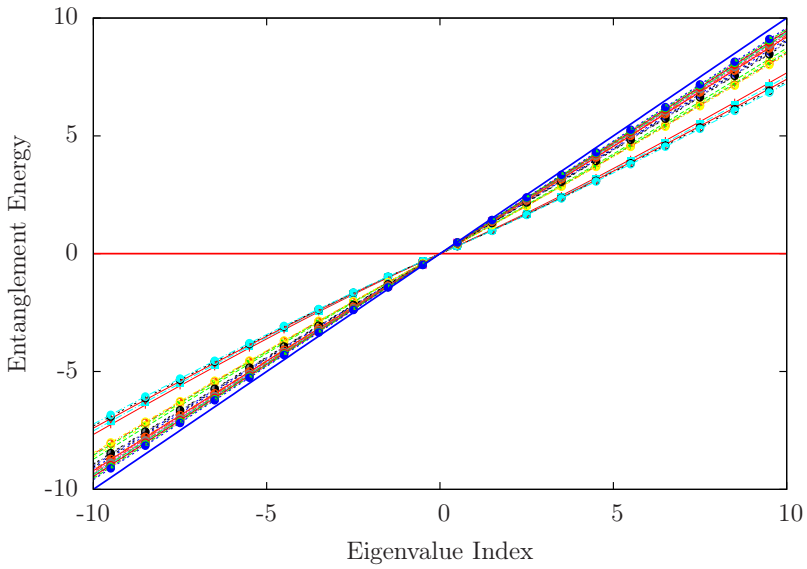


Figure 4.14: Entanglement single-body energies $\epsilon_p$ for different values of $L$ (from 60 to 160) and $z$ (from 5 to $L$ in each case, i.e. $\alpha = 0.61$), multiplied by $z/(2\pi^2)$. As predicted, they collapse to the diagonal line, following equation (4.55), $\epsilon_p \simeq 2\pi^2 p/z$.

$\Delta_L$ given by equation (4.50) can be approximated to

$$S_L \approx \frac{\pi^2}{3\Delta_L}, \tag{4.52}$$

which, using equations (4.26) and (4.30), implies

$$\Delta_L \approx \frac{2\pi^2}{hL} = \frac{\pi\beta}{L}. \tag{4.53}$$

Hence, the density matrix can be expressed as

$$\rho_A \approx e^{-\beta H_{CFT}}, \tag{4.54a}$$

$$H_{CFT} = \frac{\pi}{L}\sum_p p\, b_p^\dagger\, b_p, \tag{4.54b}$$

where $H_{CFT}$ is the CFT Hamiltonian of half of the chain. Thus, the single-body entanglement energies should fulfill, for different values of $L$ and $z$, the following law:

$$\epsilon_p \simeq \beta\, \epsilon_p^{CFT} = \left(\frac{2\pi}{h}\right)\left(\frac{\pi}{L}\,p\right) = \frac{2\pi^2}{z}\,p, \tag{4.55}$$

which we can see confirmed in the results of figure 4.14.

We then arrive at the conclusion that the rainbow state can be written as

$$|\psi_{CSP}\rangle = \sum_n e^{-\beta E_n/2}|n\rangle_L\,|n\rangle_R, \tag{4.56}$$

where $|n\rangle_R$ and $|n\rangle_L$ are orthonormal basis for the right and left pieces of the chain whose Hamiltonians are isomorphic to $H_{CFT}$ given in equations (4.54).

A pure state of the form given by equation (4.56) is called a thermo field state which links the entanglement structure to the emerging geometry of space-time. It has been employed in connection with black holes and the EPR=ER conjecture (Hartman and Maldacena, 2013; Maldacena and Susskind, 2013). In analogy to those studies, we can consider the temperature $T = 1/\beta$ to be related to the surface temperature of a black hole with gravity acceleration $g = 2\pi T$ or, alternatively, the temperature measured by a Rindler observer with acceleration $a = 2\pi T$. Looking at equation (4.40), we see that the constant $h$ plays that role in our model.

Numerical evidence for other cases where $\rho \sim e^{-H_{CFT}}$ was explored before in different systems Läuchli (2013). Thermal density matrices of this form have also been found for topological quantum states in $2+1$ dimensions, e.g. general quantum Hall states, which possess edge states described by a chiral CFT in $1+1$ dimensions (Qi *et al.*, 2012)

## 4.4 Generalizing the Rainbow State

### 4.4.1 Heisenberg model

The deformation applied to the inhomogeneous XX model, discussed in section 4.2, can be immediately generalized to any 1D system with OBC whose dynamics is described by a local Hamiltonian, i.e. $H = \sum_{i=1} h_{i,i+1}$, whose exponential deformation for a system of $N = 2L$ sites is given by (Ramírez *et al.*, 2014b)

$$H_L(\alpha) = J_0(\alpha)\; h_{\frac{1}{1},-\frac{1}{2}} + \sum_{i=\frac{1}{2}}^{L-\frac{3}{2}} J_i(\alpha)\; \left[h_{i,i+1} + h_{-i,-(i+1)}\right], \tag{4.57}$$

where $J_i(\alpha)$ are engineered to follow the same parametrization used for the free fermion system (cf. equation (4.2)):

$$\begin{cases} J_0 & = 1, \\ J_i(\alpha) & = \alpha^{2i}, \quad i = \frac{1}{2}, \ldots, L - \frac{3}{2}. \end{cases} \tag{4.58}$$

We shall consider the exponential deformation applied to the spin-1/2 Heisenberg Model which was described in section 2.3, thus $h_{i,i+1} = \vec{S}_i \cdot \vec{S}_{i+1}$. If $J_k$ is the strongest coupling in $\{J_i\}$, the Dasgupta-Ma RG equation to find the effective couplings is given by (Refael and Moore, 2009)

$$J_k^{(R)} = \frac{J_{k-1} J_{k+1}}{2 J_k}, \tag{4.59}$$

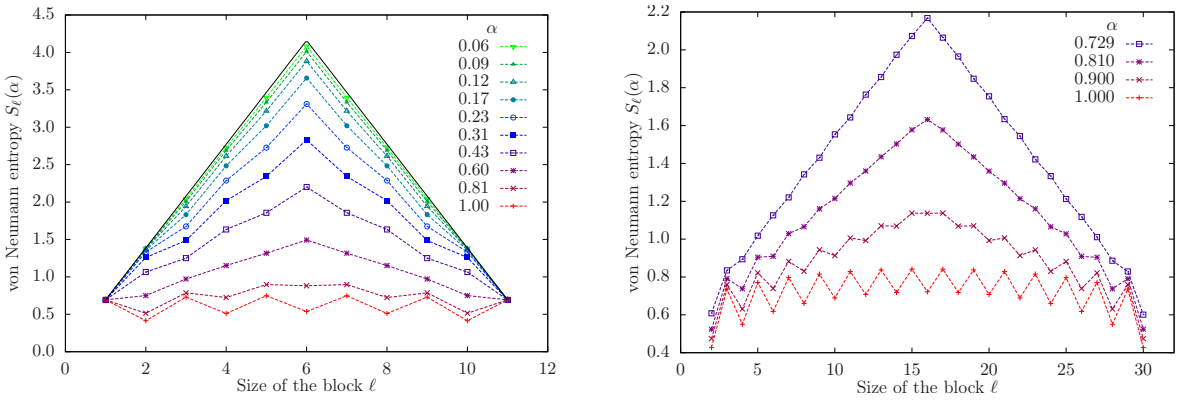


Figure 4.15: Left: von Neumann entropy of the deformed Heisenberg system and $L = 6$ (12 sites), where all the values of $\alpha$ are explored. Right: system with $L = 16$ (32 sites) studied with the DMRG method. The fast increase of entanglement of the half-chain limits the range of $\alpha$ where the method can be applied.

which differs from the computation of the effective coupling of the XX model (cf. equation (2.28) in section 2.7) by a factor of 2 in the denominator. In the strong inhomogeneity limit, i.e. $\alpha \to 0^+$, one obtains again the rainbow state made of valence bonds across the middle of the chain.

The numerical study of the uniform to rainbow transition is more involved than in the free fermionic case, because the GS cannot be obtained via the single-body procedures described in chapter 2. For very small system sizes, we have used exact diagonalization of the many-body Hamiltonian, while for larger sizes we have employed the density matrix renormalization group (DMRG) method described in section 1.3. The problem with the latter method is that we cannot reach very low values of $\alpha$, since the entanglement entropy of a block $B$ with the rest of the system grows linearly with the system size, thus the number of retained states grows exponentially with $S_L$. [2]

Figure 4.15 summarizes our results: the left panel shows the exact von Neumann entropy $S_\ell(\alpha)$ as a function of the block size $\ell$ for a system of $L = 6$, i.e. 12 sites. Notice the black line, which marks the strong inhomogeneity limit. The right panel shows the von Neumann entropy $S_\ell(\alpha)$ for a system of $L = 16$, i.e. 32 sites, but where $\alpha$ varies in the range $[0.7, 1]$. In both cases we can see the development of the tent shape, which is the hallmark of the volume-law (cf. section 4.3.1).

### 4.4.2 2D extension of the Rainbow State

A natural question is: can the 1D results be extended to 2D? In other terms, can we find a local 2D Hamiltonian whose GS violates maximally the area law? We shall next show that this is indeed possible in a rather simple way.

Let us consider a $2L \times 2L$ square lattice whose sites are labeled by $X = (x, y)$ with

[2] There is an alternative route to study this problem with DMRG, as it was pointed to us by J. I. Cirac, folding the chain into a ladder. We will pursue this route in further works.

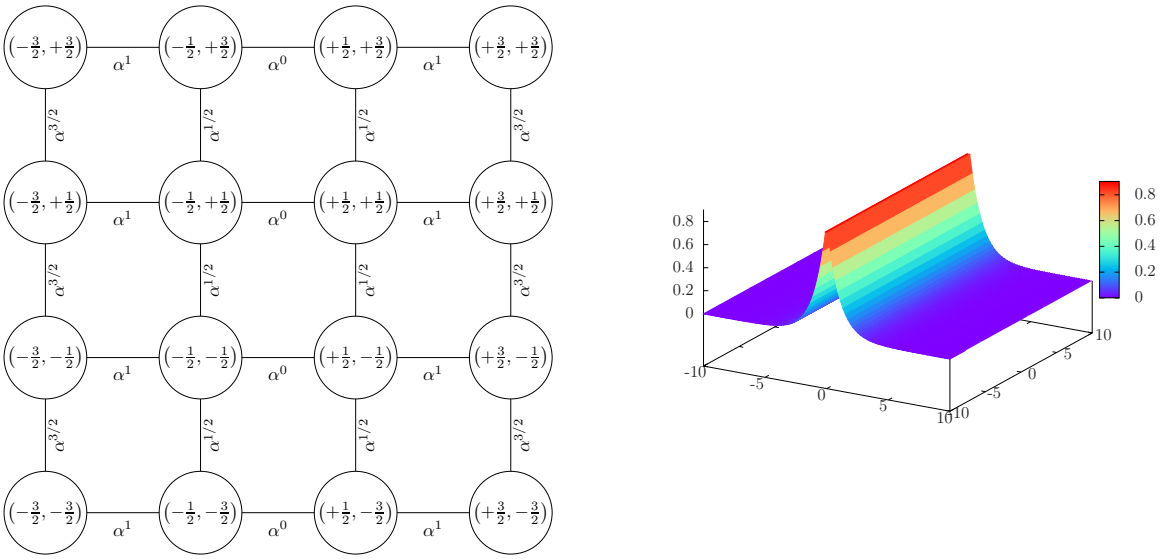


Figure 4.16: Left: a small region of the $2L \times 2L$ square lattice used to generate the 2D rainbow state. The nodes represent the sites, and the number attached to the link is the associated hopping amplitude, given by $\alpha^{|x|}$, with $x$ the horizontal coordinate of the middle point. Right: 3D view of the structure of the hopping distribution.

$x, y \in \{\pm 1/2, \pm 3/2, \cdots, \pm(L/2 - 1/2)\}$. We define a hopping Hamiltonian of the form:

$$H = -\sum_{\langle X, X' \rangle} t_{X,X'}\, c_X^\dagger c_{X'} + \text{h.c.} \tag{4.60}$$

where hopping matrix $t_{X,X'} = F\left((X + X')/2\right)$ is only determined by the center of the segment joining points $X$ and $X'$. In our case, we choose $F(x, y) = \alpha^{|x|}$, to resemble the 1D analogue. The left panel in figure 4.16 represents a small region of the lattice near the center. The right panel in figure 4.16 represents graphically the engineered distribution $F(x, y)$ for the elements of the inhomogeneous hopping matrix $t_{X,X'}$.

Figure 4.17 shows the entropy per unit length of a block composed of the left half of the system $S_L(\alpha)/L$ for different values of the deformation parameter $\alpha$. The solid lines represent fits to an expression of the form

$$\frac{S_L(\alpha)}{L} \simeq A(\alpha)L + B(\alpha)\log(L) + C(\alpha), \tag{4.61}$$

where a non-zero value for the linear term will denote a volumetric behaviour of the entanglement entropy. The logarithmic term is added in order to predict the correct behavior for the weak inhomogeneous limit, i.e. $\alpha \to 1^-$ (Gioev and Klich, 2006). The fits can be seen in table 4.2. Notice the low values of $\chi^2$ for $\alpha < 1$ and the increase of the volume coefficient with decreasing $\alpha$.

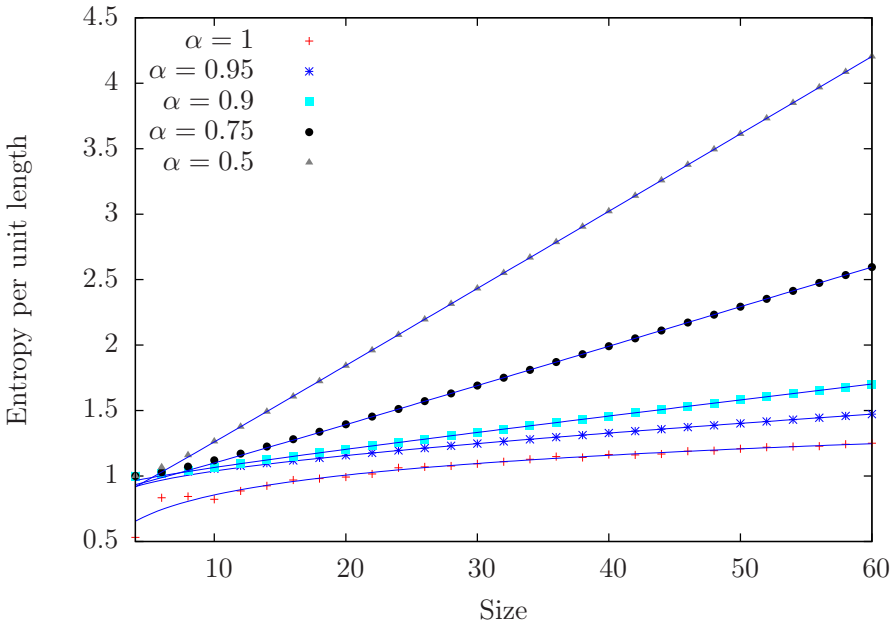


Figure 4.17: Entanglement entropy of the left half of the system, per unit length of the boundary, for different values of $\alpha$ for a 2D concentric singlet phase.

| $\alpha$ | $A(\alpha)$ | $B(\alpha)$ | $C(\alpha)$ | $\chi^2$ |
|---|---|---|---|---|
| 1 | 0 | 0.234 | 0.29 | $3 \cdot 10^{-5}$ |
| 0.95 | 0.0053 | 0.0940 | 0.77 | $10^{-9}$ |
| 0.9 | 0.0116 | 0.0330 | 0.87 | $10^{-9}$ |
| 0.75 | 0.0307 | $-0.0225$ | 0.85 | $10^{-9}$ |
| 0.5 | 0.0594 | $-0.015$ | 0.70 | $10^{-9}$ |

Table 4.2: Fitting parameters for the 2D entropy function in equation (4.61).

## 4.5 Qubistic picture of the Rainbow State

Qubism (Rodríguez-Laguna *et al.*, 2012) is a pictographic representation for quantum many-body states with the peculiarity that it allows for the visualization of entanglement. In summary, an $N$ qubit wavefunction is shown on the $[0,1]^2$ square divided into $2^{N/2} \times 2^{N/2}$ cells. Each of the $2^N$ wavefunction component are depicted into one of the cells, following a recursive pattern, in which the $i$-th qubit is associated with the $i$-th length scale, in decreasing order.

Figure 4.18 represents the qubistic plots of the rainbow ground state in 1D for two different sizes, $2L = 10$ and $2L = 12$, and three values of $\alpha = 0.01$, 0.3 and 1. Therefore, the top panels correspond to the ground state of the free fermion model (cf. section 2.5), and the bottom panels represent the rainbow states (cf section 4.3). Notice that the representation is formed only by a finite and small set of points.

Entanglement between the first pair of qubits and the rest can be visualized in the following way (Rodríguez-Laguna *et al.*, 2012). Break the full square into $2 \times 2$ square of half-size. Count the number of different (strictly, linearly independent) images among the small squares. That number is an upper bound for the Schmidt rank, which is a measure of entanglement as described in section 1.2. The same procedure can continue, for the block composed of the first four qubits, if we decompose the original square into a $4 \times 4$ grid. In our case, notice that the dots in each of the small squares form a similar but different pattern. In fact, the number of different (independent) images coincides with the number of squares, 4 for the first two qubits, 16 for the first four, etc. This shows that the Schmidt rank grows as $2^\ell$, i.e., entanglement is maximal.

Another visualization possibility would be given by the so-called *entanglement contour*, which aims at locating in real space the entangled degrees of freedom within a block (Chen and Vidal, 2014). As we can see in the qubistic plot, the entangled degrees of freedom are totally located in real space in the rainbow state and span the whole block for a left-right partition.

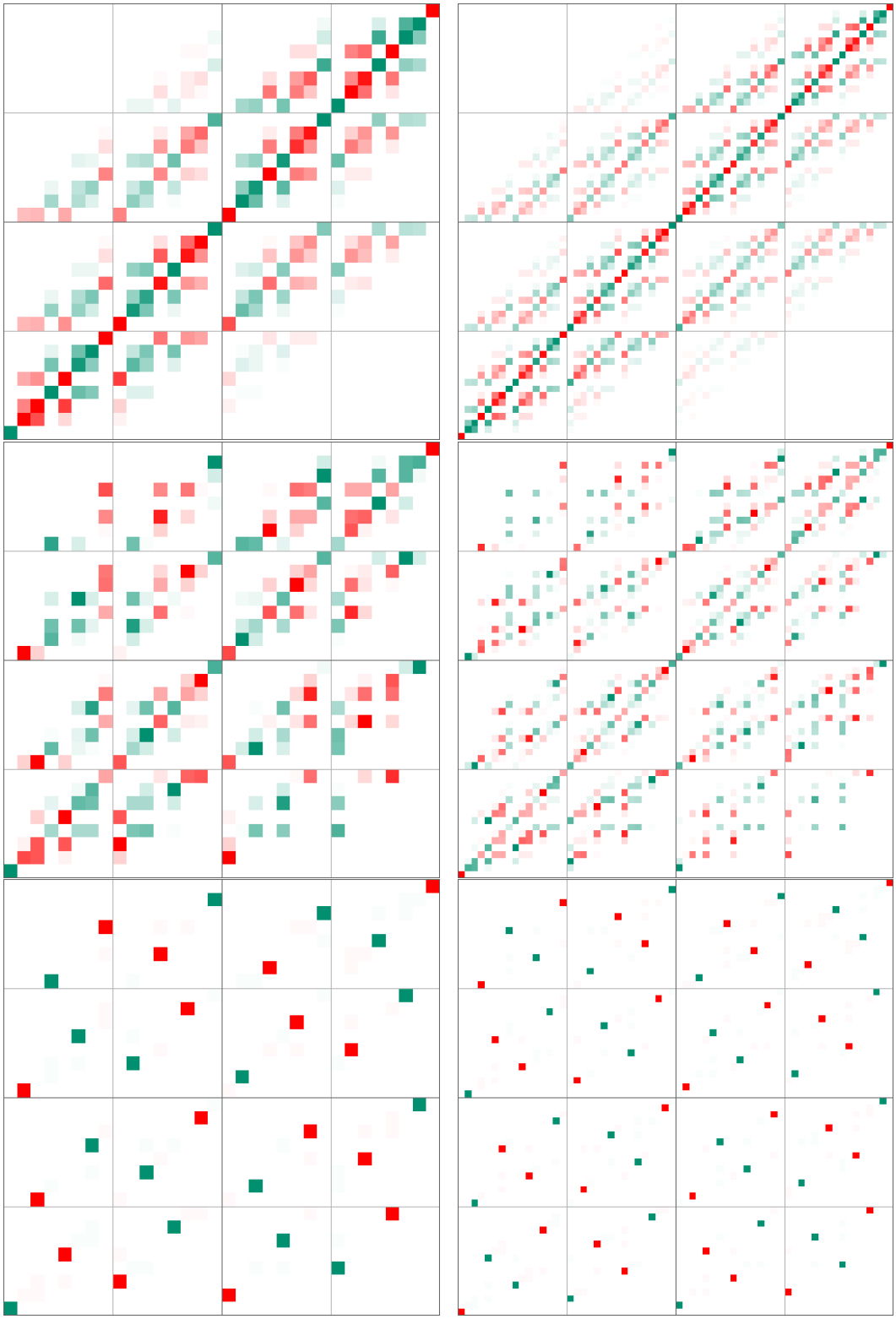

Figure 4.18: Qubistic picture of the rainbow state for different sizes of the system $2L = 10$ and $2L = 12$ (left and right columns) and three values of $\alpha = 0.01$, 0.3 and 1 (from bottom to top). Color intensity denotes the wavefunction amplitude and hue denotes phase: red is positive and green negative.

# Chapter 5

# Quenched Dynamics of Valence Bond States

## 5.1 Introduction

The recent experimental advances in ultracold atom technology have motivated a surge of interest in the non-equilibrium dynamics of closed quantum systems after a sudden change of the Hamiltonian, also known as a quantum quench (Polkovnikov *et al.*, 2011; Daley *et al.*, 2012). In a quenching protocol, the ground state (GS) of a certain Hamiltonian $H_0$ is obtained, and then suddenly changed into a quenching Hamiltonian, $H$, which does not commute with $H_0$. Further evolution is assumed to take place without dissipation, i.e. to be unitary. Quenches are termed *local* if the new Hamiltonian $H$ differs from the original one only in the addition of a local operator (Calabrese and Cardy, 2007; Eisler *et al.*, 2008). For example, a *joining* quench is the result of getting two homogeneous systems with open boundaries and adding a link between them, thus quenching to a larger homogeneous Hamiltonian (Calabrese and Cardy, 2007; Eisler *et al.*, 2008). The *splitting* quench is its opposite: start with a homogeneous system and split into two disconnected halves (Zamora *et al.*, 2014; Torlai *et al.*, 2014).

The propagation of information in a local quench is limited. In fact, dynamical effects in quantum many-body systems with only local interactions are subject to the *Lieb-Robinson bound* (Lieb and Robinson, 1972), which imposes the existence of an equivalent to the speed of light: the amount of information which is transmitted faster than a certain Lieb-Robinson velocity, $V_{LR}$, is exponentially suppressed. Thus, after a local quench, one can expect a transient time before the entanglement entropy of a given block starts to grow, given by its distance to the quench location divided by $V_{LR}$. Moreover, theoretical results obtained for 1D systems using conformal field theory (Calabrese and Cardy, 2005, 2006) allowed to formulate the so-called *quasiparticle picture*. In the initial state, entangled quasiparticles are established at a distance of the order of the correlation length. After the quench, they start to propagate classically

through the system, thus increasing linearly the effective correlation length. This picture predicts that the entanglement entropy of arbitrary blocks will grow linearly with time just after the quench, an effect which has been experimentally observed in different situations (Schachenmayer *et al.*, 2013).

Is the quasiparticle picture still valid when the initial state contains already very long distance correlations? As it was pointed out in the previous chapters, the GS of local Hamiltonians in 1D can have bonds of arbitrarily long length, if the system is inhomogeneous. Indeed, in section 4.2 we have engineered a 1D valence bond state (VBS) with a concentric structure around the center of the chain, which we called *rainbow state*, that present a maximal growth of the entanglement (Vitagliano *et al.*, 2010; Ramírez *et al.*, 2014b, 2015). Since the entanglement entropy of a VBS is proportional to the number of bonds cut by the block, the entanglement of the left half of the chain grows linearly with the system size, i.e. a volumetric growth of the entanglement. What would be the time-evolution of entanglement in this situation?

In this chapter we study the time-evolution of different VBS, specifically the rainbow state and the dimer state, after a quench to a homogeneous Hamiltonian in 1D. The subsequent evolution of the entanglement presents very intriguing features. To start, entanglement of the half-chain of the rainbow decreases linearly with time and, after it reaches a minimal value, it increases again, eventually reaching (approximately) the initial state. Blocks of smaller sizes only decrease after a certain transient time, which can not be explained via a Lieb-Robinson bound, since the quench is global. Also, the correlation between pairs of sites suggests the motion of certain objects or quasiparticles, but with apparent *superluminal* velocity. The dimer state, on the other hand presents an approximately opposite behaviour: the entanglement grows linearly for all blocks, reaching a maximally entangled state which resembles the rainbow state. Afterwards, entanglement decreases again, cyclically.

After a phenomenological discussion of the time-evolution of the dimer and rainbow states after a quench to a homogeneous Hamiltonian, we will attempt a theoretical explanation in terms of an extension of the quasiparticle picture of (Calabrese and Cardy, 2005).

## 5.2 Quenching a Free Fermion State

Let us consider a generic Slater determinant that is defined by

$$|\Psi_0\rangle \equiv \prod_{k\in K} b_k^\dagger |0\rangle, \tag{5.1}$$

in terms of some fermionic operators $b_k^\dagger = \sum_j B_{jk} c_j^\dagger$, where $c_j^\dagger$ is the creation operator on the $j$-th site, $|0\rangle$ is the Fock vacuum and the set $K$ contains the single particle energy

levels that are occupied.

Now, let the state evolve under the action of the free fermion Hamiltonian (recall Hamiltonian (2.1) in section 2.2)

$$H \equiv -\sum_{i,j} \frac{T_{ij}}{2} c_i^\dagger c_j + \text{h.c.} \tag{5.2}$$

where $T$ is the hopping matrix.[1] When a Slater determinant which evolves under the action of a free fermion Hamiltonian remains as a Slater determinant throughout evolution. Therefore, the numerical study of the quench can be reduced to a single-body problem: the time-evolution of the single-body orbitals of the initial state under the action of the hopping matrix. Following the description given in section 2.2, we diagonalize the Hamiltonian (5.2) in terms of the fermionic operators $d_k^\dagger = \sum_j D_{jk} c_j^\dagger$, where $D$ is a unitary matrix whose columns are eigenvectors of $T$

$$H = \sum_k \epsilon_k d_k^\dagger d_k + E_0.$$

The time-evolved state is given formally by

$$|\Psi(t)\rangle = e^{-iHt}|\Psi_0\rangle, \tag{5.3}$$

however, for our case, we obtain a simpler expression in terms of a Slater determinant

$$|\Psi(t)\rangle = \prod_{k\in K} b_k^\dagger(t)|0\rangle, \tag{5.4}$$

where the time-dependent creation operators $b_k^\dagger(t)$ are given by

$$b_k^\dagger(t) = \sum_j B_{jk}(t)\, c_j^\dagger, \tag{5.5}$$

and

$$B_{jk}(t) = \sum_{m,n} D_{jm} \exp\left(i\epsilon_m t\right) D_{mn}^* B_{nk}. \tag{5.6}$$

Therefore, the correlation matrix and, following the procedure discussed in section 2.2, the entanglement entropies, can be obtained for all times with knowledge of this matrix $B_{jk}(t)$.

In this chapter we focus on two 1D VBSs: (i) the dimer state, which present only local correlations, and (ii) the rainbow state, which in contrast present long range correlations and, as discussed in chapter 4, it is a maximally entangled state.

[1] Note the change in the notation to keep $t$ for the time

## 5.3 Quenching from Dimer to Clean

Let us study the quench to a clean Hamiltonian starting from a VBS which presents only local correlations. Consider a system with $2L$ sites with indices $\{1, \ldots, 2L\}$ whose dynamics is described by the Hamiltonian with open boundary conditions (OBC)

$$H_D = -\sum_{j=1}^{2L-1} \left[1 + (-1)^j \delta\right] c_j^\dagger c_{j+1} + \text{h.c.} \tag{5.7}$$

where hoppings alternate between a strong value, $1+\delta$, to a weak one, $1-\delta$, characterized by the dimerization parameter $\delta$. The GS of the Hamiltonian (5.7) is the dimer state which can be written as

$$|D\rangle = \prod_{k=1}^{L} b_k^\dagger |0\rangle, \tag{5.8}$$

where the bond creating operators are defined as

$$b_k^\dagger \equiv \frac{1}{\sqrt{2}} \left(c_{2k-1}^\dagger - c_{2k}^\dagger\right), \tag{5.9}$$

for $k = 1, 2, 3, \ldots, L$. Thus, we can write

$$B_{ik} = \frac{1}{\sqrt{2}} \left(\delta_{i,2k-1} - \delta_{i,2k}\right). \tag{5.10}$$

Let $|D_0\rangle$ be the starting state defined by equation (5.8). At time $t = 0$ the system is quenched to a free fermions uniform Hamiltonian such as that defined in equation (5.2) with $T_{j,j+1} = 1$, then

$$H = -\frac{1}{2} \sum_{i=1}^{2L-1} c_i^\dagger c_{i+1} + \text{h.c.} \tag{5.11}$$

and the state proceeds to evolve. Notice that the Hamiltonian has OBC and its normalization is such that the Fermi velocity $v_F = 1$.

Figure 5.1 shows the numerical results for the evolution of the correlator after the quench. It shows a space-time diagram representing the absolute value of the correlation between site 1 and all other sites of the lattice, $|\langle\Psi(t)|c_1^\dagger c_i|\Psi(t)\rangle|$, in a system with $2L = 200$ sites. For time zero, we can see how site 1 is only correlated with site 2. But, as time evolves, the strongest correlation is established with a second site, $p(t)$, which moves rightwards with an approximately constant speed. When $p(t)$ reaches the site $2L$, the signal is reflected at the boundary and starts to move leftwards. It is relevant to notice that the propagation speed is twice the Fermi velocity: $p(t) \simeq 2v_F t$. This does not imply any violation of causality, since the correlation between site 1 and site $p(t)$

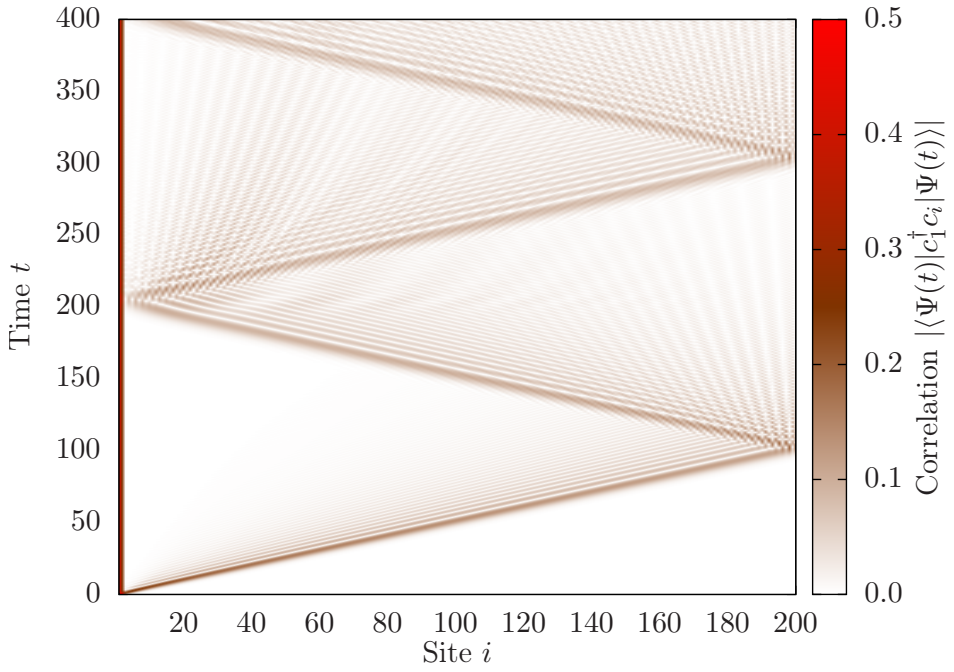


Figure 5.1: Space-time diagram of the evolution of the correlation for the quench of the dimer state to the clean Hamiltonian. The diagram shows the correlation between the left-most site with all other sites, $|\langle\Psi(t)|c_1^\dagger c_i|\Psi(t)\rangle|$, for a system with $2L = 200$ sites.

does not correspond to any moving object. Let us remind the reader that the quench is global quench and not local.

This results support the qualitative predictions of the Calabrese-Cardy picture since it shows that the bonds stretch linearly in time. Further discussion of the entanglement will be done in section 5.5.

## 5.4 Quenching from Rainbow to Clean

Let us study the quench to a clean Hamiltonian starting from the rainbow state described in section 4.2. The rainbow state is a VBS obtained as the GS of an inhomogeneous Hamiltonian which is engineered in order to obtain a maximal growth of the block entropy. The inhomogeneity is parametrized with the deformation parameter $\alpha$ which allows to move from the clean regime, i.e. $\alpha = 1$, to a strong inhomogeneity limit, i.e. $\alpha \to 0^+$.

For a system of $2L$ sites with indices $\{-L+\frac{1}{2},\dots,-\frac{1}{2},\frac{1}{2},\dots,L-\frac{1}{2}\}$, the rainbow state can be defined (cf. equation (4.8))

$$|\Psi\rangle \equiv \left(b^{s_L}_{-L+\frac{1}{2},L-\frac{1}{2}}\right)^\dagger \cdots \left(b^{+}_{-\frac{5}{2},\frac{5}{2}}\right)^\dagger \left(b^{-}_{-\frac{3}{2},\frac{3}{2}}\right)^\dagger \left(b^{+}_{-\frac{1}{2},\frac{1}{2}}\right)^\dagger |0\rangle, \tag{5.12}$$

where $s_L = (-1)^L$ can select either a bond or an anti-bond creating operators (cf.

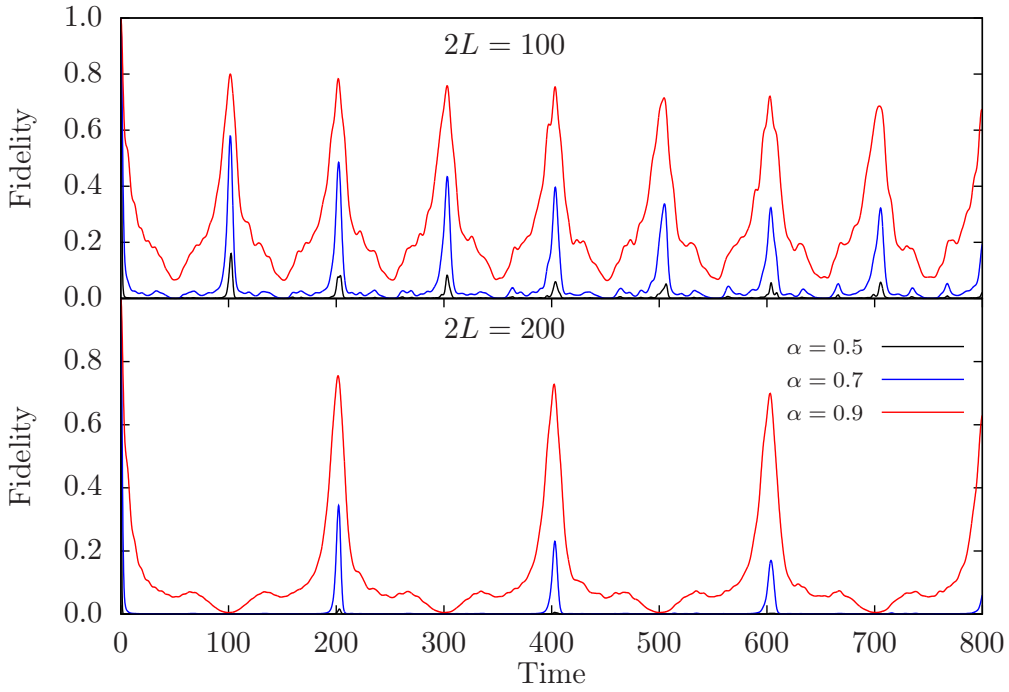


Figure 5.2: Fidelity between the initial and the time evolved state after a quantum quench to a clean Hamiltonian of the rainbow state. Top panel: a system with size $2L = 100$. Bottom: size $2L = 200$. The approximate Loschmidt echo is marked by the peaks at nearly periodic times, with a period which is approximately $T = 2L$.

equations (4.7) in section 4.2)

$$\left(b^{+}_{jj'}\right)^{\dagger} \equiv \frac{1}{\sqrt{2}}\left(c^{\dagger}_{j} + c^{\dagger}_{j'}\right), \tag{5.13a}$$

$$\left(b^{-}_{jj'}\right)^{\dagger} \equiv \frac{1}{\sqrt{2}}\left(c^{\dagger}_{j} - c^{\dagger}_{j'}\right). \tag{5.13b}$$

Let $|\Psi_0\rangle$ be the rainbow state defined in equation (5.12). At time $t = 0$ it undergoes a quench to a uniform Hamiltonian, given by

$$H = -\frac{1}{2}\sum_{i=-L+1/2}^{L-3/2} c^{\dagger}_{i}c_{i+1} + \text{h.c.} \tag{5.14}$$

with OBC. The normalization is chosen to let the Fermi velocity $v_F = 1$.

The first magnitude that we have studied is the *fidelity* of the state with respect to the initial state, as a function of time, $|\langle\Psi(t)|\Psi_0\rangle|$. Figure 5.2 shows this magnitude for two system sizes, $2L = 100$ and $2L = 200$, and several values of $\alpha$. Notice the approximate Loschmidt echo which appears for high values of $\alpha$, even for large systems, with periodicity $T = 2L$.

In figure 5.3 we show a space-time diagram of the correlation between the left-most site $-L + 1/2$ and all other sites, i.e. $|C_{-L+1/2}, i(t)| = |\langle\Psi(t)|c^{\dagger}_{-L+1/2}c_i|\Psi(t)\rangle|$, for a system with $2L = 128$ and $\alpha = 0.79$ (left) and for a system with $2L = 256$ and $\alpha = 0.89$

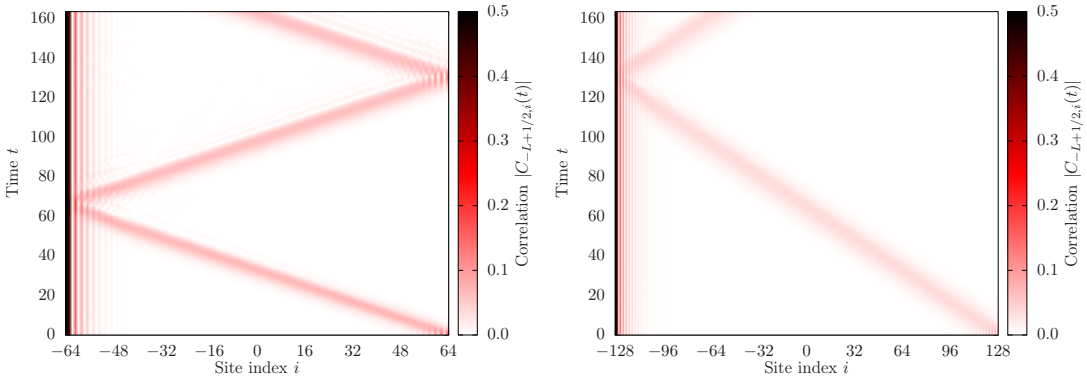


Figure 5.3: Space-time diagram showing the correlation between the left-most site and all other sites of the lattice, for a system of $2L = 128$ (left) and $2L = 256$ (right). Notice that, for time $t = 0$, the left-most and the right-most sites make up a Bell pair, but the right-most extreme of the pair moves leftwards with constant speed.

(right). At time zero, it only presents non-zero correlation with the right-most site. As time evolves, this Bell pair remains reasonably coherent with its ends contracting with a uniform speed $2v_F$ with good accuracy. When the bond has contracted to its minimum length, it starts to stretch again, with the same speed.

The time evolution of the full structure of the correlation matrix is given in figure 5.4. Each panel represents the quantum state at a different instant of time, which is marked with a label. The lines connecting the sites in the circumference provide a graphical representation of the full correlation matrix, $C_{ij}(t) = \langle\Psi(t)|c_i^\dagger c_j|\Psi(t)\rangle$. See appendix A.1 for a description of the graphical representation. The initial state is a rainbow state with $2L = 60$ and $\alpha = 0.25$. Notice that, at that time, each site establishes a strong bond with the opposite extreme, and some other less intense bonds. When the quench begins, the most salient feature is that the longest bond breaks into two symmetric bonds which, with one end on the extremes, start contracting with uniform speed $2v_F$. For time $T = 30$, i.e. $T = L$, these bonds have reached their minimal possible size, becoming short ranged. At that moment, the long distance bonds have all disappeared, and the entanglement is minimal. From that moment on, the system repeats almost the same steps backwards, returning to a similar state to the original one for $T = 2L$, as we can see in the last panel. This is a reflection of the Loschmidt echo which we pointed out in the study of the fidelity.

The top left panel in figure 5.5 shows the evolution of the von Neumann entanglement entropy for blocks of contiguous sites which extend from the left extreme of a system of $2L = 128$ sites. At time $t = 0$ each block has its maximal possible entropy. The maximal entropy block, which is the one that spans half the system size, starts out with a linear decrease which drags down the entropy of all other blocks, in such a way that larger blocks always have larger entropy. Once all the entropies have reached the same minimum, the dynamics repeats itself with a good accuracy (see the top right panel in figure 5.5).

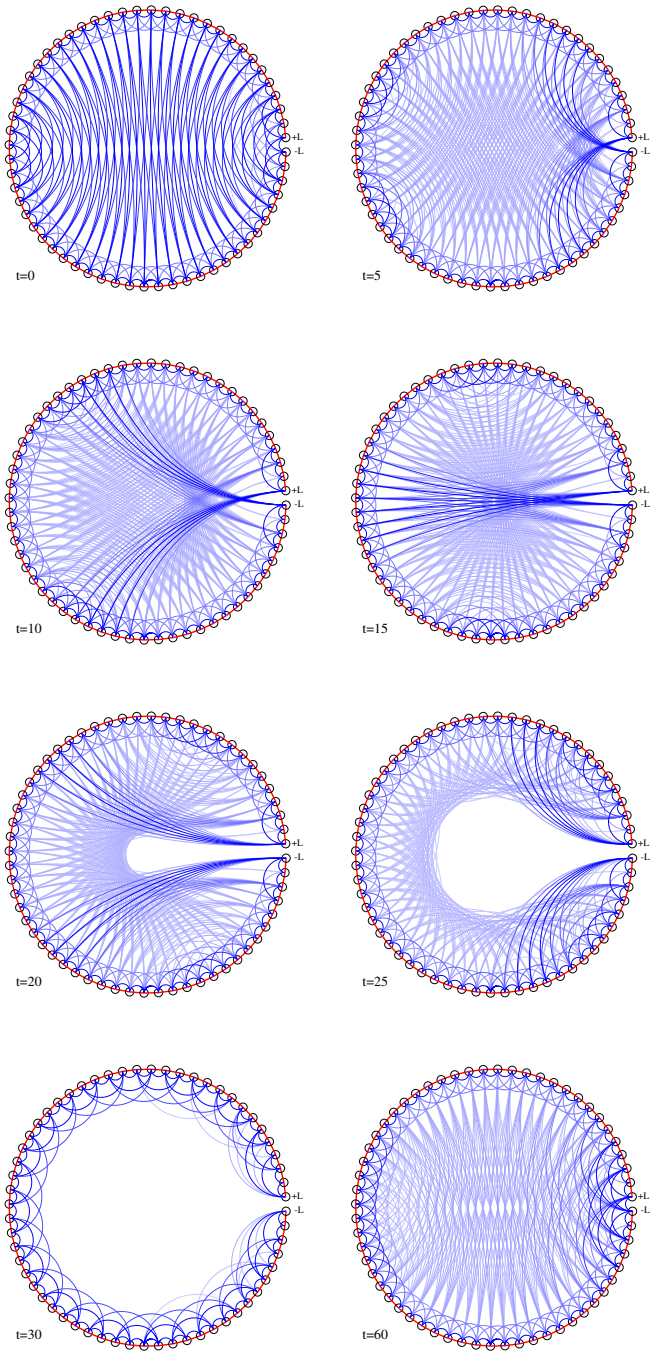


Figure 5.4: Time evolution of the correlator structure of the rainbow state under a quench to a clean Hamiltonian. The size of the system is $2L = 60$, and the initial state is the ground state of the rainbow Hamiltonian with $\alpha = 0.25$. Each frame represents the correlation matrix $C_{ij}(t) = \langle \Psi(t)|c_i^\dagger c_j|\Psi(t)\rangle$ for a different time, which appears close to each picture. Each line corresponds to an element of that matrix and the color intensity is related to $|C_{ij}(t)|$. The last frame corresponds to a time equal to the period.

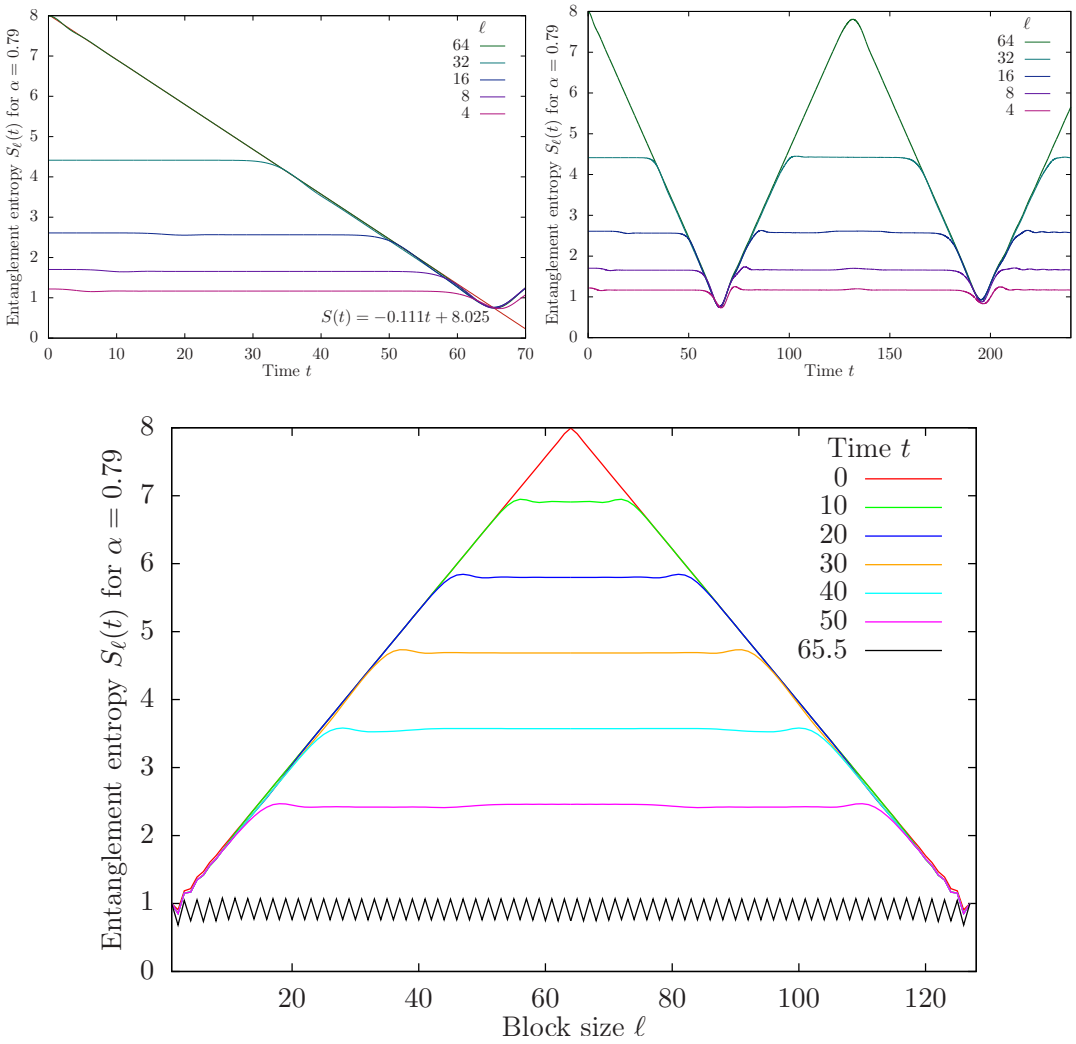


Figure 5.5: Top: time evolution of the entropy of blocks starting from the left extreme. Top-left: short time picture; Top-right: longer times. Notice the accurate time periodicity and the strict order: the entropy of a larger block is always strictly larger than the entropy of a smaller one. Bottom: entropy as a function of the block size, for different times.

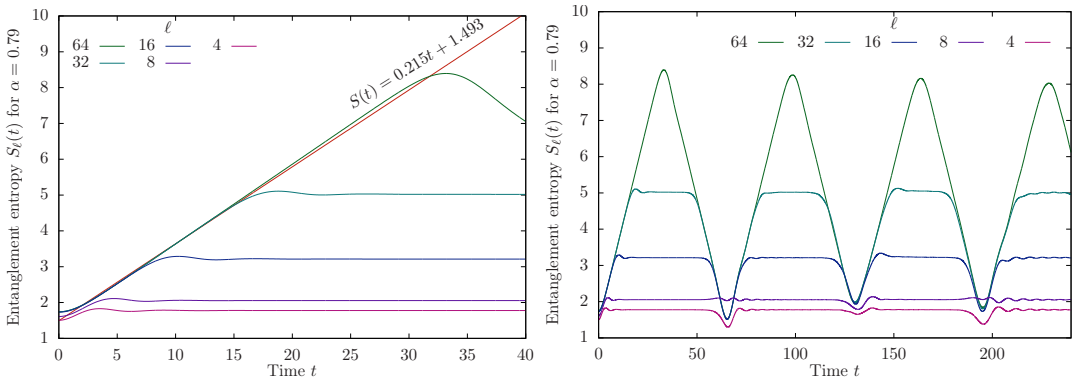


Figure 5.6: Time evolution of the entanglement entropy of central blocks. Left panel: short time; Right: longer times. All computations are made for $2L = 128$ and $\alpha = 0.79$.

The bottom panel of figure 5.5 shows the time evolution of the von Neumann block entropy $S(\ell)$ for $\alpha \to 0^+$. For time $t = 0$ we obtain the characteristic *tent* shape that was already reported by Ramírez *et al.* (2014b), which reflects the long distance Bell-pair structure. As time evolves, the maximal entropy decreases linearly in time, dragging all other entropies along, creating a plateau. When the time of the first reflection is reached, the system has minimal entropy, and a slightly dimerized entropy pattern is achieved. After that point, the entropies increase again, making up the tent again.

Figure 5.6 shows, in contrast, the time evolution of the entanglement entropy of centered blocks of different sizes, $\{-(\ell-1)/2, \cdots, (\ell-1)/2\}$. The entanglement starts out as zero for all blocks, which is a feature of the state, and it increases linearly with time until they saturate at a value which is lower than the maximum allowed value. They stay at that saturation value for a certain time, making up a plateau. For $\ell = L$, the plateau does not develop, and as soon as the entropy saturates, the entropy starts decreasing again. An oscillatory pattern develops from that moment.

## 5.5 The Ballistic Bond Picture

In order to try to explain the observed behavior, we have developed a simple *ballistic* picture, as a generalization of the *quasiparticle* image put forward by Calabrese and Cardy (2005) (see appendix A.3 for a brief summary) in order to explain the linear growth of the entanglement entropy. In their image, the original state is composed by a *soup* of particles which have established among themselves local bonds. The quench forces these particles to start traveling and, thus, the bonds stretch.

The ballistic bond picture proposes that, after a quench, each bond $(x_1, x_2)$ converts into four virtual particles, $x_{1L}$, $x_{1R}$, $x_{2L}$ and $x_{2R}$. Each left-particle ($x_{1L}$ and $x_{2L}$) propagates leftwards, while the right-particles ($x_{1R}$ and $x_{2R}$) move rightwards, with the same speed, equal to the Fermi velocity $v_F$. The virtual particles keep *partial* bonds among themselves. In principle, six bonds can be established among them, each one

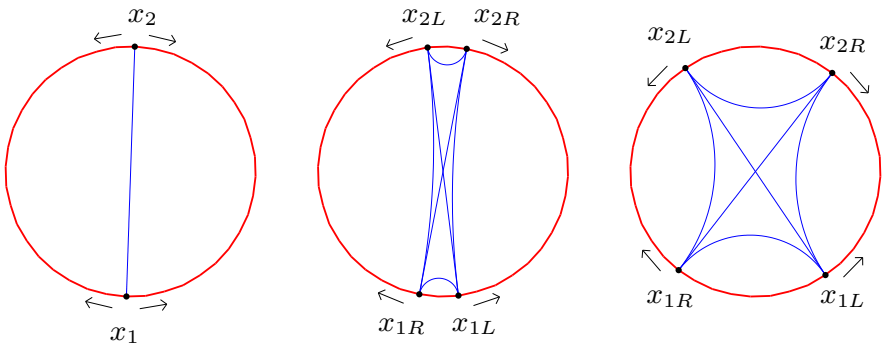


Figure 5.7: Illustration of the ballistic picture. Consider the dark bond to be the initial state. As time evolves, four virtual particles propagate, two from each extreme, in both directions. At all times, six virtual bonds may be established.

contributing an entropy $\log(2)/6$. See figure 5.7 for an illustration. Some of those bonds will carry the entanglement among them, and some will not. In the rainbow case, as we will see, the entanglement can be said to be carried by bonds between the virtual particles with the same velocities, i.e.: $(x_{1L}, x_{2L})$ and $(x_{1R}, x_{2R})$. It is not yet clear why those precisely. The last rule is that, if the boundaries are open, the virtual particles are reflected in them.

Figure 5.8 shows the comparison between the ballistic picture and the exact computation of the entanglement after the rainbow has been quenched, for a system with $L = 128$ and open boundaries. The time axis is the same for the ballistic and exact calculations. The system repeats approximately the same configuration after a time $T = L$, while the periodicity is exact within the ballistic approximation. Notice that the plateau for lower system sizes appear in the ballistic picture, showing that it is a merely combinatorial effect. Figure 5.9 shows a few snapshots of the bond structure, which accounts for the entropy, according to the ballistic picture.

The explanation for the apparent superluminal propagation of the information in the correlation is very simple within the ballistic picture. The bond extremes are moving with the Fermi velocity $v_F$, indeed. But the observed moving maximum for the correlations between a certain site and all other sites corresponds to different original bonds for different times. In other words, let us say that, at time $t = 0$, site $x_1$ is linked to site $x_2$ by a certain bond. At time $t = \Delta t$, that bond is not touching sites $x_1$ and $x_2$ any more. Instead, a new bond is passing through $x_1$, and also touches $x_2'$. The position of this new $x_2'$ need not satisfy the causality relation, $|x_2' - x_2| < v_F \Delta t$.

In order to investigate the applicability of the ballistic picture to the quench of the dimerized state, we have to consider which virtual sites are to be connected by bonds. If we connect, as in the rainbow case, the ones with the same velocity, then each bond will simply undergo "parallel transport" around the system, without any stretch. Instead, we should consider the bonds joining the virtual particles with opposite velocities. If we do so, we obtain a behavior as the one shown in figure 5.10. The *pure* dimerized

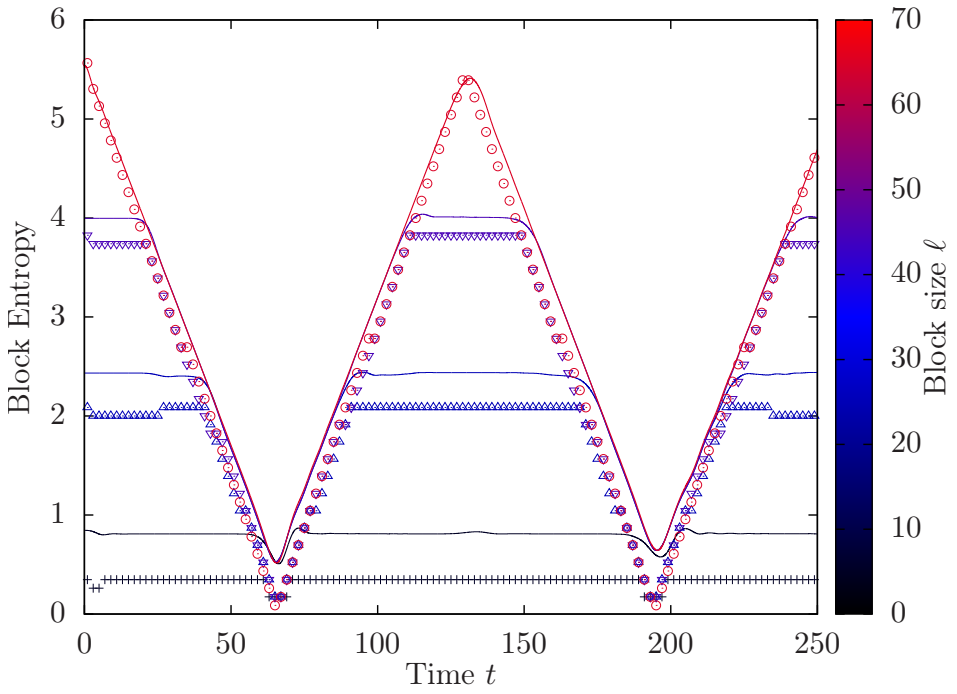


Figure 5.8: Comparison between the entanglement evolution for different sizes of block $\ell$ after a quench of the rainbow state, ballistic picture (with points) and exact diagonalization (with lines), for a system with $L = 128$ and open boundaries. The time axis is the same for both, but the entropy axis is re-scaled.

state is the state obtained with $\delta = 1$.

Figure 5.11 show snapshots of the time evolution of the correlator structure for the dimer state for a system of $2L = 60$ sites. For each snapshot, the blue lines represent the elements of the correlation matrix $C_{ij}(t)$. At $t = 0$ all correlators are local and after the quench, the correlation with distant sites increases.

Figure 5.12 shows the bond structure obtained with the ballistic picture, for $t = 0$ the bonds are locally established. After the quench, longer bonds appear as the virtual particles move through the system. Note how the evolution of the dimer state given by the ballistic bond picture in figure 5.12 looks like a time-reversed version of the ballistic evolution of the rainbow state (cf. figure 5.9).

### 5.5.1 Towards an explanation of the Ballistic picture

We would like to derive the ballistic picture from first principles. In particular we would like to understand the differences between the rainbow and the dimer states, which present different types of bonds. The calculation done in this section can be extended for a generic VBS.

The dimer state can be defined using equations (5.8) and (5.9)

$$|D\rangle = 2^{-L/2} \prod_{j=1}^{L} \left( c^\dagger_{2j-1} + c^\dagger_{2j} \right) |0\rangle. \tag{5.15}$$

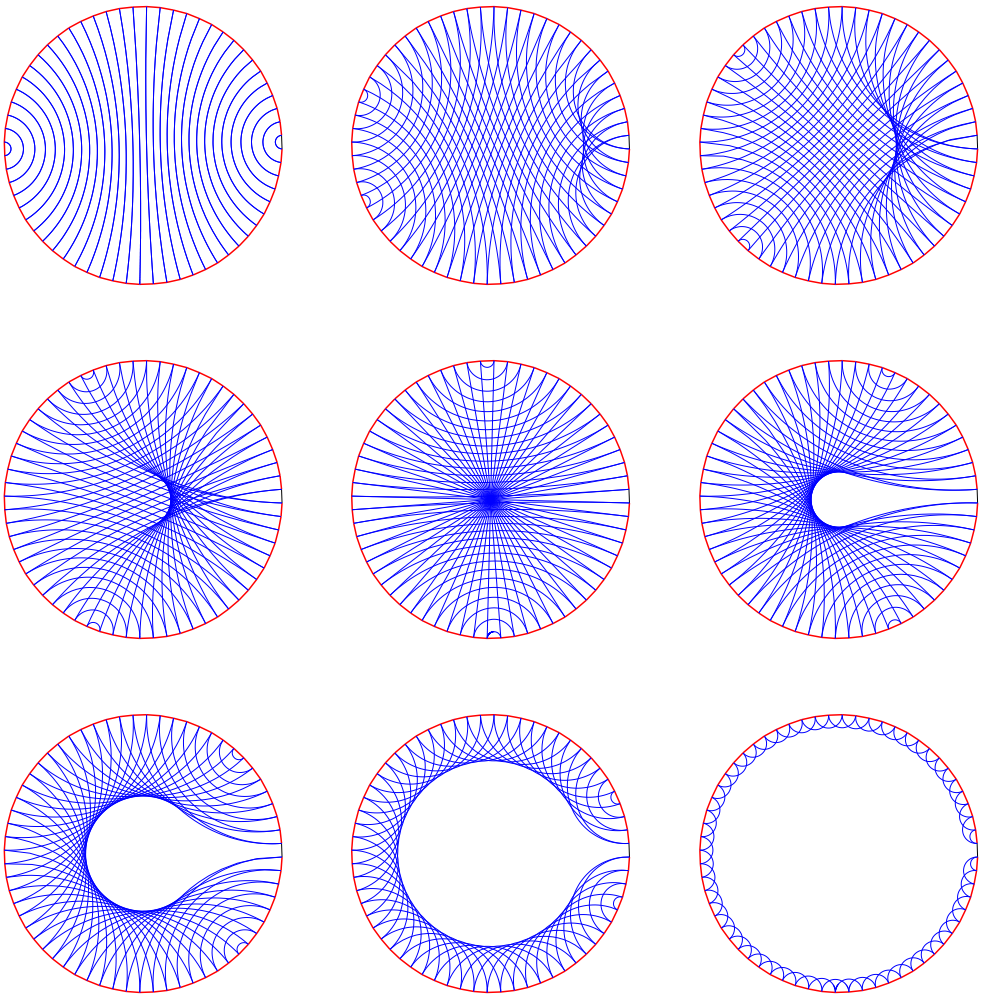

Figure 5.9: Different snapshots of the ballistic picture of the quench of the rainbow state with $L = 128$ sites by a homogeneous Hamiltonian with open boundaries (at the right extreme). Snapshots are taken with an interval of $\Delta T = 8$, from left to right and top to bottom. For time $T = 128$ the state is actually completely void of bonds, but we depict the case $T = 126$, where we can see a very local bond structure.

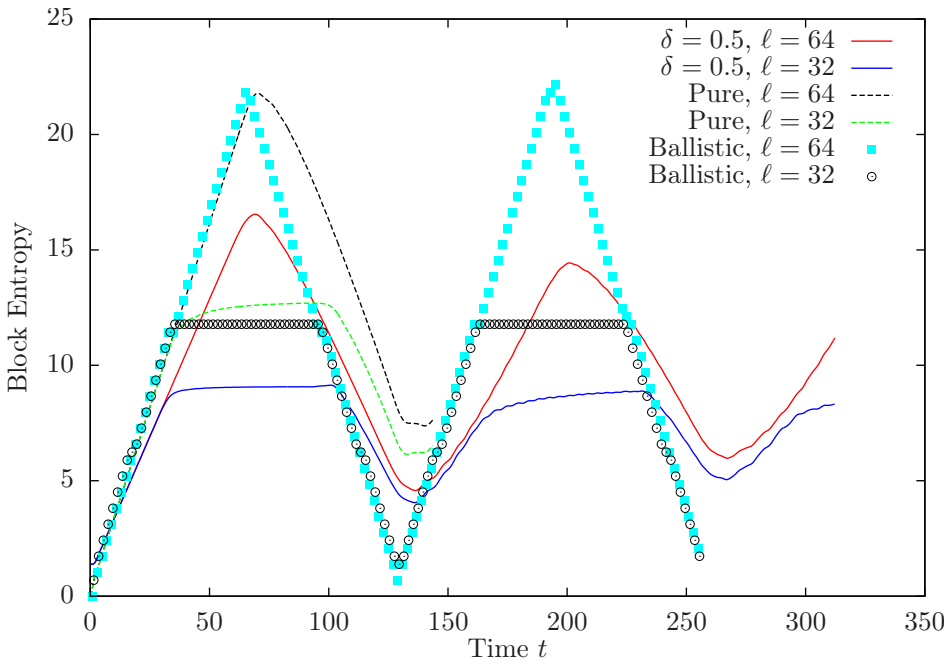


Figure 5.10: Comparison between the entanglement entropy of a system of $2L = 256$ sites obtained after the quench of a dimerized state, by exact diagonalization and the ballistic picture. The exact diagonalization is performed with the ground state of a dimerized Hamiltonian with $\delta = 0.5$ and with a *pure* dimerized state.

We shall consider the time evolution of a VBS under the free Hamiltonian with anti periodic boundary conditions (APBC)

$$H = -\frac{1}{2}\sum_{j=1}^{2L}\left(c_j^\dagger c_{j+1} + c_{j+1}^\dagger c_j\right), \tag{5.16}$$

where $c_{2L+1} = -c_1$. The choice of the boundary conditions is simply for later convenience. Let us consider the linear combination of fermionic operators $c_j$ with a well defined momentum

$$d_k = \frac{1}{\sqrt{2L}}\sum_{j=1}^{2L} e^{-ijk} c_j \ , \tag{5.17}$$

where the momentum $k \in \Lambda_L$ is chosen to be half-integers

$$\Lambda_L = \left\{ \frac{\pi m}{L} \middle| m = \pm\frac{1}{2}, \pm\frac{3}{2}, \ldots, \pm\left(L - \frac{1}{2}\right) \right\}, \tag{5.18}$$

in terms of these new operators, the Hamiltonian (5.16) transforms into

$$H = \sum_{k\in\Lambda_L} \varepsilon_k \, d_k^\dagger d_k \ , \tag{5.19}$$

which is diagonal in the momentum operators with eigenvalues $\varepsilon_k = -\cos(k)$.

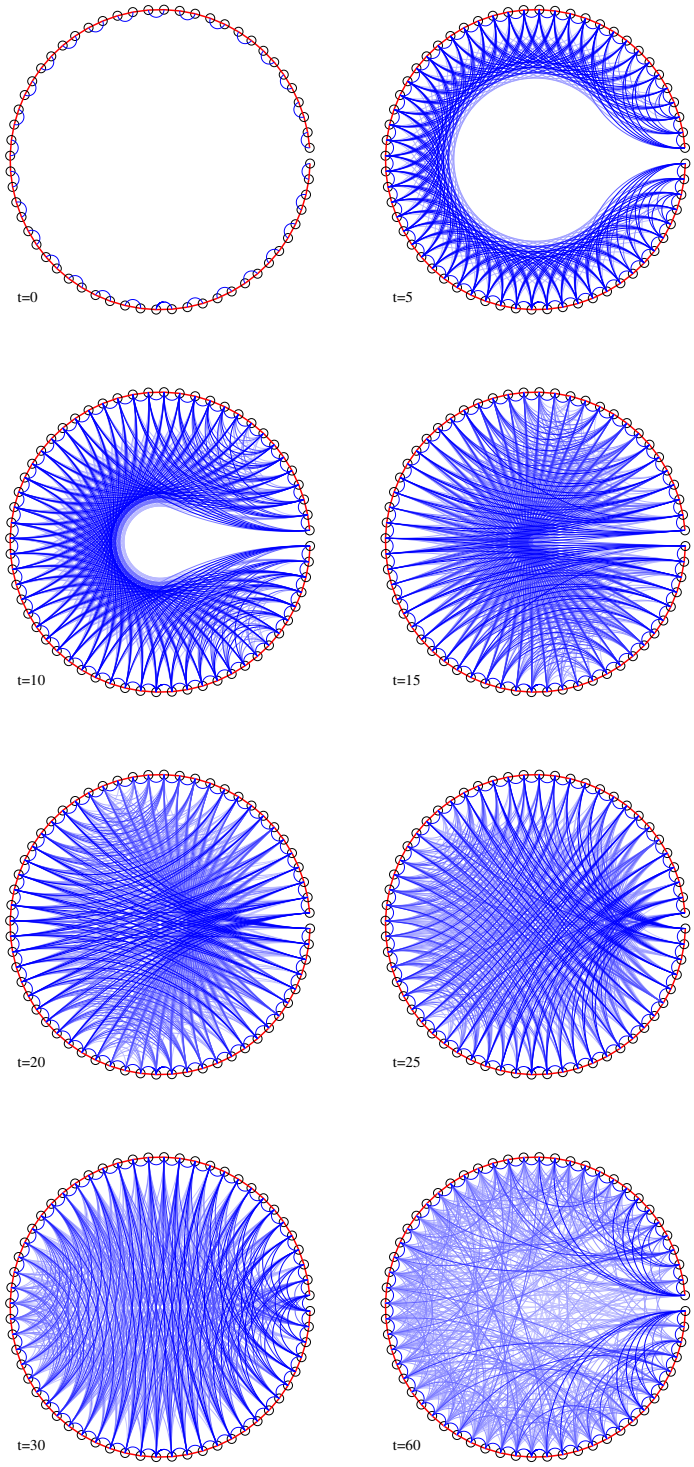


Figure 5.11: Time evolution of the correlator structure of the dimer state under a quench to a clean Hamiltonian. The size of the system is $2L = 60$. Each frame represents the correlation matrix $C_{ij}(t) = \langle \Psi(t)|c_i^\dagger c_j|\Psi(t)\rangle$ for different times, which appear close to each picture. Each line corresponds to an element of that matrix and the color intensity is related to $|C_{ij}(t)|$, removing the smallest near the precision machine for visualization reasons only. The last frame corresponds to the period.

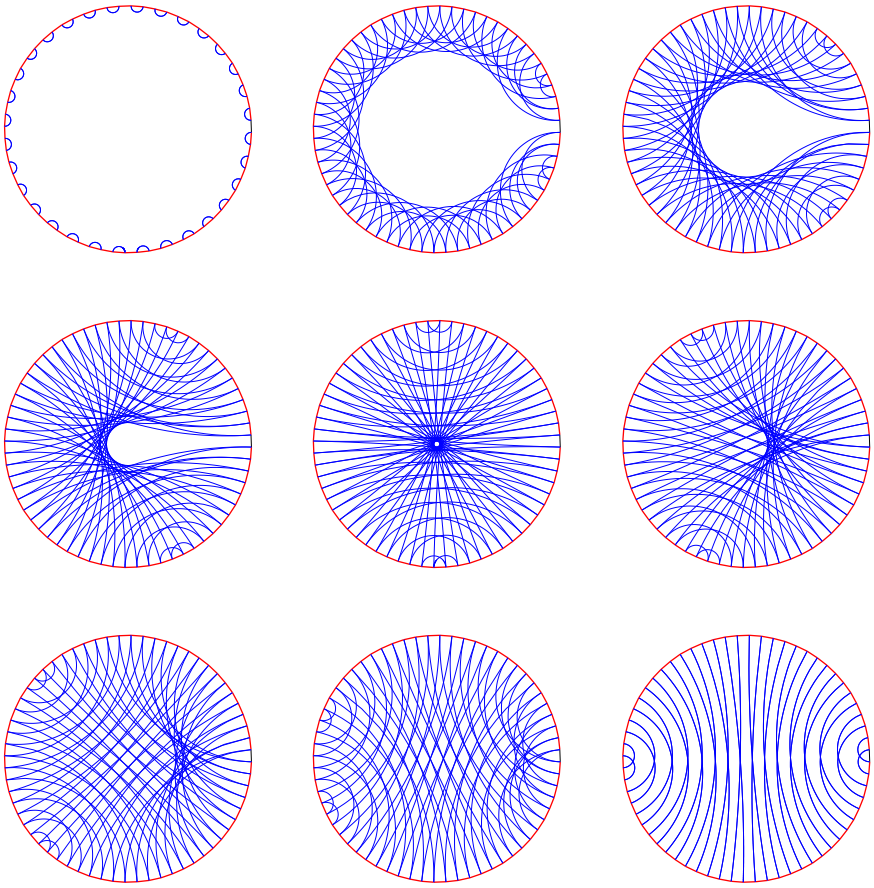

Figure 5.12: Time evolution of the bond structure of the dimerized state for a system of $2L = 60$, under the ballistic picture. Note that the last snapshot corresponds to one half of the period.

Thus, the time-dependent state is

$$|D(t)\rangle = e^{-itH}|D\rangle, \tag{5.20}$$

and we can obtain the two-point correlator using

$$C_{j,j'}(t) = \langle D|e^{itH}c_j^\dagger c_{j'}e^{-itH}|D\rangle = \langle D|c_j^\dagger(t)c_{j'}(t)|D\rangle, \tag{5.21}$$

where $c_j(t)$ is the fermion operator in the Heisenberg picture

$$c_j(t) = e^{itH}c_j\, e^{-itH} = \frac{1}{\sqrt{2L}}\sum_k e^{ijk}e^{-it\varepsilon_k}d_k = \frac{1}{\sqrt{2L}}\sum_{k,j'} e^{i(j-j')k}e^{-it\varepsilon_k}c_{j'}\ , \tag{5.22}$$

plugging this equation into equation (5.20) yields

$$C_{j,j'}(t) = \frac{1}{(2L)^2}\sum_{k,k',\ell,\ell'} e^{-i(j-\ell)k+i(j'-\ell')k'}\ e^{it(\varepsilon_k-\varepsilon_{k'})}\,C_{\ell,\ell'}\ , \tag{5.23}$$

and using the two-point correlator for the dimer state defined as

$$C_{j,j'} = \frac{1}{2}\begin{cases}\delta_{j',\sigma(j)}, & j\in A,\ j'\in B\\ \delta_{j,\sigma(j')}, & j\in B,\ j'\in A\\ 0 & \text{else}\end{cases} \tag{5.24}$$

where $A$ and $B$ are respectively the sets of odd and even sites and $\sigma(2j-1)=2j$ for $j=1,\ldots,L$. Thus, we obtain the time-dependent two-point correlator

$$C_{j,j'}(t) = \frac{1}{8L^2}\sum_{k,k'}\sum_{\ell\in A} e^{i(-jk+j'k')}\left[e^{i(\ell k-\sigma(\ell)k')}+e^{i(\sigma(\ell)k-\ell k')}\right]e^{it(\varepsilon_k-\varepsilon_{k'})}. \tag{5.25}$$

It is convenient to first carry out the sum over the lattice points $A$ defining the function

$$F_{k,k'} = \frac{1}{L}\sum_{\ell\in A}\left[e^{i(\ell k-\sigma(\ell)k')}+e^{i(-\ell k'+\sigma(\ell)k)}\right], \tag{5.26}$$

in terms of which

$$C_{j,j'}(t) = \frac{1}{8L}\sum_{k,k'} e^{i[-jk+j'k'+t(\varepsilon_k-\varepsilon_{k'})]}F_{k,k'}\ . \tag{5.27}$$

We shall call $F_{k,k'}$ the *form factor* of the dimer state because it characterizes the quench dynamics of the state. The form factor satisfy the property $F^*_{k,k'} = F_{k',k}$ and can be defined for any other VBS.

In the dimer case one finds the form factor

$$F_{k,k'} = (e^{-ik} + e^{ik'})(\delta_{k-k',0} + \delta_{k-k',\pi}), \tag{5.28}$$

which yields the correlator

$$C_{j,j'}(t) = \frac{(-1)^{j'}}{4}\left(\delta_{j,j'-1} - \delta_{j,j'+1}\right) + \frac{1}{8L}\sum_k \left[e^{i(-j+j'+1)k} + e^{i(-j+j'-1)k}\right] e^{2it\varepsilon_k}, \tag{5.29}$$

which satisfies

$$C_{j,j'}(t=0) = \frac{1}{2}\begin{cases}\delta_{j,j'-1} & j' \text{ even} \\ \delta_{j,j'+1} & j' \text{ odd}\end{cases} \tag{5.30}$$

in agreement with equation (5.24) for the dimer state. Observe that

$$\lim_{T\to\infty}\frac{1}{T}\int_0^T dt\, C_{j,j'}(t) = \frac{1}{4}\delta_{|j-j'|,1}\ , \tag{5.31}$$

which means that the time evolution does not erase completely the dimer correlations of the initial state. Moreover, notice also the time dependence $e^{2it\varepsilon_k}$ in equation (5.29), which follows from the relation $\varepsilon_{k+\pi} = -\varepsilon_k$.

Let us introduce an approximate version of equation (5.29) assuming that it only depends on the difference $x = j' - j$,

$$C(x,t) \equiv C_{j,j'}(t) = \frac{1}{4}\delta_{|x|,1} + \frac{1}{8L}\sum_k \left(e^{i(x+1)k} + e^{i(x-1)k}\right) e^{2it\varepsilon_k}, \tag{5.32}$$

and, from equation (5.17), we can make the continuum limit

$$\sum_k \to \frac{L}{\pi}\int_{-\pi}^{\pi} dk \tag{5.33}$$

and replace equation (5.32) by

$$C(x,t) \simeq \frac{1}{4\pi}\int_{-\pi}^{\pi} dk\ e^{i(kx+2t\varepsilon(k))}, \quad |x| \gg 1. \tag{5.34}$$

As a side comment, let us take $t = 0$ in this equation and replace the momentum $\pm\pi$ by $\pm\infty$,

$$C(x, t=0) \to \frac{1}{4\pi}\int_{-\infty}^{\infty} dk\ e^{ikx} = \frac{1}{2}\delta(x)$$

which is a continuous version of equation (5.30).

For large values of $x$ and $t$, the phase of the exponential in equation (5.34), $\mathcal{S}(k) =$

$kx - 2t\cos(k)$, oscillates strongly so the integral can be evaluated using the saddle point method. The first step is to find the momenta $k_n$ for which the phase $\mathcal{S}(k)$ is stationary

$$\mathcal{S}'(k) = x + 2t\sin k = 0 \implies \sin k_n = -\frac{x}{2t} \tag{5.35}$$

then one expands the phase up to second order around $k_n$,

$$\mathcal{S}(k) \simeq \mathcal{S}(k_n) + \frac{1}{2}(k-k_n)^2\mathcal{S}''(k_n), \tag{5.36}$$

where

$$\mathcal{S}''(k) = 2t\cos k \tag{5.37}$$

and integrate around all the saddle points, which yields the approximation

$$C(x,t) \sim \frac{1}{\sqrt{8\pi}} \sum_n |\mathcal{S}''(k_n)|^{-1/2}\ e^{i\mathcal{S}(k_n)+i\frac{\pi}{4}\mathrm{sign}(\mathcal{S}''(k_n))} \tag{5.38}$$

where we assume that momenta $k_n$ are such that $\mathcal{S}''(k_n)$ is real. The largest values of $C(x,t)$ occur if $|\mathcal{S}''(k_n)| \simeq 0$, which corresponds to $|k_n| \simeq \pi/2$ (see equation (5.37)) and therefore to $|x/2t| \simeq 1$ (see equation (5.35)) which is the reason of the apparent superluminal propagation. Thus, the four solutions of equation (5.35) in the vicinity of the two Fermi points,

$$k_{R,\pm} \simeq -\frac{\pi}{2} \pm \sqrt{2 - \frac{x}{t}}, \qquad x \lesssim 2t, \tag{5.39a}$$

$$k_{L,\pm} \simeq \frac{\pi}{2} \pm \sqrt{2 + \frac{x}{t}}, \qquad x \gtrsim -2t, \tag{5.39b}$$

where $k_{R,\pm}$ and $k_{L,\pm}$ correspond, respectively, to a right and left moving quasiparticles. Replacing these expressions into equation (5.38) provides the final result

$$C(x,t) \simeq \frac{1}{2\pi^{1/2}} \left[\frac{e^{-i\pi x/2}}{t^{1/4}(2t-x)^{1/4}}\right] \cos\left[t^{-1/2}(2t-x)^{3/2} - \pi/4\right], \quad x \lesssim 2t, \tag{5.40a}$$

$$C(x,t) \simeq \frac{1}{2\pi^{1/2}} \left[\frac{e^{i\pi x/2}}{t^{1/4}(2t+x)^{1/4}}\right] \cos\left[t^{-1/2}(2t+x)^{3/2} - \pi/4\right], \quad x \gtrsim -2t. \tag{5.40b}$$

For large times the oscillation factors are suppressed and these equations simplify

$$C(x,t) \to -\frac{1}{2^{3/2}\pi^{1/2}} \left[\frac{e^{-i\pi x/2}}{t^{1/4}(2t-x)^{1/4}}\right], \qquad t \gg 1,\ x \lesssim 2t \tag{5.41a}$$

$$C(x,t) \to -\frac{1}{2^{3/2}\pi^{1/2}} \left[\frac{e^{i\pi x/2}}{t^{1/4}(2t+x)^{1/4}}\right], \qquad t \gg 1,\ x \gtrsim -2t. \tag{5.41b}$$

These expressions are proportional to correlators of vertex operators of the form

$$\left\langle e^{i\varphi(x_R-t)/2}e^{-i\varphi(x_L+t)/2}\right\rangle = \frac{1}{(x_R-x_L-2t)^{1/4}} \tag{5.42}$$

where $\varphi(x \pm t)$ is a chiral massless boson field and $e^{\pm i\varphi(x)/2}$ is a vertex operator with conformal weight $h = 1/8$. The quasiparticles can then be described by the operators

$$R_\pm(x,t) \propto e^{\pm i\varphi(x-vt)/2}, \tag{5.43a}$$

$$L_\pm(x,t) \propto e^{\pm i\varphi(x+vt)/2}. \tag{5.43b}$$

At $t = 0$ an entangled pair of quasiparticles is created, that is $L_+(x)R_-(x+\epsilon) + L_-(x)R_+(x+\epsilon)$, where $\varepsilon$ is the lattice spacing, and then the particles propagate to the left and right.

Let us recall that the free fermion model is described by a compactified free boson with radius $R = 1$, and whose chiral primary fields are given by the vertex operators $e^{ip\varphi(x)}$, with $p = n + \frac{1}{2}m$ for $n, m \in \mathbb{Z}$ and conformal weight $h = \frac{1}{2}p^2$. Hence the fields $e^{\pm i\varphi(x)/2}$ belong to this set. The other primary field in the theory is the Dirac fermion $e^{\pm i\varphi}$. We have found that the quasiparticles postulated by Calabrese and Cardy (2005) are described by the fields $e^{\pm i\varphi(x)/2}$.

## 5.6 Quenching a Dimer State on a Rindler Space-time

In this section we investigate the behavior of a dimer state after a quench to a homogeneous Hamiltonian in a different space-time. As discussed by Boada *et al.* (2011), simulation of a quantum field theory on some kinds of space-times can amount to a clever choice of the hopping rates between neighboring sites. Indeed, Rindler space-time, i.e., the space-time viewed by an observer undergoing uniform acceleration when traveling through Minkowski space-time, can fit in that scheme. The metric is given by (in 1D)

$$ds^2 = -x^2dt^2 + dx^2. \tag{5.44}$$

In that case, we can model the spinless Dirac equation with the following Hamiltonian

$$H = -\sum_{i=1}^{L} \frac{J_0}{2}\left(\frac{i}{L}\right) c_i^\dagger c_{i+1} + \text{h.c.} \tag{5.45}$$

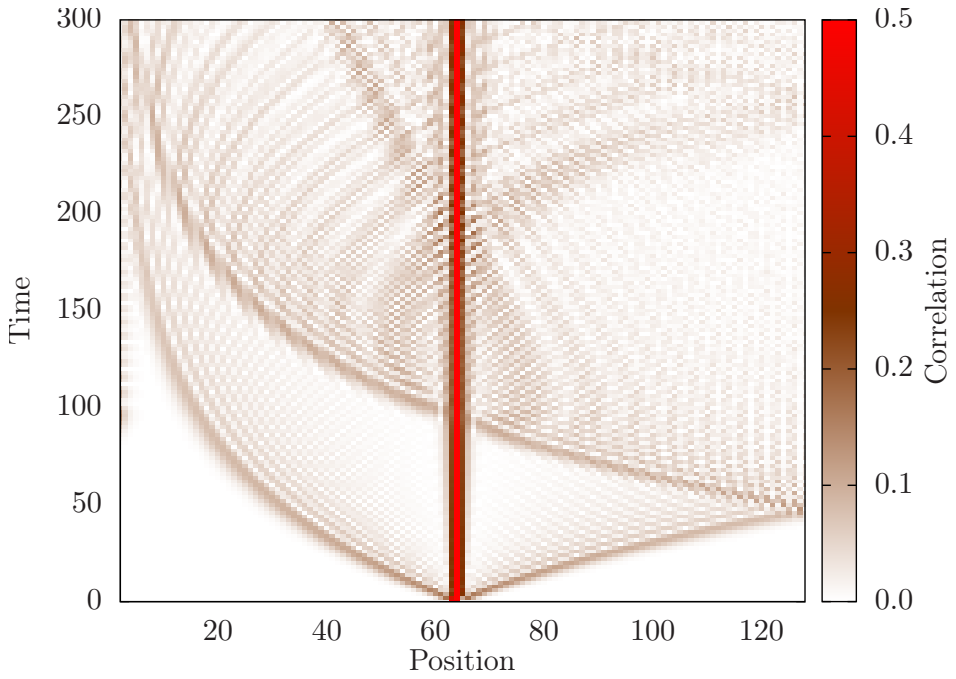


Figure 5.13: Space-time diagram of the correlation function between a site at the center of the chain and all others. Notice the perturbation how it travels leftwards and rightwards with a curvature, given by the acceleration. Notice also that the perturbation never reaches the horizon at the left, but approaches it asymptotically.

This space-time is characterized by the presence of an event horizon at $x = 0$, which for us corresponds to the left extreme. In figure 5.13 we can see the evolution of the correlator between the site at the middle of the chain with all others, as a function of time. Notice that the correlator with itself is just the density, and it is always 1/2. The correlator propagates to the left and to the right with different speeds. Leftwards, we can recognize a curvature, due to the fact that it approaches an horizon. Notice that the particles never reach exactly the horizon, it is only approached asymptotically. On the other hand, the correlator propagates rightwards with acceleration, and is reflected back at the boundary.

We have also applied the ballistic picture to this model. The only difference is that the speed of the virtual particles becomes position-dependent. This way we were able to make the following predictions, which are fulfilled. Figure 5.14 shows how, for exact diagonalization (left panel), we obtain that the block entropy for different blocks does not grow with the same speed. All blocks are considered to contain the horizon. Those which are small contain only sites for which the propagation of information is very slow, so the entropy grows only slowly. This dispersion of velocities is predicted very accurately by the ballistic model.

Figure 5.15 gives a further step and shows the time evolution of the exact bond structure. Notice that bonds propagate with different velocities at different points on the lattice. Bonds at the horizon remain unaltered.

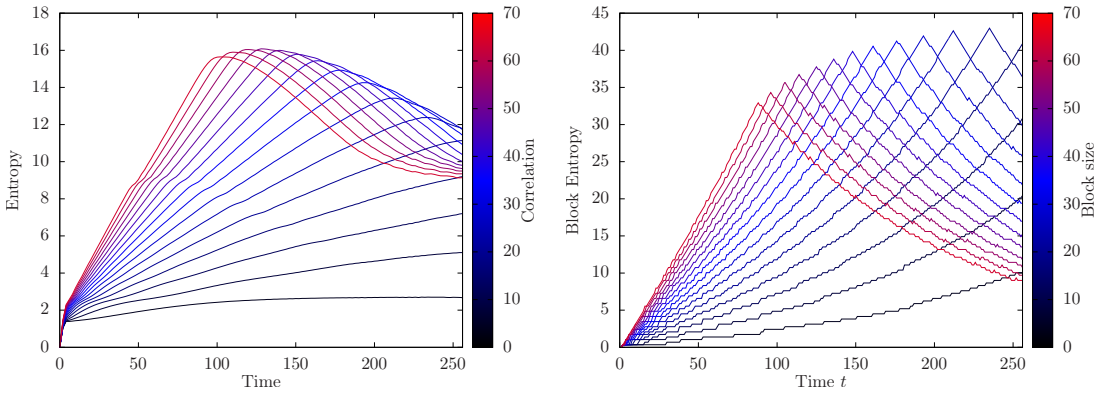


Figure 5.14: Comparison between the entropies computed by the ballistic picture and exact diagonalization for the quench of a dimerized state on a Rindler metric.

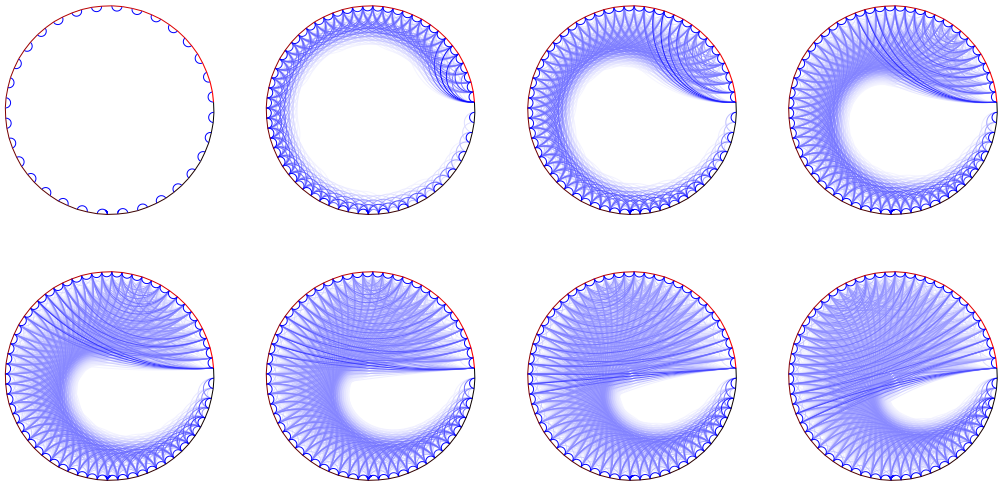

Figure 5.15: Bond structure evolution of the dimer state after the quench to a Rindler metric.

# Chapter 6

# Conclusions and Future work

## Random Systems

We discussed a fermionic system with random hoppings. Those systems have been studied from different perspectives and they have been found as a rich source of problems and surprises. The case of 1D systems with strong off-diagonal disorder is known to present logarithmic violations of the area law, although they are not. The logarithmic corrections are parametrized with an *effective* central charge related to the conformal field theory (CFT) associated to the clean system. We analyzed the properties of entanglement in random hopping models, focusing on the similarities between the CFT predictions for the clean case and the strong disorder renormalization group (RG) predictions.

1. All the entanglement properties within the ground state stem from the probability distribution for the bond lengths and an assumption of approximate independence for large bond lengths. Both the thermodynamic limit and the finite-size form for the average von Neumann entropy can be deduced from the scaling analysis of that distribution function.

2. The behavior of the Rényi entropies can not be established solely from the bond picture, since the strong disorder renormalization group (SDRG) predicts the collapse of all Rényi orders. Indeed, we have observed that the parity oscillations which appear in the clean case according to the CFT prediction, attenuate as the disorder grows, making them similar for all values of the Rényi order.

3. Parity oscillations appear both in the average von Neumann entropy of chains with open boundary conditions and in the *variance* of the von Neumann entropy in all cases. They fit nicely an expression similar to the CFT prediction, but with different constants. Remarkably, the scaling of the maximal variance is again logarithmic, but with a different prefactor. Moreover, in the case of chains with

an odd number of sites, a *plateau* appears in the average von Neumann entropy, for intermediate system sizes.

4. We have introduced the *random permutation picture*, that is a simplification of the SDRG method, in which the hoppings are given fixed values which differ broadly in order of magnitude, but are distributed at random among the lattice links. All the properties of entanglement and correlation in the ground state can be established solely in this picture.

5. We have analyzed the average entanglement of excited states. Indeed, excited states are of two types: those which convert a negative energy mode into its corresponding positive energy mode do not alter the bond picture. However, excitations which add or remove particles alter them in a remarkable way. Indeed, the average entanglement entropy of the first excitation presents a *plateau* at intermediate sizes, whose magnitude scales logarithmically with the size of the system *as if* it corresponds to the average size of the maximal bond. Higher excitations result in a further reduction of the effective size of the system.

## Inhomogeneous Systems

We engineered an inhomogeneous 1D fermionic system, in order to obtain a maximal growth of the block entropy in the ground state, that we have called *the rainbow state*. In it, sites symmetrically placed with respect to the center are maximally entangled. We have studied the full deformation of critical local 1D Hamiltonians towards the rainbow state, which interpolates between a logarithmic law for the growth of the entanglement entropy and a volume law.

6. There is a smooth crossover between the uniform and the rainbow states that we have studied in detail for the XX model (free spinless fermions model) and shown to be qualitatively equivalent in the Heisenberg model.

7. The entanglement spectrum (ES) is approximately equally spaced, with an entanglement spacing that decays with the system size as $1/\log(L)$ at the conformal point and as $1/L$ outside this point. Furthermore, we have also found that the entanglement entropy is approximately proportional to the inverse of the entanglement spacing, in wide regions of the parameter space, which generalizes previous known results in critical and massive systems.

8. In the vicinity of the conformal model, the ground state can be described by the union of two exponential maps associated to each half of the chain. This transformation further suggests the definition of a temperature that is proportional to the parameter controlling the decay of the hopping. We show how this

deformation accounts for the change in the dispersion relation, the single-particle wavefunctions in the vicinity of the Fermi point, and the half-chain von Neumann and Rényi entropies.

9. The appearance of a volume law entropy is linked to the existence of an effective temperature for the ground state (GS) that is finally identified with a thermo field state. This striking result points towards an unexpected connection with the theory of black holes and the emergence of space-time from entanglement.

## Quenched Dynamics

We studied the time-evolution of some valence bond state (VBS) after a global quench to a homogeneous Hamiltonian in 1D. We focused on the evolution of the entanglement in the rainbow and dimer states. We proposed a generalization of the quasiparticle picture, which we have called the *ballistic picture*.

10. The entanglement of the half-chain of the rainbow state decreases linearly with time and, after it reaches a minimal value, it increases again, eventually reaching (approximately) the initial state. The dimer state, on the other hand presents an approximately opposite behaviour: the entanglement grows linearly for all blocks, reaching a maximally entangled state which resembles the rainbow state.

11. The ballistic picture seems to explain the linear growth of the entanglement of the rainbow and dimer states after a quench to a homogeneous Hamiltonian in terms of quasiparticles moving at the Fermi velocity through the system and the bonds established between the quasiparticles. This picture is also valuable to explain the time-evolution of the dimer state in Rindler space-time.

## Furture work

There are still many open questions related to the XX random system. First of all, a thorough analysis of entanglement for intermediate values of the disorder would clarify the decay of the oscillations and convergence of the Rényi entropies. Moreover, it would be interesting to study the system from a dynamical point of view, i.e. the clean to disorder transition. Since this transition can be regarded as a RG-flow, one may ask whether it will follow some generalization of the $c$-theorem of Zamolodchikov, appropriate for disorder averaged systems.

More open questions refer to the generality of our results regarding excited states for interacting models such as the Heisenberg model. Here we conjecture that the ground state of the system with one more particle (i.e. the triplet ground state) will have the

same entropy structure, but with the weakest bond removed. Thus, it will suffer the same effective length contraction as in our model.

In the inhomogeneous system, we have shown that an exponential deformation of the XX and Heisenberg models offers the possibility to analyze the departure from the logarithmic law of the entanglement entropy in CFT towards a volume law that is related to the valence bond picture of these models. It would be worth to study other critical models to verify the generality of these results, as well as non critical models that will exhibit a crossover from the area to the volume law.

The results of the aforementioned engineer motivate the use similar ideas to obtain different VBS. It is relevant to ask which bond structures can be obtained as GS of these inhomogeneous hopping Hamiltonians. The SDRG algorithm tells us that the only constraint is that the bonds *may never cut*.

# Bibliography

Affleck, I., T. Kennedy, E. H. Lieb, and H. Tasaki (1987), "Rigorous results on valence-bond ground states in antiferromagnets," Physical Review Letters **59** (7), 799.

Affleck, I., T. Kennedy, E. H. Lieb, and H. Tasaki (1988), "Valence bond ground states in isotropic quantum antiferromagnets," Communications in Mathematical Physics **115** (3), 477.

Affleck, I., and A. W. W. Ludwig (1991), "Universal noninteger "ground-state degeneracy" in critical quantum systems," Physical Review Letters **67**, 161.

Affleck, I., and A. W. W. Ludwig (1993), "Exact conformal-field-theory results on the multichannel Kondo effect: Single-fermion Green's function, self-energy, and resistivity," Physical Review B **48**, 7297.

Alcaraz, F. C., M. I. Berganza, and G. Sierra (2011), "Entanglement of Low-Energy Excitations in Conformal Field Theory," Physical Review Letters **106**, 201601.

Amico, L., R. Fazio, A. Osterloh, and V. Vedral (2008), "Entanglement in many-body systems," Reviews of Modern Physics **80**, 517.

Anderson, P. W. (1958), "Absence of Diffusion in Certain Random Lattices," Physical Review **109**, 1492.

Ashcroft, N., and N. Mermin (1976), *Solid State Physics* (Harcourt College Publishers).

Aspect, A., J. Dalibard, and G. Roger (1982a), "Experimental Test of Bell's Inequalities Using Time- Varying Analyzers," Physical Review Letters **49**, 1804.

Aspect, A., P. Grangier, and G. Roger (1981), "Experimental Tests of Realistic Local Theories via Bell's Theorem," Physical Review Letters **47**, 460.

Aspect, A., P. Grangier, and G. Roger (1982b), "Experimental Realization of Einstein-Podolsky-Rosen-Bohm *Gedankenexperiment* : A New Violation of Bell's Inequalities," Physical Review Letters **49**, 91.

Bardeen, J., L. N. Cooper, and J. R. Schrieffer (1957a), "Microscopic Theory of Superconductivity," Physical Review **106**, 162.

Bardeen, J., L. N. Cooper, and J. R. Schrieffer (1957b), "Theory of Superconductivity," Physical Review **108**, 1175.

Baxter, R. J. (1981), "Corner transfer matrices," Physica A: Statistical Mechanics and its Applications **106** (1–2), 18.

Bekenstein, J. D. (1973), "Black Holes and Entropy," Physical Review D **7**, 2333.

Bell, J. S. (1964), "On the Einstein Podolsky Rosen paradox," Physics **1** (3), 195.

Bell, J. S. (1966), "On the Problem of Hidden Variables in Quantum Mechanics," Reviews of Modern Physics **38**, 447.

Bell, J. S. (1981), "Bertlmann's socks and the nature of reality," Le Journal de Physique Colloques **42** (C2), C2 41.

Bethe, H. (1931), "Zur Theorie der Metalle," Zeitschrift für Physik **71** (3-4), 205.

Bloch, I., J. Dalibard, and W. Zwerger (2008), "Many-body physics with ultracold gases," Reviews of Modern Physics **80**, 885.

Boada, O., A. Celi, J. I. Latorre, and M. Lewenstein (2011), "Dirac equation for cold atoms in artificial curved spacetimes," New Journal of Physics **13** (3), 035002.

Bohm, D. (1952a), "A Suggested Interpretation of the Quantum Theory in Terms of "Hidden" Variables. I," Physical Review **85**, 166.

Bohm, D. (1952b), "A Suggested Interpretation of the Quantum Theory in Terms of "Hidden" Variables. II," Physical Review **85**, 180.

Bohm, D., and Y. Aharonov (1957), "Discussion of Experimental Proof for the Paradox of Einstein, Rosen, and Podolsky," Physical Review **108**, 1070.

Bohr, N. (1935), "Can Quantum-Mechanical Description of Physical Reality be Considered Complete?" Physical Review **48**, 696.

Bombelli, L., R. K. Koul, J. Lee, and R. D. Sorkin (1986), "Quantum source of entropy for black holes," Physical Review D **34**, 373.

Calabrese, P., M. Campostrini, F. Essler, and B. Nienhuis (2010), "Parity Effects in the Scaling of Block Entanglement in Gapless Spin Chains," Physical Review Letters **104**, 095701.

Calabrese, P., and J. Cardy (2004), "Entanglement entropy and quantum field theory," Journal of Statistical Mechanics: Theory and Experiment **2004** (06), P06002.

Calabrese, P., and J. Cardy (2005), "Evolution of entanglement entropy in one-dimensional systems," Journal of Statistical Mechanics: Theory and Experiment **2005** (04), P04010.

Calabrese, P., and J. Cardy (2006), "Time Dependence of Correlation Functions Following a Quantum Quench," Physical Review Letters **96**, 136801.

Calabrese, P., and J. Cardy (2007), "Entanglement and correlation functions following a local quench: a conformal field theory approach," Journal of Statistical Mechanics: Theory and Experiment **2007** (10), P10004.

Calabrese, P., and J. Cardy (2009), "Entanglement entropy and conformal field theory," Journal of Physics A: Mathematical and Theoretical **42** (50), 504005.

Calabrese, P., and F. H. L. Essler (2010), "Universal corrections to scaling for block entanglement in spin-1/2 XX chains," Journal of Statistical Mechanics: Theory and Experiment **2010** (08), P08029.

Cardy, J. (1996), *Scaling and Renormalization in Statistical Physics*, Cambridge Lecture Notes in Physics (Cambridge University Press).

Cardy, J. L., and I. Peschel (1988), "Finite-size dependence of the free energy in two-dimensional critical systems," Nuclear Physics B **300**, 377.

Chen, Y., and G. Vidal (2014), "Entanglement contour," Journal of Statistical Mechanics: Theory and Experiment **2014** (10), P10011.

Cirac, J. I., and F. Verstraete (2009), "Renormalization and tensor product states in spin chains and lattices," Journal of Physics A: Mathematical and Theoretical **42** (50), 504004.

Clauser, J. F., M. A. Horne, A. Shimony, and R. A. Holt (1969), "Proposed Experiment to Test Local Hidden-Variable Theories," Physical Review Letters **23**, 880.

Daley, A. J., C. Kollath, U. Schollwöck, and G. Vidal (2004), "Time-dependent density-matrix renormalization-group using adaptive effective Hilbert spaces," Journal of Statistical Mechanics: Theory and Experiment **2004** (04), P04005.

Daley, A. J., H. Pichler, J. Schachenmayer, and P. Zoller (2012), "Measuring Entanglement Growth in Quench Dynamics of Bosons in an Optical Lattice," Physical Review Letters **109**, 020505.

Dalmonte, M., E. Ercolessi, and L. Taddia (2011), "Estimating quasi-long-range order via Rényi entropies," Physical Review B **84**, 085110.

Dalmonte, M., E. Ercolessi, and L. Taddia (2012), "Critical properties and Rényi entropies of the spin-$\frac{3}{2}$ $XXZ$ chain," Physical Review B **85**, 165112.

Dasgupta, C., and S.-k. Ma (1980), "Low-temperature properties of the random Heisenberg antiferromagnetic chain," Physical Review B **22** (3), 1305.

David, F., C. Hagendorf, and K. J. Wiese (2008), "A growth model for RNA secondary structures," Journal of Statistical Mechanics: Theory and Experiment **2008** (04), P04008.

Di Francesco, P., P. Mathieu, and D. Senechal (1997), *Conformal Field Theory*, Graduate Texts in Contemporary Physics (Springer).

Dukelsky, J., M. A. Martín-Delgado, T. Nishino, and G. Sierra (1998), "Equivalence of the variational matrix product method and the density matrix renormalization group applied to spin chains," Europhysics Letters **43** (4), 457.

Einstein, A., B. Podolsky, and N. Rosen (1935), "Can Quantum-Mechanical Description of Physical Reality Be Considered Complete?" Physical Review **47**, 777.

Eisert, J., M. Cramer, and M. B. Plenio (2010), "Colloquium: Area laws for the entanglement entropy," Reviews of Modern Physics **82**, 277.

Eisler, V., D. Karevski, T. Platini, and I. Peschel (2008), "Entanglement evolution after connecting finite to infinite quantum chains," Journal of Statistical Mechanics: Theory and Experiment **2008** (01), P01023.

Eisler, V., and I. Peschel (2013), "Free-fermion entanglement and spheroidal functions," Journal of Statistical Mechanics: Theory and Experiment **2013** (04), P04028.

Eloy, D., and J. C. Xavier (2012), "Entanglement entropy of the low-lying excited states and critical properties of an exactly solvable two-leg spin ladder with three-spin interactions," Physical Review B **86**, 064421.

Essler, F. H. L., A. M. Läuchli, and P. Calabrese (2013), "Shell-Filling Effect in the Entanglement Entropies of Spinful Fermions," Physical Review Letters **110**, 115701.

Fagotti, M., and P. Calabrese (2011), "Universal parity effects in the entanglement entropy of XX chains with open boundary conditions," Journal of Statistical Mechanics: Theory and Experiment **2011** (01), P01017.

Fagotti, M., P. Calabrese, and J. E. Moore (2011), "Entanglement spectrum of random-singlet quantum critical points," Physical Review B **83**, 045110.

Fannes, M., B. Nachtergaele, and R. Werner (1992), "Finitely correlated states on quantum spin chains," Communications in Mathematical Physics **144** (3), 443.

Fisher, D. (1995), "Critical behavior of random transverse-field Ising spin chains," Physical Review B **51** (10), 6411.

Fisher, D., and A. Young (1998), "Distributions of gaps and end-to-end correlations in random transverse-field Ising spin chains," Physical Review B **58** (14), 9131.

Fisher, D. S. (1994), "Random antiferromagnetic quantum spin chains," Physical Review B **50**, 3799.

Freedman, S. J., and J. F. Clauser (1972), "Experimental Test of Local Hidden-Variable Theories," Physical Review Letters **28**, 938.

Friedan, D., and A. Konechny (2004), "Boundary Entropy of One-Dimensional Quantum Systems at Low Temperature," Physical Review Letters **93**, 030402.

Fu, L., and C. L. Kane (2007), "Topological insulators with inversion symmetry," Physical Review B **76**, 045302.

Gioev, D., and I. Klich (2006), "Entanglement Entropy of Fermions in Any Dimension and the Widom Conjecture," Physisical Review Letters **96**, 100503.

Goldsborough, A. M., and R. A. Römer (2014), "Self-assembling tensor networks and holography in disordered spin chains," Physical Review B **89**, 214203.

Gómez, C., M. Ruiz-Altaba, and G. Sierra (1996), *Quantum Groups in Two-Dimensional Physics*, Cambridge Lecture Notes in Physics (Cambridge University Press).

Gori, G., S. Paganelli, A. Sharma, P. Sodano, and A. Trombettoni (2014), "Bell-Paired States Inducing Volume Law for Entanglement Entropy in Fermionic Lattices," arXiv e-prints arXiv:1405.3616 [cond-mat.stat-mech].

Green, D., M. Mulligan, and D. Starr (2008), "Boundary entropy can increase under bulk RG flow," Nuclear Physics B **798** (3), 491.

Haldane, F. (1983), "Continuum dynamics of the 1-D Heisenberg antiferromagnet: Identification with the O(3) nonlinear sigma model," Physics Letters A **93** (9), 464.

Hartman, T., and J. Maldacena (2013), "Time evolution of entanglement entropy from black hole interiors," Journal of High Energy Physics **2013** (5), 14, 10.1007/JHEP05(2013)014.

Hastings, M. B. (2007), "An area law for one-dimensional quantum systems," Journal of Statistical Mechanics: Theory and Experiment **2007** (08), P08024.

Hawking, S. (1975), "Particle creation by black holes," Communications in Mathematical Physics **43** (3), 199.

Heisenberg, W. (1928), "Zur Theorie des Ferromagnetismus," Zeitschrift für Physik **49** (9-10), 619.

Hohenberg, P., and W. Kohn (1964), "Inhomogeneous Electron Gas," Physical Review **136**, B864.

Holzhey, C., F. Larsen, and F. Wilczek (1994), "Geometric and renormalized entropy in conformal field theory," Nuclear Physics B **424** (3), 443.

Horodecki, R., P. Horodecki, M. Horodecki, and K. Horodecki (2009), "Quantum entanglement," Reviews of Modern Physics **81**, 865.

Hoyos, J. A., A. P. Vieira, N. Laflorencie, and E. Miranda (2007), "Correlation amplitude and entanglement entropy in random spin chains," Physical Review B **76**, 174425.

Huijse, L., and B. Swingle (2013), "Area law violations in a supersymmetric model," Physical Review B **87**, 035108.

Ibáñez Berganza, M., F. Castilho Alcaraz, and G. Sierra (2012), "Entanglement of excited states in critical spin chains," Journal of Statistical Mechanics: Theory and Experiment **2012** (01), P01016.

Jia, X., A. R. Subramaniam, I. A. Gruzberg, and S. Chakravarty (2008), "Entanglement entropy and multifractality at localization transitions," Physical Review B **77**, 014208.

Jordan, P., and E. Wigner (1928), "Über das Paulische Äquivalenzverbot," Zeitschrift für Physik **47** (9-10), 631.

Klümper, A., A. Schadschneider, and J. Zittartz (1993), "Matrix Product Ground States for One-Dimensional Spin-1 Quantum Antiferromagnets," Europhysics Letters **24** (4), 293.

Kohn, W., and L. J. Sham (1965), "Self-Consistent Equations Including Exchange and Correlation Effects," Physical Review **140**, A1133.

Kriecherbauer, T., and J. Krug (2010), "A pedestrian's view on interacting particle systems, KPZ universality and random matrices," Journal of Physics A: Mathematical and Theoretical **43** (40), 403001.

Laflorencie, N. (2005), "Scaling of entanglement entropy in the random singlet phase," Physical Review B **72**, 140408.

Laflorencie, N., E. S. Sørensen, M.-S. Chang, and I. Affleck (2006), "Boundary Effects in the Critical Scaling of Entanglement Entropy in 1D Systems," Physical Review Letters **96**, 100603.

Lange, C., A. Klümper, and J. Zittartz (1994), "Exact groundstates for antiferromagnetic spin-one chains with nearest and next-nearest neighbour interactions," Zeitschrift für Physik B Condensed Matter **96** (2), 267.

Läuchli, A. M. (2013), "Operator content of real-space entanglement spectra at conformal critical points," arXiv e-prints arXiv:1303.0741 [cond-mat.stat-mech].

Laughlin, R. B. (1981), "Quantized Hall conductivity in two dimensions," Physical Review B **23**, 5632.

Lepori, L., G. De Chiara, and A. Sanpera (2013), "Scaling of the entanglement spectrum near quantum phase transitions," Physical Review B **87**, 235107.

Lewenstein, M., A. Sanpera, and V. Ahufinger (2012), *Ultracold Atoms in Optical Lattices: Simulating quantum many-body systems* (Oxford University Press).

Lewenstein, M., A. Sanpera, V. Ahufinger, B. Damski, A. Sen(De), and U. Sen (2007), "Ultracold atomic gases in optical lattices: mimicking condensed matter physics and beyond," Advances in Physics **56** (2), 243.

Li, H., and F. D. M. Haldane (2008), "Entanglement Spectrum as a Generalization of Entanglement Entropy: Identification of Topological Order in Non-Abelian Fractional Quantum Hall Effect States," Physical Review Letters **101**, 010504.

Lieb, E. H., and D. W. Robinson (1972), "The finite group velocity of quantum spin systems," Communications in Mathematical Physics **28** (3), 251.

Ma, X.-S., T. Herbst, T. Scheidl, D. Wang, S. Kropatschek, W. Naylor, B. Wittmann, A. Mech, J. Kofler, E. Anisimova, V. Makarov, T. Jennewein, R. Ursin, and A. Zeilinger (2012), "Quantum teleportation over 143 kilometres using active feed-forward," Nature **489** (7415), 269.

Maldacena, J. (1999), "The Large-N Limit of Superconformal Field Theories and Supergravity," International Journal of Theoretical Physics **38** (4), 1113.

Maldacena, J., and L. Susskind (2013), "Cool horizons for entangled black holes," Fortschritte der Physik **61** (9), 781.

Müller, M. (2003), *Repliement d'hétéropolymères*, Ph.D. thesis (University Paris XI, Orsay), thèse de doctorat dirigée par Mèzard, M.

von Neumann, J. (1932), *Mathematische Grundlagen der Quantenmechanik* (Springer) [See von Neumann, 1955].

von Neumann, J. (1955), *Mathematical Foundations of Quantum Mechanics*, Investigations in physics (Princeton University Press).

Nielsen, M. A., and I. L. Chuang (2010), *Quantum Computation and Quantum Information: 10th Anniversary Edition*, 10th ed. (Cambridge University Press).

Okunishi, K. (2005), "Real-Space Renormalization Group Approach for the Corner Hamiltonian," Journal of the Physical Society of Japan **74** (12), 3186.

Okunishi, K., and T. Nishino (2010), "Scale-free property and edge state of Wilson's numerical renormalization group," Physical Review B **82**, 144409.

Östlund, S., and S. Rommer (1995), "Thermodynamic Limit of Density Matrix Renormalization," Physical Review Letters **75**, 3537.

Peschel, I. (2003), "Calculation of reduced density matrices from correlation functions," Journal of Physics A: Mathematical and General **36** (14), L205.

Peschel, I. (2004), "On the reduced density matrix for a chain of free electrons," Journal of Statistical Mechanics: Theory and Experiment **2004** (06), P06004.

Peschel, I., and T. Truong (1987), "Corner transfer matrices and conformal invariance," Zeitschrift für Physik B Condensed Matter **69** (2-3), 385.

Polkovnikov, A., K. Sengupta, A. Silva, and M. Vengalattore (2011), "Colloquium: Nonequilibrium dynamics of closed interacting quantum systems," Reviews of Modern Physics **83**, 863.

Qi, X.-L., H. Katsura, and A. W. W. Ludwig (2012), "General Relationship between the Entanglement Spectrum and the Edge State Spectrum of Topological Quantum States," Physical Review Letters **108**, 196402.

Ramírez, G., J. Rodríguez-Laguna, and G. Sierra (2014a), "Entanglement in low-energy states of the random-hopping model," Journal of Statistical Mechanics: Theory and Experiment **2014** (7), P07003.

Ramírez, G., J. Rodríguez-Laguna, and G. Sierra (2014b), "From conformal to volume law for the entanglement entropy in exponentially deformed critical spin 1/2 chains," Journal of Statistical Mechanics: Theory and Experiment **2014** (10), P10004.

Ramírez, G., J. Rodríguez-Laguna, and G. Sierra (2015), "Entanglement over the rainbow," arXiv e-prints arXiv:1503.02695 [quant-ph].

Refael, G., and J. E. Moore (2004), "Entanglement Entropy of Random Quantum Critical Points in One Dimension," Physical Review Letters **93**, 260602.

Refael, G., and J. E. Moore (2009), "Criticality and entanglement in random quantum systems," Journal of Physics A: Mathematical and Theoretical **42** (50), 504010.

Rodríguez-Laguna, J. (2002), *Real Space Renormalization Group Techniques and Applications*, Ph.D. thesis (Universidad Complutense de Madrid), thesis supervised by Martín-Delgado, M. A. and G. Sierra.

Rodríguez-Laguna, J., P. Migdał, M. I. Berganza, M. Lewenstein, and G. Sierra (2012), "Qubism: self-similar visualization of many-body wavefunctions," New Journal of Physics **14** (5), 053028.

Rowe, M. A., D. Kielpinski, V. Meyer, C. A. Sackett, W. M. Itano, C. Monroe, and D. J. Wineland (2001), "Experimental violation of a Bell's inequality with efficient detection," Nature **409** (6822), 791.

Ryu, S., and T. Takayanagi (2006), "Holographic Derivation of Entanglement Entropy from the anti-de Sitter Space/Conformal Field Theory Correspondence," Physical Review Letters **96**, 181602.

Schachenmayer, J., B. P. Lanyon, C. F. Roos, and A. J. Daley (2013), "Entanglement Growth in Quench Dynamics with Variable Range Interactions," Physical Review X **3**, 031015.

Schmidt, E. (1907), "Zur Theorie der linearen und nichtlinearen Integralgleichungen," Mathematische Annalen **63** (4), 433.

Schrödinger, E. (1935a), "Die gegenwärtige Situation in der Quantenmechanik," Naturwissenschaften **23** (49), 823, [See Wheeler and Zurek, 1983].

Schrödinger, E. (1935b), "Discussion of Probability Relations between Separated Systems," Mathematical Proceedings of the Cambridge Philosophical Society **31**, 555.

Schrödinger, E. (1936), "Probability relations between separated systems," Mathematical Proceedings of the Cambridge Philosophical Society **32**, 446.

Shannon, C. (1948), "A mathematical theory of communication," The Bell System Technical Journal **27** (3), 379.

Shor, P. (1994), "Algorithms for quantum computation: discrete logarithms and factoring," in *Proceedings 35th Annual Symposium on Foundations of Computer Science*, pp. 124–134, Proc. 35th Annual Symposium on Foundations of Computer Science.

Song, H. F., S. Rachel, and K. Le Hur (2010), "General relation between entanglement and fluctuations in one dimension," Physical Review B **82**, 012405.

Srednicki, M. (1993), "Entropy and area," Physical Review Letters **71**, 666.

Taddia, L., J. C. Xavier, F. C. Alcaraz, and G. Sierra (2013), "Entanglement entropies in conformal systems with boundaries," Physical Review B **88**, 075112.

Tittel, W., J. Brendel, H. Zbinden, and N. Gisin (1998), "Violation of Bell Inequalities by Photons More Than 10km Apart," Physical Review Letters **81**, 3563.

Torlai, G., L. Tagliacozzo, and G. de Chiara (2014), "Dynamics of the entanglement spectrum in spin chains," Journal of Statistical Mechanics: Theory and Experiment **2014** (06), P06001.

Ueda, H., H. Nakano, K. Kusakabe, and T. Nishino (2010), "Scaling Relation for Excitation Energy under Hyperbolic Deformation," Progress of Theoretical Physics **124** (3), 389.

Ueda, H., and T. Nishino (2009), "Hyperbolic Deformation on Quantum Lattice Hamiltonians," Journal of the Physical Society of Japan **78** (1), 014001.

Ursin, R., F. Tiefenbacher, T. Schmitt-Manderbach, H. Weier, T. Scheidl, M. Lindenthal, B. Blauensteiner, T. Jennewein, J. Perdigues, P. Trojek, B. Omer, M. Furst, M. Meyenburg, J. Rarity, Z. Sodnik, C. Barbieri, H. Weinfurter, and A. Zeilinger (2007), "Entanglement-based quantum communication over 144km," Nature Physics **3** (7), 481.

Vekić, M., and S. R. White (1993), "Smooth boundary conditions for quantum lattice systems," Physical Review Letters **71**, 4283.

Verstraete, F., and J. I. Cirac (2004), "Renormalization algorithms for Quantum-Many Body Systems in two and higher dimensions," arXiv e-prints arXiv:cond-mat/0407066.

Vidal, G. (2007), "Entanglement Renormalization," Physical Review Letters **99**, 220405.

Vidal, G. (2008), "Class of Quantum Many-Body States That Can Be Efficiently Simulated," Physical Review Letters **101**, 110501.

Vidal, G., J. I. Latorre, E. Rico, and A. Kitaev (2003), "Entanglement in Quantum Critical Phenomena," Physical Review Letters **90**, 227902.

Vitagliano, G., A. Riera, and J. I. Latorre (2010), "Volume-law scaling for the entanglement entropy in spin-1/2 chains," New Journal of Physics **12** (11), 113049.

van Vleck, J. H. (1932), *The theory of electric and magnetic susceptibilities*, International series of monographs on physics (Oxford At The Clarendon Press).

Wheeler, J. A., and W. H. Zurek, Eds. (1983), *Quantum Theory and Measurement*, Princeton Series in Physics (Princeton University Press).

White, S. R. (1992), "Density matrix formulation for quantum renormalization groups," Physical Review Letters **69**, 2863.

White, S. R. (1993), "Density-matrix algorithms for quantum renormalization groups," Physical Review B **48**, 10345.

Wilson, K. G. (1975), "The renormalization group: Critical phenomena and the Kondo problem," Reviews of Modern Physics **47**, 773.

Xavier, J. C., and F. C. Alcaraz (2011), "Rényi entropy and parity oscillations of anisotropic spin-$s$ Heisenberg chains in a magnetic field," Physical Review B **83**, 214425.

Yang, C. N., and C. P. Yang (1966a), "One-Dimensional Chain of Anisotropic Spin-Spin Interactions. I. Proof of Bethe's Hypothesis for Ground State in a Finite System," Physical Review **150**, 321.

Yang, C. N., and C. P. Yang (1966b), "One-Dimensional Chain of Anisotropic Spin-Spin Interactions. II. Properties of the Ground-State Energy Per Lattice Site for an Infinite System," Physical Review **150**, 327.

Yang, C. N., and C. P. Yang (1966c), "One-Dimensional Chain of Anisotropic Spin-Spin Interactions. III. Applications," Physical Review **151**, 258.

Zamolodchikov, A. B. (1986), "Irreversibility of the Flux of the Renormalization Group in a 2D Field Theory," Pis'ma v Zhurnal Eksperimentalnoi i Teoreticheskoi Fiziki **43**, 565, [JETP Lett. **43** 730-732 (1986)].

Zamora, A., J. Rodríguez-Laguna, M. Lewenstein, and L. Tagliacozzo (2014), "Splitting a critical spin chain," Journal of Statistical Mechanics: Theory and Experiment **2014** (09), P09035.

# Appendix A

# Technical details

## A.1 Conformal representation

In this text we have employed a visualization scheme for correlation matrices of critical, or near-critical, 1D states, inspired by the AdS/CFT correspondence. The reason is that the resulting images are both informative and suggestive.

The AdS/CFT correspondence (Maldacena, 1999) states that gravity theories on an Anti-de Sitter (AdS) space are in one-to-one correspondence with conformal quantum field theories on its boundary. This conjecture has proved extremely fruitful helping explain the behavior of entanglement in critical systems. Concretely, Ryu and Takayanagi (2006) showed that the entanglement of a block in the conformal QFT can be estimated as the area of the minimal surface in the associated AdS space. In the particular case of 1D CFT, the associated AdS space is bidimensional, and the minimal surfaces correspond to geodesics in that metric.

AdS is a hyperbolic space with constant negative curvature. In 2D, the most relevant realization of AdS with a boundary is given by the Poincaré metric on the upper half-plane:

$$ds^2 = \frac{1}{y^2}\left(dx^2 + dy^2\right) \tag{A.1}$$

Notice that this metric is singular at the $y = 0$ line. It can be proved that its geodesics are half circumferences with their center on that line. A conformal transformation can map it into an AdS space inside the unit circle:

$$w = \frac{1 - iz}{z - i} \tag{A.2}$$

Our representation for the correlation matrix operates as follows. For any matrix element, $C_{ij}$, we compute the geodesic line in the AdS space inside the unit circle

obtained by means of the conformal transformation (A.2). Then we draw that line with a color which marks the strength of the correlation between those points.

A finitely-correlated state will be characterized by a correlation matrix whose representation is given by short lines which do not go deep inside the unit circle. A conformal state, with infinite correlation length, is characterized by a certain self-similar structure in the geodesic pattern. Realizations of our random singlet states, or the rainbow state correlations are also very easy to spot.

## A.2 Strong Disorder Renormalization Group

The decimation procedure applied in the strong disorder renormalization group (SDRG) was developed by Dasgupta and Ma (1980), here we . Lets focus on the Heisenberg model

$$H = \sum_{i=1}^{N} J_i \vec{S}_i \cdot \vec{S}_{i+1}.$$

Let be $J_i$ the largest exchange coupling sites $i$ and $i+1$. We diagonalize the 2-sites block $[i, i+1]$ with a Hamiltonian

$$H_0 = J_i \vec{S}_i \cdot \vec{S}_{i+1}$$

to obtain a spin singlet state $|\phi_0^{(0)}\rangle$ with energy $E_0^{(0)} = -3J_i/4$ and a 3-fold degenerate triplet state $|\phi_k^{(0)}\rangle$ with energies $E_k^{(0)} = J_i/4$ for $k = 1, 2, 3$. The block $[i, i+1]$ is connected to the sites $i-1$ and $i+2$ and its dynamics is described by the perturbation Hamiltonian

$$H_1 = J_{i-1} \vec{S}_{i-1} \cdot \vec{S}_i + J_{i+1} \vec{S}_{i+1} \cdot \vec{S}_{i+2}$$

then we obtain the ground state energy to the second perturbation order

$$\begin{aligned} E_0 &= E_0^{(0)} + \langle \phi^{(0)} | H_1 | \phi^{(0)} \rangle + \sum_k \frac{|\langle \phi_k^{(0)} | H_1 | \phi_0^{(0)} \rangle|^2}{E_0^{(0)} - E_k^{(0)}} \\ &= -\frac{3J_i}{4} - \frac{3}{16 J_i} \left( J_{i-1}^2 + J_{i+1}^2 \right) + J_i^{(R)} \vec{S}_{i-1} \cdot \vec{S}_{i+2} \end{aligned}$$

where

$$J_i^{(R)} = \frac{J_{i-1} J_{i+1}}{2 J_i} \tag{A.3}$$

## A.3 Brief summary of the quasi-particules picture

The entropy after a quench to a conformal field theory (CFT) from a massive state follows the laws

$$S_A(t) \simeq \begin{cases} \frac{\pi c}{6\epsilon} t & t < \frac{\ell}{2} \\ \frac{\pi c}{6\epsilon} \ell & t > \frac{\ell}{2} \end{cases} \tag{A.4}$$

where $\ell$ is the size of the block $A$ whose entanglement entropy is computed and $\epsilon$ a UV cutoff that for a lattice model will be essentially of order one.

The quasiparticles picture introduced by Calabrese and Cardy (2005) can be resumed as

- The initial state has a very high energy relative to the ground state of the hamiltonian and therefore acts as a source of quasiparticle excitations.
- Particles emitted from different points (further apart than the correlation length in the initial state) are incoherent, but pairs of particles moving to the left or right from a given point are highly entangled.
- The particles are created by pairs and move classically with a speed that is lower than the speed on light.
- The results for the entropy are a consequence of causality.

These rules explain the saturation of the entropy when $t > \ell/2$. This picture explains the results obtained by Calabrese and Cardy (2005) using CFT. However it is not clear the nature of these quasiparticles, or what are their properties, i.e. what are their scattering amplitudes or dispersion relation and/or propagation speed.

# Acronyms

| Notation | Description |
|---|---|
| **AFM** | anti-ferromagnetic. |
| **AKLT** | Affleck, Kennedy, Lieb and Tasaki. |
| **APBC** | anti periodic boundary conditions. |
| **CDF** | cumulative distribution function. |
| **CFT** | conformal field theory. |
| **CSP** | concentric singlet phase. |
| **DMRG** | density matrix renormalization group. |
| **EE** | entanglement energy. |
| **EPR** | Einstein-Podolsky-Rosen. |
| **ES** | entanglement spectrum. |
| **FCS** | finitely correlated states. |
| **FM** | ferromagnetic. |
| **GS** | ground state. |
| **IRFP** | infinite-randomness fixed point. |
| **JW** | Jordan-Wigner. |
| **KPZ** | Kardar-Parisi-Zhang. |
| **MERA** | multiscale entanglement renormalization Ansatz. |
| **MPS** | matrix product state. |
| **NRG** | numerical renormalization group. |

| Notation | Description |
|---|---|
| **OBC** | open boundary conditions. |
| **PBC** | periodic boundary conditions. |
| **PDF** | probability distribution function. |
| **PEPS** | projected entangled pair states. |
| **PH** | particle-hole. |
| **RG** | renormalization group. |
| **RVB** | resonating valence bond. |
| **SDRG** | strong disorder renormalization group. |
| **TEBD** | time evolution block decimation. |
| **TN** | tensor networks. |
| **TPS** | tensor product state. |
| **VBS** | valence bond state. |